Ph.D. Thesis

Halloysite Nanotube Colloids: From Fundamentals to Applications as Antioxidant Agents

Bojana Katana

Supervisor:

Dr. István Szilágyi

Associate Professor

Doctoral School of Chemistry

MTA-SZTE „Lendület” Biocolloids Research Group

Department of Physical Chemistry and Materials Science

Faculty of Science and Informatics

University of Szeged

Szeged

2022

Table of Contents

List of Abbreviations

HNTs	halloysite nanotubes
h-HNTs	hydroxylated halloysite nanotubes
NPs	nanoparticles
ROS	reactive oxygen species
SOD	superoxide dismutase
CAT	catalase
HRP	horseradish peroxidase
GPx	glutathione peroxidase
LDH	layered double hydroxides
PSP	protamine sulfate
PEI	poly(ethyleneimine)
PDADMAC	poly(diallyldimethylammonium chloride)
PSS	polystyrene sulfonate
EDL	electrical double layer
PB	Poisson-Boltzmann
IEP	isoelectric point
ASP	adsorption saturation plateau
ILs	ionic liquids
BMPYRCl	1-butyl-1-methylpyrrolidinium chloride
BMPYCl	1-butyl-2-methylpyridinium chloride
BMPIPCl	1-butyl-1-methylpiperidinium chloride
MIMCl	1-methylimidazolium chloride
EMIMCl	1-ethyl-3-methylimidazolium chloride
BMIMCl	1-butyl-3-methylimidazolium chloride
HMIMCl	1-hexyl-3-methylimidazolium chloride
DLVO	Derjaguin, Landau, Verwey, and Overbeek
PDI	polydispersity index
DLS	dynamic light scattering
ELS	electrophoretic light scattering
CCC	critical coagulation concentration
TEM	transmission electron microscopy
SEM	scanning electron microscopy
TGA	thermal gravimetric analysis
EPR	electron paramagnetic resonance
NBT	nitro blue tetrazolium
Cu(Cit)	copper(II)-citrate

1. Introduction

Halloysite clay nanotubes (HNTs) are natural layered aluminosilicate ($Al_2Si_2O_5(OH)_4 \cdot nH_2O$) based materials with hollow tubular structures. The size of HNTs varies between 40–70 nm in outer diameter and 10–20 nm in inner diameter, and their length generally spans between 200–1500 nm. The outer surface is negatively charged in a broad range of pH owing to the existence of deprotonated silanol groups, while the inner lumen consists of aluminol groups, thereby it becomes positively charged at intermediate and lower pH. This distinctive dual-charge nature combined with biocompatibility and wide accessibility makes HNTs attractive for a range of applications, such as important building blocks in composites exploited in biomedical, environmental, and catalytic processes.

Since HNT particles are dispersed in liquid media comprising dissolved electrolytes in numerous applications, a profound understanding of their colloidal behavior is required before utilizing them in such media. In addition to an aqueous environment, novel solvents like ionic liquids (ILs) have become key components in systems containing HNT materials. There is scientific consensus that sample colloidal stability is a critical issue once nanoparticle dispersions containing simple electrolytes or ILs are included in the application procedures.

Among other applications, nanoparticles have lately become well-known candidates as supports for biocatalytic compounds. For instance, antioxidant enzymes, such as superoxide dismutase (SOD), show the greatest potential in preventing and regulating the negative implications of reactive oxygen species (ROS), but their supplementation is difficult due to their high sensitivity to environmental conditions. This issue might be resolved by immobilizing enzymes on solid supports. Apart from enzymes, the embedding of molecular and artificial antioxidants in nanostructures is of great contemporary interest. The role of the solid support is to stabilize the structure during the supplementation procedure and deliver the bioactive agents to the desired place in living organisms or industrial samples.

Owing to their beneficial properties discussed above, HNTs are promising candidates as solid supports for the immobilization of antioxidants or other molecules of biological interest. However, most HNT applications require surface functionalization, e.g., with polymeric compounds, as it has been commonly observed that such functionalization can improve the adsorption of the guest molecules while optimizing the colloidal stability of the nanotubes.

In the present thesis, a comprehensive analysis of the colloidal behavior of the HNT particles in liquid phases was conducted. First, the colloidal stability of the HNT materials in

the attendance of monovalent and multivalent inorganic electrolytes was investigated. Next, the influence of the IL constituents (with various cationic structures and imidazolium-based with alkyl chains of different lengths) in their assembly at the solid/liquid interface of the HNT dispersions was evaluated. Then the colloidal stability of the HNT particles was tuned by altering the surface with both natural and synthetic polyelectrolytes through the adsorption process. Finally, after an extensive evaluation of the basic colloidal behavior, the HNT particles were further involved as a carrier in the development of stable antioxidant colloids composed of polyelectrolytes, and bioactive molecules such as antioxidant enzymes and metal complexes with enzyme-like functions. The results of these investigations were attained utilizing experimental techniques including diverse microscopy, spectroscopy, and scattering techniques.

2. Literature Review

2.1. Colloidal dispersions

In general, colloidal dispersions or colloids are defined as a type of mixture consisting of solid, liquid, or gas particles dispersed in a continuous phase. The term „colloidal" refers to particles that have at least one dimension in the range of 1 nanometer to 1 micrometer. One of the most common types of colloidal dispersions is solid-liquid, i.e., suspensions, then liquid-liquid or emulsions, gas-liquid or foams, and solid-gas or aerosols. Particle dispersions are applied in different fields, from biomedical through industrial to environmental processes. These systems have found various applications, such as in the food industry[1], water treatment[2], papermaking[3], and paints[4], or as carrier systems in biomedicine[5], or as building blocks for various functional materials through the process of self-assembly (Figure 1).[6,7]

Figure 1. Applications of colloidal particles in various fields.

The size and shape of the particles are of great importance influencing the general properties of the colloidal systems. For example, spherical shapes, the simplest, are characteristic for emulsions, gold, and silica sols, while elongated shapes are characteristic for clays, carbon derivatives, or chalcogenides.[8] Numerous applications of particle dispersions depend strongly on their colloidal stability. Stabilization serves to prevent the aggregation of the particles. Once the primary particles are homogeneously distributed in the continuous liquid phase, stable dispersions with high colloidal stability are formed, while unstable dispersions with low colloidal stability are the result of the rapid aggregation of the particles. The latter

leads to the formation of large aggregates after longer time, which can connect leading to phase separation.[8] Therefore, it is crucial to maintain the stability of the colloidal systems. In addition to the composition and concentration of the particles, the surface charge of the particles is a property that significantly affects stability. The type of solvent, the pH of the medium, and the addition of electrolytes and surface-active agents or macromolecules can cause either stabilization or aggregation.

However, different applications require different colloidal behavior of the particles. For example, in water treatment, the addition of charged polymers (so-called polyelectrolytes) or multivalent ions to suspended solid particles leads to the formation of large aggregates and to subsequent phase separation that can be easily removed by sedimentation or filtration.[2] Following the same principle, filler particles such as clay, silica, or titania are often added in the paper industry before the coagulation process to improve the properties of the final paper product. Filler particles and cellulose fibers present in the suspension, together with charged polymeric flocculants, can form aggregates that allow the formation of raw materials.[3] On the other hand, the food and paint industries require the presence of stable dispersions. Many polymers and biocompatible particles are also added to foods because they can accumulate on the water-oil interface in the case of emulsions or on the water-air interface in the case of foams.[9,10,11] The invention and use of systems that allow the stabilization of pigments led to the development of water-based paints, eliminating the use of many toxic organic solvents in the paint industry.[4,12] Besides, in drug delivery systems, the application of carrier particles is more complicated because of the aggregation processes must be controlled in a complex fluid such as blood.[13]

2.2. Nanoparticles and nanoparticle-based composites

2.2.1. Generic remarks on nanomaterials

Nanoparticles (NPs) are a special type of solid materials whose size ranges from 1 to 100 nanometers. The applications of nano-sized particles have gained great attraction in recent decades due to their advantageous physical and chemical properties as well as to the landmark development in the experimental methodology suitable to investigate the nanoscale range interactions.[14] In general, nanoparticles can be divided into a few major groups including metals, oxides, sulfides, silicates, and other non-metallic nanocomposites (e.g., carbon or polymer-based). Metal nanoparticles encompass gold, silver, alloys, and other metals. Silver nanoparticles show great antimicrobial activity against gram-positive and gram-negative bacteria and highly resistant rod-shaped bacteria.[15] Nanoparticles of various alloys are

increasingly used in catalysis, electronics as optical materials, and coatings.[16,17,18] Nano-sized heavy metals can be synthesized using microorganisms, which is much more beneficial to the environment than synthesis by chemical means, but then these particles are harmful to the microorganisms themselves too. Sulfide nanoparticles represent an interesting group due to their novel electronic and optical properties.[19,20] They can be used as fluorescent biomarkers and cell labeling agents. Oxide nanomaterials can be divided into those with and without magnetic properties. Nano-sized magnetic particles attract widespread contemporary interest with the possibility of application in biomedicines due to their unique microscopic structure and certain properties such as paramagnetism and strong attractive forces. For instance, Fe_2O_3 and Fe_3O_4 are known to be biocompatible, and recently, they have been used for targeted cancer treatment (magnetic hyperthermia), targeted drug delivery, gene therapy, DNA analysis, and magnetic resonance imaging.[21] Non-magnetic oxide nanocomposites that have been recently studied include TiO_2, Sb_2O_3, SiO_2, $BaTiO_3$, and ZrO_2.

Based on their dimensions and shapes, nanomaterials can be divided into several groups. The first group is nanocomposites, nanostructured surfaces, and nanocomponents, where nanoparticles are included in the material. The second group includes individual nanoparticles, which can be formed independently during the application or at certain stages of production. When considering the dimension of nanoparticles, they exist as zero-dimensional (0D), one-dimensional (1D), two-dimensional (2D), and three-dimensional (3D) particles. The 0D nanomaterials, such as nanospheres and nanoclusters, are those whose all dimensions are within the nanoscale (1-100 nm). The 1D nanoparticles, such as nanotubes, nanopores, and nanofibers, are nanomaterials whose one dimension is outside the nanometer range, usually the length. For 2D nanoparticles, two dimensions are outside the nanoscale, such as graphene nanosheets, nanofilms, and nanolayers.[22] The 3D nanomaterials are larger than 100 nm in all dimensions, but there are either built up by lower dimensional nanomaterials (e.g., graphite is built up by graphene (2D)) or possess certain units, which are in the nanoscale range (e.g., pores of zeolites).[23]

Nanotube-based materials have attracted considerable interest in both the industrial and scientific communities due to their many properties, such as adaptable structural design, and unique physical and chemical properties. Different forms of nanotubes, including carbon, titania, inorganic, and polymeric nanotubes, have been produced using a variety of techniques, including hydrothermal synthesis, surfactant-assisted synthesis, and decomposition.[24,25,26] Nanotubular systems have a wide range of applications in different fields, such as energy

storage, catalysis, optics or electronics, and biological systems.[24,27,28,29,30]

Depending on their origin, nanoparticles can be divided into intentional (engineered or designed), which are created to take advantage of their inherent nanoscale properties, and unintentional, which can originate from anthropogenic (fuel combustion or mining) and natural sources (forest fires, volcanic eruptions, lightning, etc.). Some nanoparticles may belong to both groups (e.g., fullerenes). Synthetic nanoparticles, commonly referred to as engineered nanoparticles, are of particular interest due to their application in many emerging technologies and consumer products such as electronic devices and personal care and food products[1], agriculture, water treatment, and renewable energy processes[14], or in biomedical treatments.[21] Concerning the toxicity of nanomaterials, different nanostructures may have different effects on human health and on the environment, which is also related to their origin.

Aluminosilicate-based nanomaterials represent an attractive class of materials due to their many advanced properties and wide application possibilities. In general, aluminosilicates are raw minerals that are frequently used in the manufacturing industry because of their large available deposits and low-cost investigations. Despite that all aluminosilicates have the same chemical composition, the different atom and molecular configurations result in structures with various and unique physico-chemical characteristics.[31] Aluminosilicates exist in numerous different types, natural or synthetic, and among the most used and investigated ones are clays, zeolites, and mesoporous aluminosilicates.[32] They are characterized by their layered structure, where each layer is composed of two types of structural sheets, octahedral and tetrahedral.[31,33] The silicon-oxygen tetrahedra that form the tetrahedral sheet are connected by sharing three corners and creating a hexagonal network. The fourth, left corner of each tetrahedron contributes to the neighboring octahedral sheet. Typically, an octahedral sheet is composed of aluminum or magnesium with the hydroxyl and oxygen of the tetrahedral sheet.[31] Aluminosilicates are also commonly referred to as natural phyllosilicates, and examples include montmorillonite, bentonite, kaolinite, and halloysite.[33,34,35] These materials are usually subjected to organic modification to change their surface characteristics and increase their adsorption capacity. These clay minerals are distinguished from other colloidal materials by their frequently asymmetric shape of the particles, wide variety of particle sizes, the flexibility of the layers, heterogeneity of charge of the layers, great cation exchange capacity, and various methods of aggregation.[34]

Due to their high surface area, excellent thermal and hydrothermal stability, high shape-selectivity, and exceptional ion-exchange capability, aluminosilicates have been significant

materials for applications in biomedical formulation, as excipients in pharmaceutical preparations. They also found a wide application in the area of catalysis (zeolites)[36] or in civil engineering or sealing materials (bentonite),[34] as well in the environmental technology in wastewater treatment.[37] Among the aluminosilicate-based nanomaterials, halloysite is one of the leading candidates for a variety of applications, including biomedicine, drug delivery systems, supply, and sustained release of active agents for anticorrosive coatings, in nanoreactors or nanotemplates, then in environmental area and catalysis.[35,38,39,40,41] The following chapters will provide a more elaborative description regarding the composition, characteristics, and application of the halloysite material.

2.2.2. Halloysite nanotubes (HNTs)

This chapter introduces the subject matter - halloysite nanotubes (HNTs) - on which all the research in this thesis is based. The fundamental features including composition, size, and charge are outlined.

As already mentioned in the previous chapter, the clays represent attractive group of materials with potential nanoscale organization and broad applicability.[42] There are two main categories of clays: cationic clays, which are more common in nature, and anionic clays, which can be synthesized.[43] Tetrahedral SiO_4 and octahedral AlO_6 dominate the layered structure of the cationic clays.[44] Clay minerals can be classified as 1:1 or 2:1 based on the distribution of these domains. Accordingly, a 1:1 clay consists of a tetrahedral and an octahedral sheet, such as kaolinite and serpentinite, while a 2:1 clay is composed of an octahedral sheet packed between two tetrahedral sheets, like talc, vermiculite, and montmorillonite.[44] Although these materials can be divided into several groups according to their layered structure, let us focus now on the kaolin group. One of the representative minerals belonging to the kaolin subgroup is halloysite. Halloysite is a nanotubular aluminosilicate-based clay mineral, which is created by rolling up the kaolinite clay sheets. Along with the significant deposits of this material in New Zealand, the Dragon Mine in Eureka, Utah, USA, is one of the largest deposits of catalytic grade halloysite.[45] It has also been discovered in basaltic rocks and together with carbonates.[46]

2.2.2.1. Structural aspects

In addition to the water molecule and elements that are included in its chemical structure, such as Al, Si, halloysite frequently contains impurities including zinc, calcium, magnesium, iron, nickel, and chromium, causing a color change of the mineral from white to yellowish and brown. Microcrystalline aggregates are the most common type of halloysite. As the crystals

grow, they bend into cylindrical tubes.[47] Halloysite continuously loses water under normal atmospheric conditions, and there are transitions from a fully hydrated state to a dehydrated state. It loses water from the interlayer space when the temperature reaches 50 °C or the relative humidity is below 50%.[48] Initially, there is a transition from semi-hydrated to dehydrated halloysite with a layer thickness of 10 Å, and then dehydrated halloysite with a layer thickness of 7.2 Å.[47]

Halloysite nanotubes (HNTs) are, hence, 1:1 layered aluminosilicates with a distinctive hollow tubular structure and a unique chemical formula of $(Al_2Si_2O_5(OH)_4 \cdot nH_2O)$.[49,41,50] This composition is typical for kaolinite, however, the water molecule is packed between two layers. The layers consist of aluminum oxide octahedra and silicium oxide tetrahedra. Dry HNT is thought to be composed of 10 to 15 double layered aluminosilicate sheets that have been rolled into a cylindrical shape. The wall packing of this substance can be evaluated using a (00l) X-rayBragg reflectance of 0.72 nm.[47] Figure 2 depicts the structure and chemical composition of the HNTs. Tubes ordinarily have an outer diameter of 40–70 nm, an inner lumen diameter of 10–20 nm, and a length of 200–1500 nm. Although the dimensions may vary, for example ,tubes with a length of 1 μm have proven to be useful, as this is a safe dimension for macrophages to remove nanoparticles from living organisms.[48] Larger tube diameters have also been observed, but smaller clay nanotubes are of greatest interest for the sustained release of chemical compounds and drug formulations. Due to intense crushing during industrial processing, HNTs used for commercial purposes have shorter lengths of around 400–500 nm.[47]

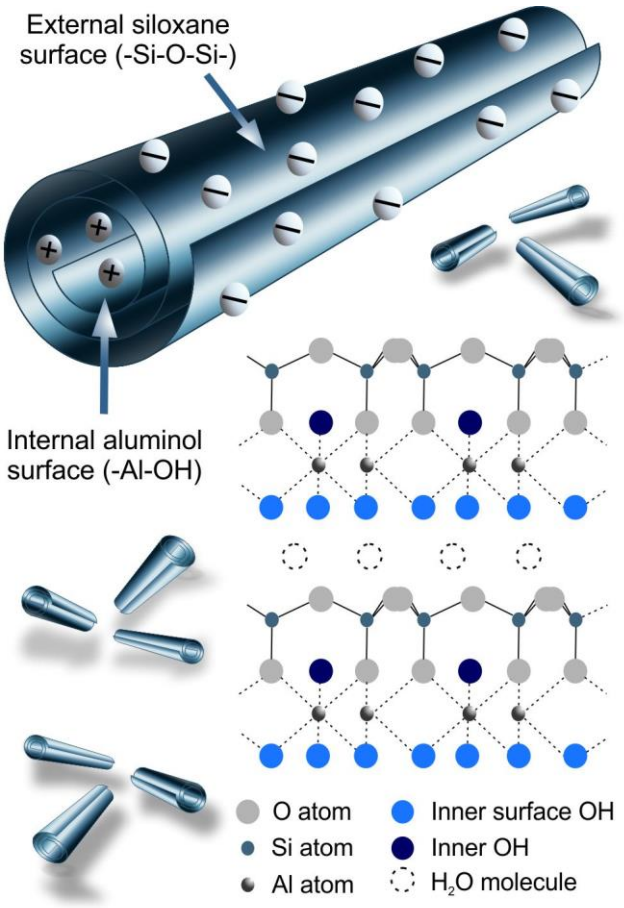

Figure 2. Schematic illustration of the structure and chemical composition of HNTs.

Microscopically, it is quite difficult to distinguish kaolinite and halloysite. The identification of halloysite material requires the use of special examination spectroscopic

techniques, such as IR and Raman spectroscopy.[51] The nanotubular form of halloysite allows easy dispersion of these particles, which is not the case with platy kaolin or montmorillonite, and bentonite particles.[48,49]

In a study conducted by Lvov[48], the HNTs were found to be stable at temperatures up to 460 °C, where dehydroxylation occurred, destroying the multilayer packing of the HNT walls. Thermogravimetric studies reveal a mass decrease of about 12 wt%, but the tubular shape of the clay retained even up to 900 °C. The outer layer of the HNT is made of silicon dioxide and, hence, it is negatively charged due to the presence of the deprotonated silanol groups and their surface zeta potential value at pH 4–8 is about –30 mV.[47,41] The internal surface is composed of aluminium oxide providing a positively charged lumen at neutral or lower pH values.[52] HNTs are a very unique type of nanotubes, due to this dual charge composition. HNTs have a density of about 2.53 $g \cdot cm^{-3}$, the porosity of 50–60 $cm^2 \cdot g^{-1}$, and cation exchange capacity of about $30–50 \times 10^{-2}$ $mol \cdot kg^{-1}$.[47, 48]

2.2.2.2. Applications

Because it is a natural material, halloysite has no environmental risks and possesses great promise in sustainable applications.[48] Toxicity testing of HNTs has shown that they are not hazardous to cells. The reported data suggest that HNT composites are safe for use in biomedical applications when less than 0.1 wt% of halloysite is added to cell culture.[53] HNTs are promising candidates for a range of applications, including biomedical[47,54], as nanocarriers for effective targeting in cancer therapy[55, 56], then in environmental disciplines (waste-water treatment)[57,58], in nanoelectronics[59], and catalytic processes[39, 60] or as a material for stabilizing Pickering emulsions[61] and in food packaging systems[62], or as an alternative detergent.[60, 63] These applications are enabled by the different compositions of the inner and outer surfaces, biocompatibility, high aspect ratio, and large-scale availability. Numerous studies have demonstrated these exceptional properties of HNTs, making them suitable for drug delivery, medical implants, and cosmetics.[48,49] They are also suitable building blocks for the development of nanocomposites, according to reported studies.[41,50] The abundance of functional groups on the inner and outer surfaces of HNTs allows them to act as nanocontainers, and they can be used for loading antioxidants such as quercetin[64], curcumin[65], and resveratrol[66], bioactive compounds including enzymes or drug molecules.[67,68,45] These studies included structural features, release assays, and antioxidant activities; the results showed that HNTs are good carriers. Different types of immobilized agents and the methods of immobilization will be discussed in detail in the following chapters and some examples are shown in Figure 3.

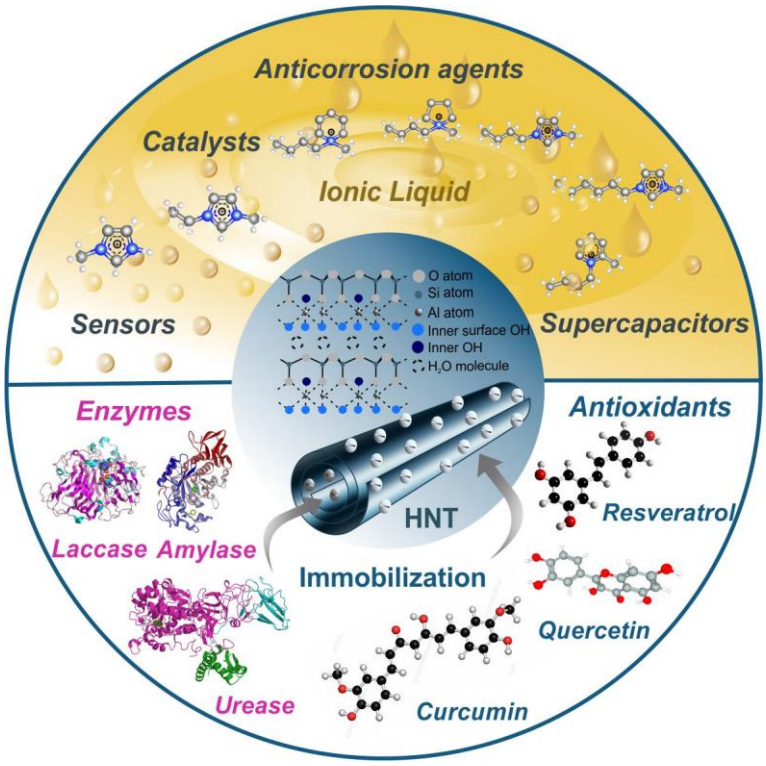

Figure 3. Possible applications of HNT materials dispersed in ionic liquids or used as a carrier material during immobilization of various enzymes or antioxidants.

HNT materials have demonstrated excellent qualities and capacities when dispersed in novel solvents such as ILs, in addition to their ability to act as solid supports or containers in immobilization or loading operations. Systems composed of ILs and HNT nanoparticles have attracted considerable attention in a variety of applications.[69] More about these systems and the effect of ILs, in general, will be discussed in one of the following chapters. Figure 3 also includes some application examples for HNT-IL systems. HNT materials have also been used in the cultural heritage protection. Bionanocomposite films consisting of HNT loaded with natural antioxidants have been proved as promising films for the surface protection of artworks.[70] In another study, biopolymers filled with inorganic micelles or Pickering emulsions based on HNT were used for controlled cleaning of marble sculptures, monuments, artifacts or wood surfaces.[71]

2.2.2.3. Colloidal features

The colloidal stability of commercially available HNTs is a significant issue in liquid phase applications[72, 73] since their resistance to aggregation processes is limited, i.e., their dispersions can be conveniently destabilized by electrolyte-induced aggregation and subsequent sedimentation. Various utilizations take place in liquid media[49,74,75,76], but less attention has been given to the colloidal features of dispersions. The weak colloidal stability of the

commercial HNTs has been observed in numerous studies[50,77,78,79] resulting in aggregation and subsequent sedimentation of HNT materials. However, prior to any further research in dispersions, the HNTs can be alkaline treated, which increases the number of surface silanol groups and enhances colloidal stability, to be discussed in more detail later. There are also numerous efficient approaches to govern aggregation processes and tune the colloidal stability of HNTs, such as surface alteration with appropriate polyelectrolytes. The colloidal features of HNTs also depend on the type and concentration of the electrolytes present in the dispersions, while comprehensive investigations dealing with this issue are missing.

2.3. Colloidal stability

Since the colloidal stability of particle suspensions greatly influences their synthesis or applications, its extensive understanding is an essential point before their use. Two groups of scientists, Boris Derjaguin and Lev Landau, as well as Evert Verwey and Theo Overbeek, independently developed and presented a theoretical analysis of the colloidal stability known as the DLVO theory. The basic ideas were first developed by Boris Derjaguin, then expanded in an article co-authored by Lev Landau[80], and later further disseminated in a book by Evert Verwey and Jan Overbeek.[81] Accordingly, the theory affirmed that the colloidal stability of particles depends strongly on the interplay between the attractive van der Waals forces (London forces) and double layer forces (Coulomb forces).

Let us first discuss the interface of charged particles immersed in an electrolyte solution, i.e., in the presence of dissolved salt constituents. The spatial distribution of ions around the charged surface controls its electrical state. The term electrical double layer (EDL) has been used to describe such charge distribution.[8,82] In case of a negatively charged particle, positive ions, which act as counterions, will be collected in the diffuse layer near the surface. The representation of the EDL formation is described in Figure 4. The basic model predicts that one layer of EDL is a fixed charge tightly bound to the particle or solid surface, and another layer is relatively diffusely distributed in the solution in contact with the surface. In this layer, there is a deficiency of co-ions, which are of the same sign as the fixed charge, and an excess of counterions, which are of the opposite sign of the fixed charge.[82] The concentration of the counterions will decrease progressively from the surface to the bulk concentration. In contrary, the concentration of the co-ions will increase from the surface until reaches the bulk concentrations.[83]

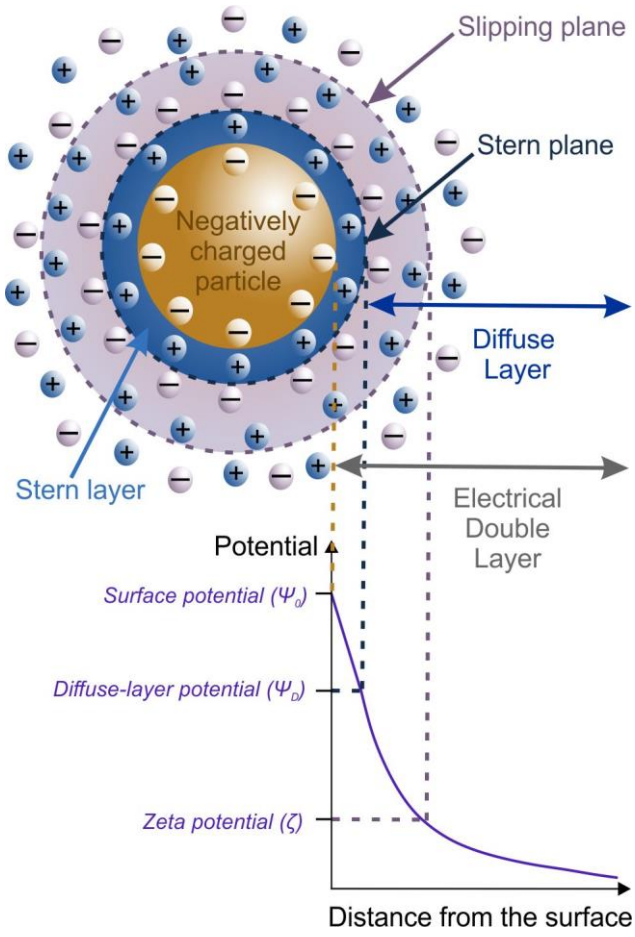

Figure 4. Schematic representation of the EDL structure for negatively charged surface.

As shown in Figure 4, there are three types of potentials that need to be defined. Namely, surface potential (ψ_0) refers to the potential at the surface of the particle that is in the contact with ions. The potential at the start of the diffuse layer is called diffuse-layer potential (ψ_D). Zeta potential (ζ) refers to the potential at the slipping plane, which can be defined as the potential difference between the dispersion medium and the stationary layer of liquid adhered to the particle, and it is one of the most important parameters in prediction of interactions of colloidal particles.[82, 84,85]

The mechanisms governing the interaction energy between colloid particles as well as the aggregation behavior have been predicted using the DLVO interaction energy profile.

The DLVO theory states that the total energy of the interaction ($V(h)$) between two identical particles at distance h can be estimated by the contribution of the electrical double layer ($V_{EDL}(h)$) and the van der Waals potential energy ($V_{vdW}(h)$):

$$V(h) = V_{EDL}(h) + V_{vdW}(h) \quad (1)$$

Figure 5 shows the DLVO interaction potential energy profile as a function of the distance between two colloidal particles. At short and large distances, van der Waals forces control the profiles, and the potential curve exhibits the deep primary minimum, while the double layer force dominates at intermediate distances where the energy profile reaches a secondary minimum. Primary and secondary minima are separated by an energy maximum, referred as energy barrier. The energy barrier, which depends on the interaction between these potentials, is important in terms of the colloid stability of particle dispersion. The particles are subjected

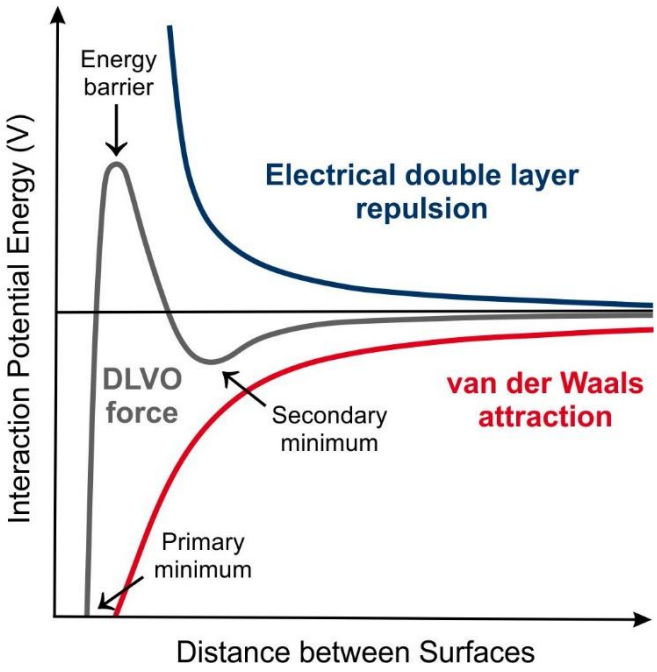

Figure 5. Schematic representation of the DLVO interaction potential energy between two colloidal particles as a function of the distance between two surfaces. The total interaction potential energy is the sum of the repulsive EDL and the attractive van der Waals forces.

to the diffusional motion in the suspending fluid, and when they come close enough, they adhere to each other and form an aggregate in an unstable sample. The formation of dimers may occur due to the high ionic strength in the dispersion, where the ions are able to screen the charge of the particles, reducing the extent of double layer repulsion and causing the energy barrier to disappear owing to the prevailing van der Waals forces. On the other hand, at lower salt concentrations, the energy barrier develops due to the stronger double layer interaction. Since the particles must overcome this barrier by thermal motion, they are separated from each other at large distances.[83,86] In this case, stable colloidal suspensions are obtained.

There are also non-DLVO forces, which can be attractive or repulsive, such as hydrophobic interaction[87], ion-ion correlation[88], depletion forces[89], or steric repulsion.[90] Additional terms describing the potential energy between two particles are involved.

$$V(h) = V_{EDL}(h) + V_{vdW}(h) + V_{non-DLVO}(h) \tag{2}$$

The van der Waals interaction potential can be expressed by applying the Derjaguin approximation, and in the case when the particle size is distinctly larger than the distance between particles, the relation can be expressed as follows[8,91]:

$$V_{vdW}(h) = -\frac{RH_{12}}{12h} \tag{3}$$

where R refers to the particle radius and H is Hamaker constant, which depends on the particle composition and the type of the medium.[8]

The repulsive double layer forces and the interaction energy profile can be determined by solving the Poisson-Boltzmann (PB) equation between two identical planar surfaces.[83,91] In an electrolyte medium with number of concentration c_i and valence z_i of the ionic species i in the solution, the electrostatic potential ψ as a function of the position x can be calculated as follows:

$$\frac{d^2\psi}{dx^2} = -\frac{e}{\varepsilon\varepsilon_o}\sum_i z_i c_i e^{-z_i e\psi/(kT)} \quad (4)$$

where e is the elementary charge, ε_0 and ε refer to vacuum permittivity and dielectric constant of water, k_B is the Boltzmann constant, and T is the absolute temperature. The PB model depends on the ionic composition, and it is required for systems with high surface charge. However, the PB equation can only be solved analytically for a small number of cases with simple boundary conditions, because it is a nonlinear second-order equation.

This type of interaction can also be well evaluated with the Debye-Hückel approximation in the case of particles with low surface charge density. The final equation for the potential energy of the double layer is thus reduced and can be expressed as a function of the electrostatic potential (ψ_D):

$$V_{EDL}(h) = 2\pi\varepsilon_0\varepsilon R\psi_D^2 e^{-\kappa h} \quad (5)$$

where κ is the inverse Debye length, which can be calculated as follows [83]:

$$\kappa = \sqrt{\frac{2N_A e^2 I}{\varepsilon_0\varepsilon k_B T}} \quad (6)$$

where N_A is the Avogadro constant, I is the ionic strength, which is usually expressed in mol/m^3, and can be calculated by the following relation:

$$I = \frac{1}{2}\sum_i c_i z_i^2 \quad (7)$$

where c_i is the molar concentration of the ionic species in the solution and z_i is the valence.

The rate, with which the aggregation proceeds, is the aggregation rate coefficient (k). There is a relation for the diffusion controlled aggregation rate, which was developed by Smoluchowski and can be expressed as follows[8,86]:

$$k = \frac{8k_B T}{3\eta} = 1.2 \times 10^{-17} m^3 s^{-1} \quad (8)$$

where η is the viscosity of the fluid and rate value in eq 8 refers to water medium at 25 °C.

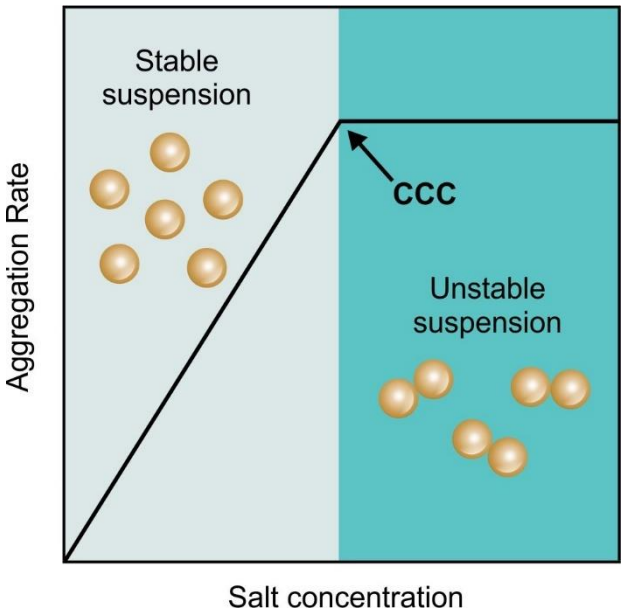

Figure 6. Schematic representation of the trend of aggregation rate of charged colloidal particles as a function of salt concentration.

When the salt concentration decreased, the aggregation rate also decreases rapidly due to the presence of the barrier originating from the double layer repulsion. Hence, these conditions are referred to as the slow aggregation regime. At high salt levels, the aggregation rate is increasing, and it is constant after a threshold value, and this refers to the fast aggregation regime or diffusion controlled aggregation independent from the electrolyte concentration. The clear and sharp changeover between the slow and rapid aggregation regimes is referred to as the critical coagulation concentration (CCC), as indicated in Figure 6. The CCC is an important parameter of the particles as it predicts the resistance against salt induced aggregation in a certain medium. A more detailed explanation of this parameter is given later in *subchapter 4.2.2.*

2.4. Controlling colloidal stability

Since the colloidal dispersions of charged particles have a variety of applications, a comprehensive understanding of their stability is essential. This chapter discusses the effects of monovalent and multivalent ions, and polyelectrolytes on the suspension stability of HNTs, and other colloids, in general. The information provided will help to better understand the origin of the interparticle forces responsible for colloidal stability and to develop highly stable or aggregating colloids in line with the goals of the desired specific applications.

2.4.1. Influence of mono- and multivalent ions

The colloidal stability of particles dispersed in solutions of monovalent electrolytes has been the subject of numerous studies during the past decades. Since DLVO theory only considers the concentration and valence of electrolyte constituents regardless of their chemical nature, it can give us insight to partly understand this issue. DLVO theory predicts the same effect of monovalent electrolytes of different compositions on colloidal stability (see eq 5-7, *chapter 2.3.*). However, within the DLVO theory, it is not possible to distinguish between different types of monovalent salts. Therefore, the theory predicts the same CCC value for all

types of ions of the same valence, and the ion specific effects on the aggregation processes is not considered within the framework of the theory. However, experimental studies reported in the past revealed that different monovalent salt constituents destabilize colloidal particles at different CCCs.[92,93,94,95 96,97,98,99] It is assumed that the ion specificity derives from the fact that salt constituents interact specifically with the surface, altering the surface charge density in different ways.[100,101,102]

This phenomenon induced the establishment of the Hofmeister series of cations and anions for particle aggregation processes, classifying them in order reflecting also their affinity to the surfaces considering the hydration level.[103,104,105] This theory was developed primarily by Franz Hofmeister with the aim of predicting the destabilization of protein solutions by inorganic salts.[106] However, it has also proved to be an excellent tool for predicting the stability of particle dispersions based on the nature of co- and counterions, with the exception of the higher valence ions that were included in the original version of the Hofmeister series, but their effect originates from different phenomena. Namely, the effect of the higher valence ions can be explained by another model, the Schulze–Hardy rule[107,108], which will be discussed in more detail later. Therefore, let us first consider the influence of the monovalent salts and how the order of the Hofmeister series is established. Depending on the surface of particles, whether it is hydrophobic or hydrophilic, and whether it possesses a positive or negative surface charge, the specific Hofmeister series can be created (Figure 7). On the left-hand side of the series highly hydrated anions are located, while less-hydrated anions are found on the right. The cations are arranged in the opposite way. Weakly hydrated cations are on the left, while highly hydrated ones are on the right.

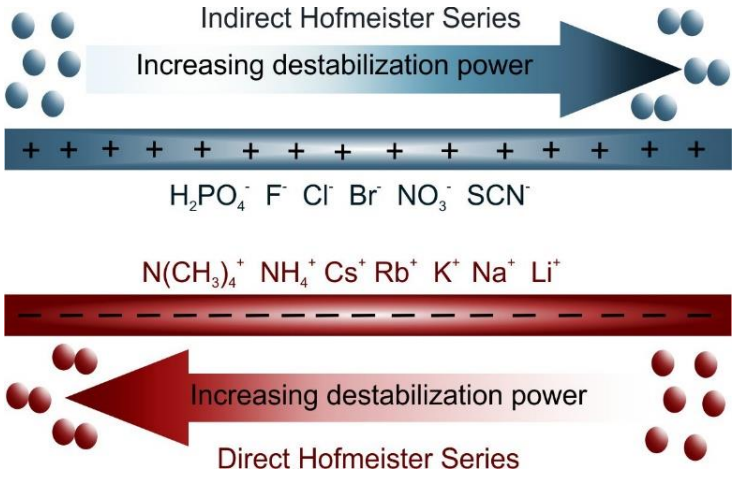

Figure 7. Illustration of the Hofmeister series for cations and anions in the presence of hydrophobic particles.

Given that the subject of my research was negatively charged HNT particles, let us first discuss the Hofmeister series and its significance on particle aggregation for negatively charged hydrophobic particles. The power of destabilization of cations follows the direct Hofmeister series, where cations act as the counterions. Weakly hydrated ions adsorb on the surface more strongly than the highly hydrated ions. Cation adsorption on the negatively charged surface decreases the surface charge and leads to a lower CCC values due to the weakening of the EDL repulsive forces. On the other hand, anion binding increases the magnitude of the surface charge and results in higher CCC values. Adsorption of anions results in a lower surface charge for positively charged particles, while adsorption of cations leads to the opposite. Therefore, the ions located on the right-hand side of the series lead to a lower CCC value and they will attend to adsorb on the surface more strongly, while the ions on the left-hand side lead to higher CCC value, and they destabilize the particle suspension by charge screening at only high concentration. Thus, in the case of positively charged surface, the destabilizing power tendency can be explained by the indirect Hofmeister series. For the hydrophilic particles, the sequence is reversed, so that negatively charged particles follow the indirect Hofmeister series, while particles with positive surface charge can be described by the direct Hofmeister series.[109] Therefore, ions of different chemical compositions adsorb on surfaces to different extents due to the specific interactions between the ions and the surface. Since the DLVO theory cannot differentiate types of ions of the same valence, this presumption can be explained by the fact that such specific ion adsorption alters the surface charge and the strength of EDL forces.[100,101,102, 110,111]

In the case of multivalent ions, the DLVO theory considers the valence of the ions, which can be explained by the Schulze–Hardy rule.[112] The rule was confirmed experimentally by Schulze[113] and Hardy[114] earlier and claims that multivalent ions destabilize the colloidal suspensions more efficiently than the monovalent ions. Numerous studies have been published with systems containing nanoparticles dispersed in electrolyte solutions of different valences.[115,116,117,118,119,120] The Schulze–Hardy rule assumes that the CCC values of the colloidal particles may depend on the counterion valence (z), as follows:

$$CCC \sim z^{-n} \tag{9}$$

The above empirical relation allows the comparison of the fitted calculated CCCs with experimental data. According to DLVO theory, the onset of fast particle aggregation controls the destabilization of colloidal suspensions, if considers the presumption that the interactions

are dominated by dispersion and double layer forces, where the latter ones are described within the Poisson–Boltzmann theory (eq 4, in *chapter 2.3.*). The Debye-Hückel approximation can be used instead of the PB equation for weakly charged particles.[121,122,123,124] The electrolyte composition here enters through the Debye length, which is solely dependent on ionic strength (*chapter 2.3.*). Multivalent counterions greatly reduce the surface charge by adsorbing to oppositely charged substrates. With increasing the valence, this reduction becomes more pronounced, which results in a lower CCC. Low magnitudes of the diffuse layer charge density and partial charge neutralization are the results of this adsorption process.[123]

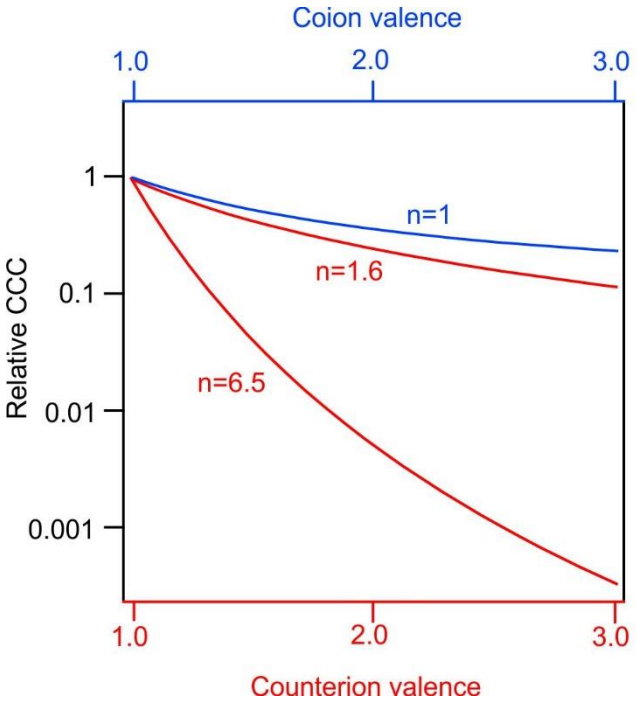

Figure 8. Illustration of the Schulze–Hardy rule and inverse Schulze–Hardy rule.

The effect of the valence on the relative CCC is illustrated in Figure 8. In investigations, asymmetric 1:*z* or *z*:1 multivalent electrolytes are generally used since symmetric *z:z* electrolytes are typically practically insoluble.[125] For asymmetric electrolytes (z :1 or 1: z), consisting of multivalent counterions, the value of parameter *n* might vary between 1.6 and 6.5 for counterions depending on the surface charge density. The DLVO theory predicts *n* = 1.6 for low surface charge concentrations. With increasing the surface charge densities, the dependence becomes stronger and similar for both, symmetric and asymmetric electrolytes. However, the *n* = 6.5 dependence refers only to highly charged particles (around 1000 mC/m^2), which is highly unrealistic for natural or synthetic particles. Note that these ion valence dependencies presuppose a constant charge density. In realistic situations, the charge densities may also change depending on the valence type, which could result in a varied apparent exponent in eq 9.[122]

Multivalent ions can act as counterions or co-ions in asymmetric electrolytes, depending on whether they are oppositely or have the same charge as the surface of the colloidal particle. Beside the classical Schulze–Hardy rule describing the counterion effect, the influence of co-ions on particle aggregation has been recently investigated.[121] This phenomenon can also be described by the eq 9 with *n* = 1 dependence, which is much weaker in the case of co-ions.

Realizing that the surface charge is primarily neutralized by the monovalent counterions may also help understand the inverse Schulze–Hardy rule. In that case, eq 9 follows since their concentration is *z*-times greater than the corresponding salt concentration.[123] The inverse Schulze–Hardy rule was confirmed in experiments conducted for the negatively charged sulfate latex and positively charged amidine latex particles in the presence of different multivalent salts.[121] This approach was also proposed for the negatively charged boron nitride nanospheres in the presence of salts of different compositions and valences, and it was confirmed that the destabilization ability of the co-ions followed the inverse Schulze–Hardy rule.[120]

In numerous investigations conducted on various particles such as carbon nanotubes[126], fullerenes[127], or titania[115] the validity of the classical Schulze–Hardy rule was confirmed. Note that despite the large number of reports published in the past concerning the Schulze–Hardy rule in particle aggregation processes, the increasing number of novel nanoparticle systems requires similar studies since they are often applied in electrolyte mixtures. In addition, very few results are available on the effect of co-ions, i.e., the inverse Schulze–Hardy rule was investigated only for a few particle systems. Summarily, comprehensive experimental studies determining surface charges and aggregation rates are needed in this field.

2.4.2. Influence of polyelectrolytes

Polyelectrolytes represent polymers with dissociated ionic groups located on the side chains or on the spine.[128] They contain numerous charged groups, such as sulfonate groups, carboxyl groups, or amines. Polyelectrolytes represent an interesting type of macromolecules that exhibit several advantageous phenomena due to their dual nature involving the features of both highly charged electrolytes and macromolecular chains. Based on these properties, polyelectrolytes can be divided into natural (e.g., polypeptides, polysaccharides, polynucleic acids), modified natural (e.g., cellulose or chitin derivatives), and synthetic polymers (polystyrene sulfonate (PSS), polyimidazolium-based polymer, poly(ethylene imine) (PEI) or poly(diallyldimethylammonium chloride) (PDADMAC)). On the basis of the ionization constant of their functional groups, they are also divided into the groups of strong and weak polyelectrolytes. Their diversity in charge and structure allows multiple applications in different fields of industries, including the pharmaceutical, paper, food, cosmetic, and water treatment industries, as well as medicine.[128] Examples of various polyelectrolytes are shown in Figure 9.

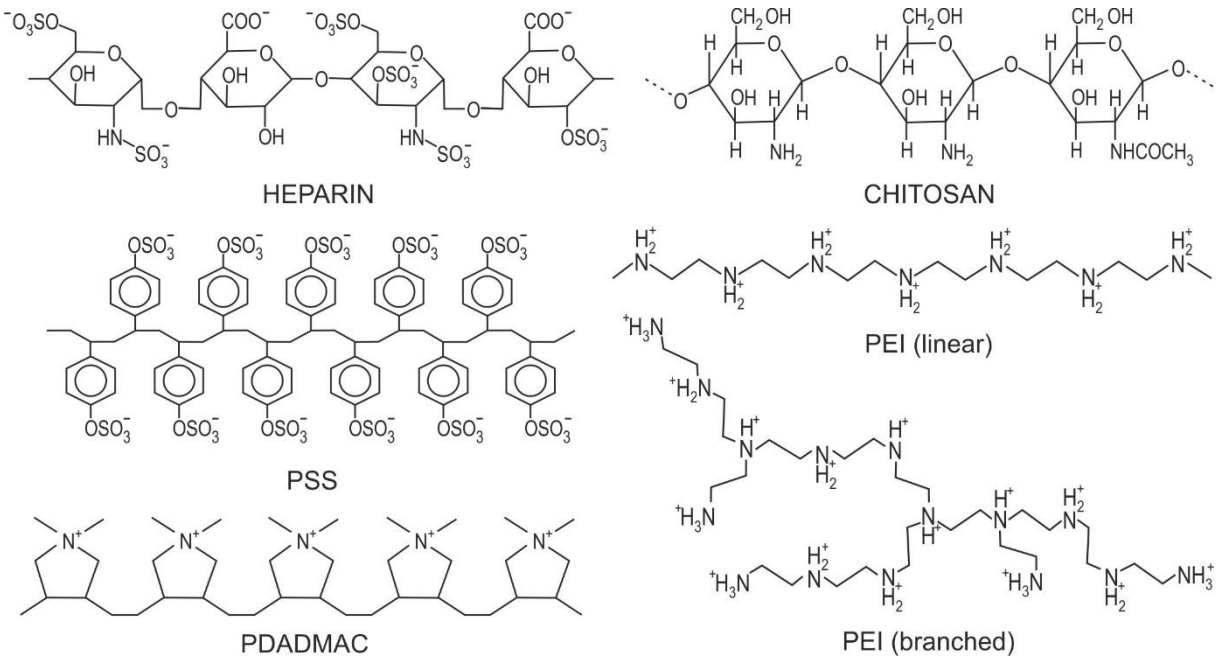

Figure 9. Chemical structure of various polyelectrolytes. The negatively charged ones include heparin, and PSS, while PDADMAC, chitosan, and PEI are positively charged at appropriate pH.

In terms of the colloidal systems, polyelectrolytes have found great number of applications as stabilizing agents to prevent the occurrence of aggregation or coagulation. The polyelectrolyte coating of nanoparticles takes place through the adsorption process on oppositely charged surfaces[129,130], even though there are some cases of adsorption on like-charged surfaces, often intermediated by the cations, as well.[131] Accordingly, functionalization of the particle surface with polyelectrolytes can affect colloidal stability in different ways. Regarding the HNT surface, some studies validated the successful functionalization with various polyelectrolytes such as heparin[132], chitosan[133, 134],or PEI.[79]

Let us discuss the influence of one these polyelectrolytes on the HNT suspensions. For instance, in case of HNT functionalization with cationic PEI (Figure 10), the effect of polyelectrolyte layer on the colloidal were assessed by electrophoretic and dynamic light scattering (DLS) techniques. When the polyelectrolyte dose is appropriate, oppositely charged particles typically exhibit effects of neutralization and charge reversal as a result of strong polyelectrolyte adsorption onto their surface.[130] At low PEI doses the particles remained negatively charged at low doses of the polyelectrolyte due to the partial neutralization of the original charges on the particles. When the polyelectrolyte concentration rises, a sharp increase in the mobility values is observed, indicating the adsorption of the polyelectrolytes leading to the charge neutralization at the isoelectric point (IEP) and charge reversal at suitable doses. At higher PEI doses (higher than 200 mg/g), the mobility values remained constant, indicating the

formation of a saturated layer of the polyelectrolyte on the oppositely charged surface.[79] After reaching the adsorption saturation plateau (ASP), further added polyelectrolyte no longer adsorbed on the surface and remained dissolved in the bulk solution.

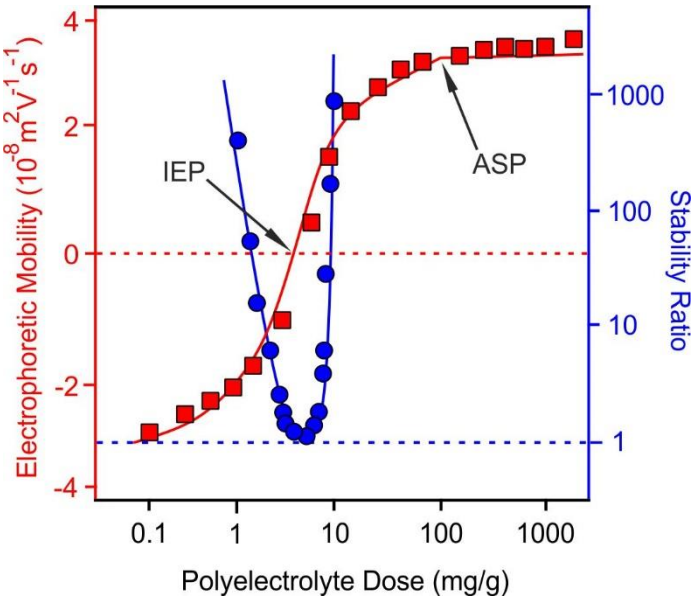

Figure 10. Electrophoretic mobility and stability ratio of a negatively charged HNT upon adsorption of a cationic polyelectrolyte at different concentrations. The data were taken from reference 79.

Regarding the aggregation tendencies in the polyelectrolyte-particle systems, the stability ratios determined in time-resolved DLS measurements indicate rapid aggregation at the dose corresponding to the point of charge neutralization. The stability ratio was close to unity at a minimum (polyelectrolyte intermediate dose), while dispersions at lower and higher polyelectrolyte doses were stable when the particles had an adequately high surface charge. These results can be qualitatively described by the DLVO theory, hence, with charge neutralization the EDL repulsive forces are insufficient and the van der Waals attractions become dominative forces (*chapter 2.3.*).

Similar behavior was observed in the case of chitosan-coated HNT, and it has been reported[134] that its adsorption neutralizes the negative charge of the HNT resulting in an inversion of the surface charge. Numerous studies conducted on other types of particles have confirmed this type of behavior.[135,136] In addition, there are some cases where the adsorption of the polyelectrolyte is also associated with forces that are not of the DLVO type, such as patch-charge, bridging, or steric forces.[130] However, a detailed explanation of these phenomena will be omitted as they were not investigated in the present thesis.

Due to the complex interactions and different nature of the particles and the polyelectrolytes, there are still uncertainties about the influence of the polyelectrolytes on the colloidal stability of particles, especially novel nanoparticles.

2.4.3. Influence of ionic liquids

How the overall colloidal stability of nanoparticles can be affected by a new type of solvent, such as ionic liquids, in a situation where nanoparticles are dispersed in an ionic liquid

medium, as well as their subsequent application, will be discussed in this chapter.

ILs represent an enticing class of compounds entirely consisting of ions. The most accepted definition of ILs is that they are organic salts of low melting points below 100 °C. [137,138,139,140,141] When the melting point is at or below room temperature, they are also known as room temperature ionic liquids. Most often ILs consist of large, organic cations and organic or inorganic anions.[142] The asymmetric dimensions and structure of the ions themselves prevent the formation of an ionic crystal structure, which could explain the low melting point and liquid state of these systems at room temperature. There are various natures of IL cations that can be found such as pyrrolidinium, imidazolium, oxazolium, piperidinium, pyridinium, or with substituted ammonium, phosphonium, or sulfonium cations, while the anions involved in the ILs can be organic or inorganic. Figure 11 shows the structure of the cations most commonly found in ILs and also used in the present thesis.

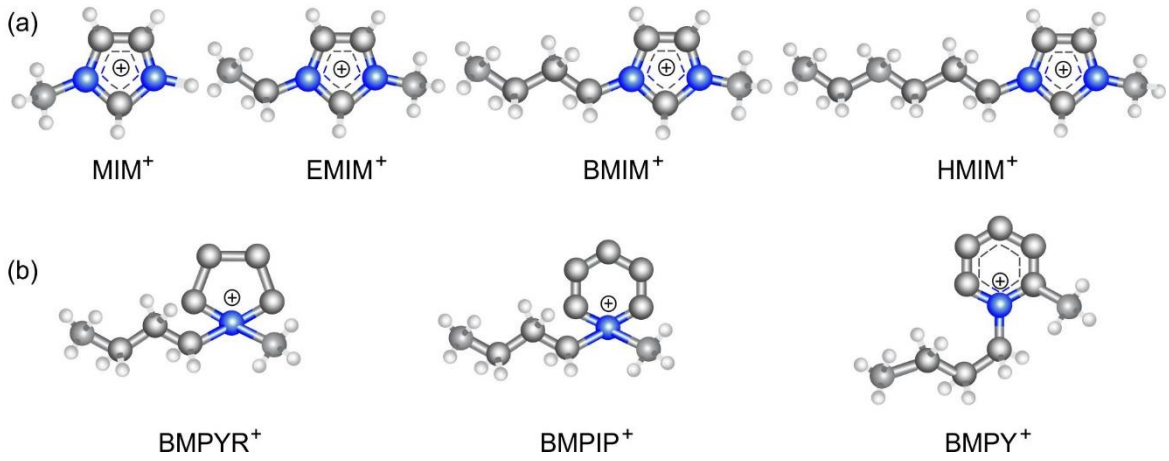

Figure 11. Chemical structure of various IL cations used in the present thesis. Imidazolium-based IL cations with different alkyl chain lengths: MIM^+, $EMIM^+$, $BMIM^+$, and $HMIM^+$ (a), as well as IL cations with different cationic structures: $BMPYR^+$, $BMPIP^+$, and $BMPY^+$ (b). The chloride was used as anion in all cases. The abbreviations are defined on page 4.

One of the greatest features of ILs is the possibility of designing the structure, i.e., different combinations of cations and anions can yield a huge number of different ILs, making them the largest class of solvents in chemistry today.[143,144] A particular advantage of using ILs is that depending on the desired physicochemical properties, a suitable IL with the intended structure can be synthesized by varying anions or cations.[145] Owing to specific physical and chemical properties such as liquid aggregate state, high thermal and chemical stability, low vapor pressure, low melting point, and solubility of organic and inorganic components, ILs have become a „green" alternative to volatile organic solvents in many applications.[138, 146] In addition, ILs have been used in recent years as a platform for the production of new advanced

materials that can be used in many fields such as functional components in seawater desalination or tunable nanoreactors.[147]

In some cases where water is not a suitable continuous medium in colloidal dispersions, ILs can be used instead as solvents.[140, 148] Numerous studies have attempted to clarify the mechanisms leading to the colloidal stabilization of nanoparticles in ILs. The combination of nanomaterials and ILs represent unique and functional systems that are used in many applications such as energy storage, biomolecule processing, or catalysis.[149, 150,151] Despite the significant interest in the study of IL-colloid systems, important studies of the colloidal behavior of particles in ILs have only recently been reported.[152,153,154,155,156,157,158] The interfacial assembly of the constituents of IL was revealed that has a great impact on the colloidal stability of the dispersions and this issue can be suitably followed in diluted aqueous IL solutions by investigating the influence of interfacial properties on the forces between particles. During the development processes of novel materials, nanoparticles are often dispersed in ILs leading to the formation of colloidal dispersions, glasses, and gels, depending on the composition of the samples and the experimental conditions.[159,160,161, 162,163] In addition to the ILs, stable colloids were also obtained in molten inorganic salts due to the charge density oscillations around the dispersed particles.[164]

Investigation of the colloidal stability of the systems containing nanoparticles dispersed in ILs is therefore a crucial issue, due to the fact that some applications require homogeneously distributed primary particles, for example in catalysis[165], while in others particle aggregates are necessary to prepare materials by self-assembly of nanoparticles.[166,167] For this reason, the basic charging and aggregation properties in ILs have attracted considerable attention and became the subject of investigations. Some of these examples are studies of the stability of iron oxide[157,168], latex[154], ruthenium[169], gold[158], or silica particles[155, 170,171,172] in IL at room temperature using different methods. In addition, the governing surface forces induced by ILs were investigated and two types of stabilization mechanisms were proposed based on the results obtained with planar alumina and silica surfaces. First, the repulsive interaction was assumed to originate from the ordered interfacial layering of IL constituents and the subsequent occurrence of oscillatory forces.[173,174] The thickness of the interfacial IL ion pairs can be several nanometers depending on the size of the anions and cations. Second, the formation of a diffuse double layer of dissociated IL ions around charged surfaces has been proposed, and the presence of this layer leads to strong repulsive forces.[175] The latter mechanism is based on an interpretation similar to that predicted by DLVO theory[176,177,122], explained for charged particles

immersed in an electrolyte solution in *chapter 2.3.* It is generally agreed that long-range repulsive forces exist between the surfaces in ILs, but their origin is still an open question.[178] To further explain the nature of the interaction forces in ILs, the interfacial behavior of the IL constituents must be well understood. In order to explore the basic colloidal behavior, the affinity of IL cations and anions to the particle surfaces was examined, and the findings with polystyrene[179], melamine[180], and silica[181] particles showed that the ion specific adsorption of the IL constituents from aqueous solutions determined the surface charge properties, while the major interparticle forces were defined by DLVO theory. These particle-IL interactions allowed the extension of the original Hofmeister series to include IL cations and anions.[179,182,183] As for the quantitative description of particle aggregation processes in dilute IL solutions, there is a limited number of studies.[158,154,155] Therefore, precise measurements of aggregation rates are needed to study the effects of IL constituents on the colloidal stability of particle dispersions.

Concerning the applications of systems containing HNT particles and ILs, they have attracted considerable interest in various fields, such as corrosion inhibitors[184], catalysts with superior catalytic activity[16], and highly conductive materials.[185] Also, they found an application for the development of catecholamine biosensor,[186] or bionanocomposite ionogels used as supercapacitors in flexible electrochemical devices[187] (Figure 12).

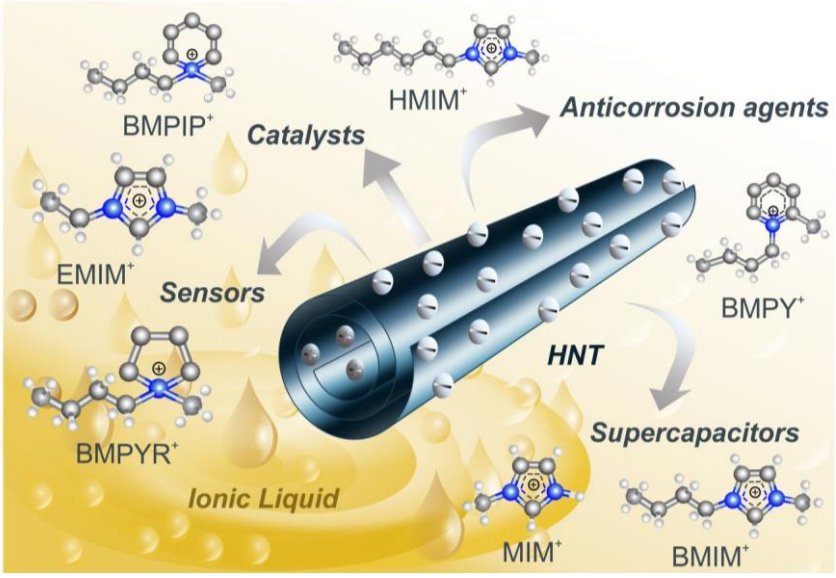

Figure 12. Illustration of the potential applications of the HNT nanoparticles in IL solutions.

To the best of our knowledge, a thorough experimental investigation of the colloidal stability of HNT nanoparticles in ILs, with a well-described or controlled solid-liquid interface has not yet been completed, and many questions remained open concerning the affinity of IL constituents to the surface and the subsequent influence on the interparticle forces.

2.5. The oxidative stress

Several decades ago, the presence of reactive oxygen species (ROS) including free radicals in biological systems was recognized as the primary factor in the development of the toxic effects of oxygen.[188,189] The regulatory biochemical processes include the process of oxidation, which supports the production of energy that is essential for bodies. ROS are produced throughout these processes, and they have their own beneficial physiological effects.[189] However, the issue emerges when the balance is disrupted and natural defense of the body deteriorates and the number of ROS starts to surpass its ability to neutralize them. This alters the oxidative status and places the body in a state of oxidative stress. Oxidative stress is a state of the organism induced by an imbalance between the formation of ROS (oxidants) and their neutralization by the antioxidant protective mechanism.[190] The elevated presence of ROS leads to chain reactions that alter thousands of biomolecules and damage DNA, RNA, enzymes, and/or lipid components of the cellular membrane.[191] For this reason, ROS and other free radicals are now believed to be directly related to numerous degenerative diseases including cancer, neurological disorders[192,193], diabetes, chronic pulmonary disease, and asthma.[194]

In general, ROS can be produced in living systems both endogenously (during physiological processes, e.g., cellular respiration) and exogenously (when their production is caused by the introduction of xenobiotics and other substances into the body). Research led by McCord and Fridovich,[195] who found the enzyme superoxide dismutase, raised insights and interest in the significance of ROS. In 1990, Storz et al.[196] demonstrated that different gene induction in bacteria occurs under the influence of hydrogen peroxide. However, some ROS can also be generated under the influence of exogenous sources, i.e., external influences that cause the increased formation of ROS including drugs, some therapeutic and environmental radiation (ionizing radiation and hyperoxia), smoking, pollution, and an unhealthy lifestyle.

From biomedical aspects, many ROS are of particular significance such as free radicals, like superoxide radical anion or superoxide ($\bullet O_2^-$), or hydroxyl radical (•OH), as well as non-radicals such as hydrogen peroxide (H_2O_2) and singlet oxygen ($^1O_2$).[197] Superoxide represents one of the primary groups of ROS that can be produced by various enzymatic and nonenzymatic pathways. $\bullet O_2^-$ is formed during the one-electron reduction of oxygen.[198] The primary site for generating $\bullet O_2^-$ is the mitochondria during the production of adenosine triphosphate and the mitochondrial electron transport chain usually transfers electrons for the reduction of oxygen to water. However, 1 to 3% of all electrons escape the system and result in superoxide.[191] ROS can also be generated as co-products of many enzymes such as NADPH

oxidase and xanthine oxidase, or during the uncoupled endothelial nitric oxide synthase.[198] The NADPH oxidases, found on the cell membranes of polymorphonuclear cells, macrophages, or endothelial cells, are one of the main sources of $\bullet O_2^-$ production.[198,199] $\bullet O_2^-$ are enzymatically converted to H_2O_2 by superoxide dismutase enzyme. Also, the H_2O_2 is a non-radical ROS, and when combined with reduced transition metals, it produces the extremely reactive •OH.[198] Additionally, H_2O_2 can be formed by NADPH oxidase, xanthine oxidase, and amino acid oxidase and using molecular oxygen in metabolic processes in peroxisomes.[191]

2.6. Enzymes

Enzymes are macromolecules that act as biological catalysts, meaning that they have the ability to affect the rate of a chemical reaction.[200] Like all catalysts, enzymes act by reducing the activation energy of a reaction, thereby accelerating it. An enzyme remains unaffected by the catalyzed reaction, so when one reaction is complete, it can initiate another catalytic cycle. Furthermore, enzymes may alter the redox potential of the cofactor by selectively stabilizing the oxidized or reduced forms of a cofactor bound at its active site, but they cannot affect the equilibrium constant of a chemical reaction that is thermodynamically unfavorable.[200] In a typical enzyme-catalyzed process, substrates are attached to the enzyme, and a complex between them is formed. It is an intermediate product, and from this complex, the product of this reaction is formed, while the enzyme remains unchanged. Genetic mutations and insufficient or increased production of a single enzyme can be the main cause of severe genetic disorders. There are a number of diseases, called enzymopathies, that are caused by genetic mutations.

Enzymes are essential in daily life, from the normal functioning of the human body to their application in many industries, including food, pharmaceuticals, agriculture, cosmetics, and in detergent production.[200,201,202,203] However, the utilization of enzymes is very limited due to many interfering factors. Namely, the presence of molecules that are very similar to the substrate of the enzyme, known as inhibitors, can cover the active site and thus, prevent the binding of the actual substrate. Since enzymes work most efficiently in the physiological temperature range, extreme thermal effects can cause denaturation of the enzyme.[204] Another critical factor of optimal enzymatic operation is the pH of the samples. Slight changes in pH can cause dramatic effects on the catalytic performance of enzymes. Among others, the above experimental conditions limit the supplementation of enzymes as well as their use in industrial manufacturing processes. There are possibilities to overcome these limitations and still benefit from the efficiency of enzymes. These include the immobilization of enzymes[205], utilization of

enzyme mimics such as metal complexes, or the development of nanomaterials with enzyme-like capabilities.[206,207] *Subchapters 2.6.2* and *2.6.3* provide more information on the topic of enzyme immobilization and enzyme mimics.

2.6.1. Enzymatic antioxidants

In order to control ROS concentration, the living organism has developed a variety of defense mechanisms that maintain the balance of oxidation-reduction processes.[191] During evolution, nature developed an antioxidant defense system consisting of several levels to eliminate ROS, as well as to repair oxidative damage that has already occurred.[199] By the level and mode of functioning in the human body, antioxidants can be divided into the following categories: preventive antioxidants, which prevent the formation of free radicals; the so-called radical scavengers, which are able to „capture" the free radicals, and „reparative" antioxidants, which act through specific mechanisms by renewing or eliminating damaged vital biomolecules produced under oxidative stress.[208] Preventive antioxidants are those capable of suppressing and preventing free radical generation such as superoxide dismutase (SOD), catalase (CAT), horseradish peroxidase (HRP), and glutathione peroxidase (GPx).[208,209] The scavenging antioxidants represent the group of antioxidants that may scavenge the active radicals to inhibit chain initiation and terminate chain propagation reactions. [208] The majority of antioxidants belong to this group, such as vitamin E, ascorbic acid, and lipophilic ubiquinol.[210] The reparative antioxidants include phospholipases, proteases, enzymes that restore DNA, and transferases.[191,210] The antioxidants can be also divided into endogenous and exogenous antioxidants according to their origin. Endogenous antioxidants are antioxidants generated in the human body while exogenous antioxidants are supplied through food or drugs and their activity is determined by structural characteristics.[210] Additionally, the antioxidant protective system also involves the enzymatic and non-enzymatic antioxidants, and all antioxidants can be divided into cellular, membrane, and extracellular antioxidants. Enzymatic antioxidants belong to the group of cellular antioxidants. The antioxidant enzymes play a crucial role in preventing lipid peroxidation and maintaining the integrity and functionality of cell membranes by lowering the amounts of lipid hydroperoxide and H_2O_2.[188]

The above-mentioned preventative group, which includes SOD, CAT, HRP, and GPx, are some of the key enzymatic antioxidants that act as the first line of defense against ROS.[209] (Figure 13).

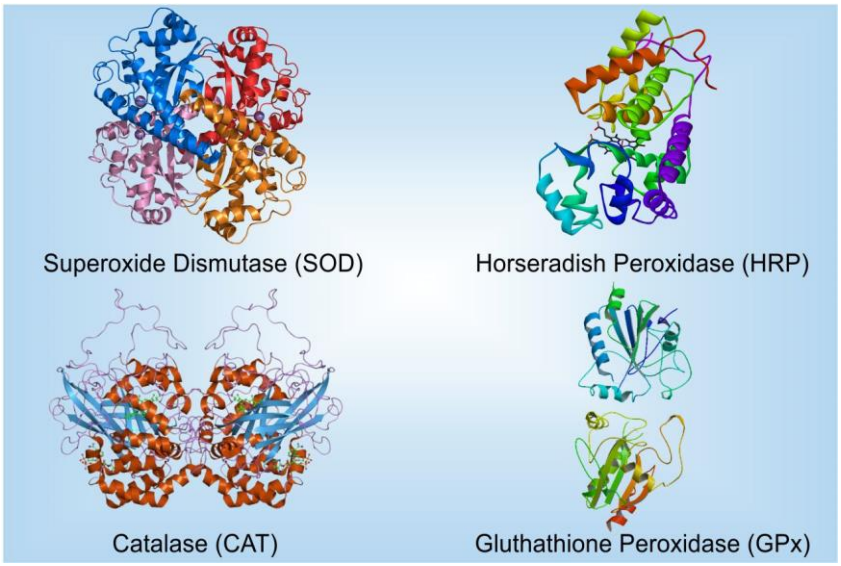

Figure 13. Illustration of common antioxidant enzymes. Note that only the SOD enzyme was used in the present research.

The CAT enzyme can be found in the cell organelles, named peroxisomes, in the cells of plants, animals or aerobic bacteria.[189] The CAT completes the detoxification process started by SOD by catalyzing the breakdown, i.e., the reduction of H_2O_2 to water and molecular oxygen using either iron or manganese as a cofactor.[208] The HRP is one of the numerous peroxidases and its heme group has an iron cation in its active site, which interacts with H_2O_2 to form an enzymatic intermediate capable of oxidizing organic compounds such as guaiacol.[211] The GPx is an essential intracellular enzyme that has the ability to convert peroxides to their corresponding alcohols and H_2O_2 to water, primarily in the mitochondria and occasionally in the cytosol.[208]

Considering that the present thesis deals with SOD and SOD-mimicking metal complexes that were used for immobilization purposes, the main emphasis will be on the properties and principles of action of this enzyme. The first detoxifying enzyme and the most powerful antioxidant in a cell is the SOD. It is a crucial endogenous antioxidant enzyme that serves as a part of the body's initial line of defense against ROS.[208] The SOD is a metalloenzyme and necessitates a metal cofactor to function. It is found in all eukaryotic cells or in all aerobic cells that metabolize oxygen, and in extracellular fluid.[212] It catalyzes the dismutation of superoxide anions to H_2O_2 and molecular oxygen.[213] Since superoxides are the primary ROS and can react also with other molecules to produce another ROS, such as H_2O_2, their dismutation by SOD is of utmost importance to any cell.[212] Considering the type of metal ion needed by SOD as a cofactor, the enzyme has been classified into several groups such as Cu-Zn-, Ni-, Mn-, and Fe-SODs. Distinct genes encode different SOD isoforms in different ways. The SOD1 gene,

which maps to chromosome 21, encodes Cu-Zn-SOD, the SOD2 gene maps to chromosome 6 encoding Mn-SOD, while the SOD3 gene, located on chromosome 4, encodes the extracellular SOD of eukaryotes. Almost all human tissues have a significant amount of SOD3.[208,214] Cu-Zn SOD or SOD1 is typically homodimeric and can be found in various places in various species. Mn-SOD or SOD2 is localized in the mitochondria of aerobic cells, and it usually exists as a homotetramer. EC-SOD or SOD3 is also a homotetramer, and it is mainly localized in the extracellular matrix.[213,214] It is generally believed that Cu-Zn-SOD and Mn-SOD act as bulk scavengers of superoxides, while high levels of EC-SOD in the lung may be an essential component of lung matrix protection.[191] Depending on its oxidation state, the Cu(II) ion is coordinated with three or four histidine residues. The stabilization of protein structures of SOD1 and SOD3 depends on the Zn(II) ion.[215]

Antioxidant enzymes are broadly used systems in the food industry to prevent food oxidizing, or as food supplements, then in the textile industry to keep material peroxidase-free, and in the cosmetic industry, in some aesthetic treatments.[209] Among them, the SOD enzyme has always attracted considerable attention. The application of the Cu-Zn-SOD enzyme is wide in modern medicine, in therapeutic and prophylactic application in humans, mutagenicity testing, and as a vaccination agent.[213] SOD may regulate cancer progression, hence, can be used as a novel target for cancer treatment.[215] In order to minimize free radical damage and advance the body's overall health, the SOD has also been widely used in cosmetic and supplemental items. It heals wounds, prevents skin hyperpigmentation or depigmentation, and aging, and protects against UV rays. It may improve sports performance by lowering lactic acid buildup.[209,213]

2.6.2. Enzyme mimics

Enzymes are not always ideal for practical use due to numerous limitations such as pH, environmental conditions, isoelectric point, temperature, and substrate specificity. However, based on the structural understanding of natural enzymes, many mimicking compounds with biocatalytic activity have been obtained by chemical and biosynthetic methods. Some of them show significant antioxidant effect in living models and can be used as effective antioxidants in target applications.[216] Enzyme mimics can be used in many areas such as biological reactions, biosensors, medical applications, fuel production, and green and sustainable chemistry.[217]

In recent decades, an extensive research has been conducted to develop nanocomposites that are capable of mimicking the function of enzymes.[206,207] For example, a composite based

on Prussian blue nanoparticles immobilized on amidine-functionalized polystyrene latex particles exhibited significant enzyme-mimic activity.[218] Additionally, it was shown that MoS_2 nanosheets have significant SOD-, CAT-, and HRP-mimicking activity, under physiological conditions.[219] These nanomaterials (also known as nanozymes) with intrinsic enzyme-like properties have great potential for various biomedical applications.[220] Of particular interest in this field are nanozymes designed with the ability to replace antioxidant enzymes such as SOD and CAT enzymes. For numerous diseases, SOD mimics have demonstrated considerable therapeutic benefits. For instance, it was shown that developed nanozymes with SOD-like activity may scavenge amyloid-β peptides-mediated ROS, which when accumulated may trigger the onset of Alzheimer's disease.[221] It was also discovered that Mn_3O_4 nanozyme, with multi-enzyme-like activity (SOD, CAT, and GPx) and redox modulatory effect, internalizes into human cells and provides the effective cytoprotection in a Parkinson's disease model.[222] For indications like ischemia followed by reperfusion, when the harmful molecule is continuously overproduced as a result of the injury, SOD mimics show great potential.[223] Among them, the Mn porphyrins have demonstrated high capability as therapeutic agents for treating other different disorders, including amyotrophic lateral sclerosis, thrombosis, adult respiratory distress syndrome, or inflammation.[217] SOD mimics may be superior to natural enzymes due to, for example, their ability to penetrate the intracellular space, longer half-life in the blood, and lower commercial cost.[216,217,223]

Antioxidant nanozymes can be found in the form of bare or functionalized nanoparticles. In this case, a series of nanoparticles containing Fe[218], Mn[224,222], or Ce[225] and Si[226] oxides have enzyme-like activity and are capable of acting similar to the native enzymes. On the other hand, nanozymes can be developed by forming hybrid materials with immobilized metal complexes and nanoparticles. Many studies have been conducted with nanoparticles containing redox-active metals that exhibit enzymatic activity and effective scavenging activity for ROS, such as Mn_3O_4 nanozymes[222] or citrate-coated biocompatible platinum[227], Prussian blue[228] or Co_3O_4 nanoparticles.[229]

Since the redox principles are used to eliminate the ROS, metal complexes with rich coordination chemistry and a redox-active metal site might be considered as one of the effective SOD mimics. Hence, metal complexes with structures comparable to the active center of antioxidant enzymes can be adopted as antioxidant agents.[230,231] For example, copper(II) complexes with monomeric and dimeric structures showed the potential to mimic the catalytic activity of the SOD enzyme.[232] There are two approaches for mimicking the catalytic activity

of enzyme, which are based on whether the enzyme's function or the active site is mimicked. A number of metal complexes that have activity in the chosen process that is comparable to or nearly identical to the enzyme activity resulting in "functional mimicking". On the other hand, a metal complex with a comparable structure to mimic the structure of the active center is called "structural mimicking".[233]

The active center of the SOD enzyme is composed of Cu(II) and Zn(II) ions linked by an anion called a histidyl imidazolate[234] (Figure 14). The Cu(II) ion is further coordinated by three L-histidine molecules and one water molecule. In addition to the imidazolate bridge, the Zn(II) ion is linked to two L-histidine molecules and an L-aspartic acid molecule. The Zn(II) arranges the peptide chains around the active center and protects its structure, but the Cu(II) participates directly in the catalytic electron transfer and can change the coordination number, geometric configuration of the ligands, and valence state of the system.[235]

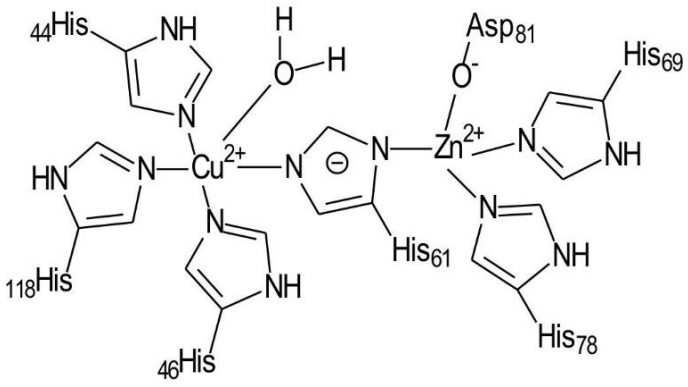

Figure 14. The structure of the active center of Cu-Zn SOD enzyme.

It was reported that analogous ligands can be added to actual ligands to produce SOD activity.[236] A compound with the same central ions but less complicated ligands than those found in the real Cu-Zn SOD enzyme can successfully mimic the prosthetic group. The ligands maintained the properties of those present in the enzyme while being smaller and less complicated, which reduced the computational cost of molecular modeling while still reliably pointing to potential causes of catalytic activity. This was found when Cu–Zn SOD model, Cu(II)-diethylenetriamino-m-imidazolato-Zn(II)-tris-aminoethyl amine complex was immobilized on various supports such as montmorillonite [237] and silica gel.[238] The bare complex had SOD activity, but it was significantly poorer than the enzyme. However, upon immobilization on silica gel and montmorillonite, the activity increased significantly. As already mentioned above, some of the most favorable enzyme-like systems are composed of transition metal[239,240] or their complexes.[241,242,243]

2.6.3. Immobilization of enzymes and enzyme mimics

To broaden the utilization of native enzymes including SOD by overcoming their sensitivity to environmental circumstances, decades ago interest in this field shifted to the immobilization of enzymes, enzymatic antioxidants, or enzyme mimics. Due to their advantageous properties, immobilized systems have found a wide range of applications in many industries, and they are used to manufacture various products. For instance, papain immobilized on chemically modified charcoal has been efficiently employed in industrial wastewater treatment.[205] A commercial pectolytic enzyme was immobilized onto porous anion exchange resins and used in the food industry.[244] Immobilized lipases on magnetic nanoparticles were employed in biodiesel production.[245] An example of their utilization in the pharmaceutical industry is glucose oxidase immobilized on magnetic nanoparticles or in hydrogels based on SiO_2 nanoparticles.[246]

One of the main advantages of the immobilization process in many applications is that the reaction can be easily controlled and stopped by simply isolating the biocatalyst, which increases the productivity. It is essential to have a high enzyme binding capacity, to be chemically stable and biocompatible, and allowing effortless separation of the immobilized enzyme from the reaction mixture. These points are particularly important to elude denaturation of the enzyme, which may occur owing to alterations in the enzyme conformation when adsorbed on the support surface. A number of organic or inorganic materials have been utilized as supports for the immobilization of a variety of enzymes.[247] In recent years, nanomaterials have become increasingly versatile in this field as a huge number of biocatalytic molecules have been associated with nanotubes, nanoparticles, and nanofibers.[248,245]

Due to their beneficial properties mentioned above (*subchapter 2.2.2.*), HNTs are promising candidates as solid carriers for biomolecule immobilization.[41,47] Characteristics such as wide-ranging availability, the maximum surface area per unit of mass, the minimum diffusion limitations, the maximum amount of bound enzyme, and the high mechanical stability possessed by the nanotubes make them ideal carriers. In addition, the nanotubes can be easily separated by simple filtration due to their length. Due to the dual charge of the HNTs, which has been described in detail in *subchapter 2.2.2,* the selective immobilization of charged molecules is possible, for example, some negatively charged proteins were adsorbed in the tube lumen[68] (Figure 15). Many reported studies have confirmed that molecules can be loaded inside the HNT using different approaches, such as intercalation, or tubular entrapment.[68,45, 249] At physiological pH, most enzymes are usually negatively charged.[250] The attachment of enzymes

on the external surface or within the oppositely charged lumen has generated great interest in the scientific community.[49,59,67,251] For instance, various enzymes could be immobilized on the outer or inner surface of HNTs such as laccase[252], lipase[253], amylase[67], urease[68], lactamase[79], and glucose oxidase.[254] In all these reports, HNTs were found to be suitable candidates for enzyme transport processes.

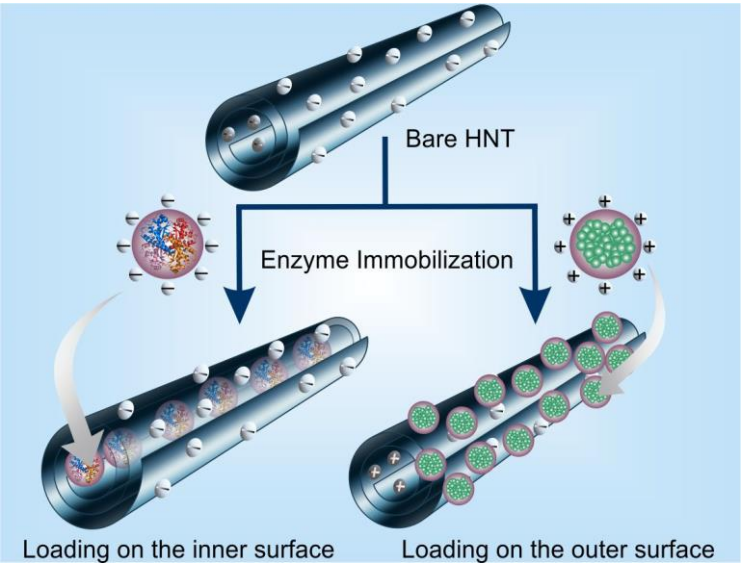

Figure 15. Schematic representation of the two commonly used approaches for enzyme immobilization in/on HNTs.

Despite the favorable aspects of HNTs, many bioapplications require surface functionalization with macromolecules prior to immobilization processes. Such surface modification is important for several reasons, including further immobilization of enzymes or enzyme-like systems, improving the strength of attractive enzyme-particle interactions, and enhancing the colloidal stability of HNTs, as discussed in *subchapter 2.4.2*. The substrate diffusion into the lumen and the product release from the lumen are usually the disadvantages when applying HNTs as supports for enzyme immobilization processes. Despite the positive charge and internal aluminol (Al-OH) groups that can be considered as possible adsorption sites, the pristine (non-treated) HNT still has limitations such as the absence of functional groups with strong adsorption capacity and low surface area and porosity, which result in low loading and weak bonding between biomolecules and nanotubes.[255] Numerous studies, however, have shown interest in the development of possible methods to improve the biomolecule loading of HNTs via surface functionalization or loading of different hydrophilic chemicals (alginate, $CuSO_4$, or $RuCl_3 \cdot xH_2O$) or via embedding metal oxides (α-Fe_2O_3, ZnO, or MgO), or monometals (Au, Ag, or Pd) inside the lumen.[255, 256] However, in the present thesis the studies focused on the outer surface rather than the immobilization in the lumen of HNTs.

The immobilization of enzymes on the surface of nanoparticles serving as solid supports can be performed in a similar way as the adsorption of polyelectrolytes used for the functionalization. There are several approaches that can be employed for the immobilization of enzyme catalysts[205], such as physical adsorption, covalent bonding, cross-linking or enzyme encapsulation[257, 258] (Figure 16).

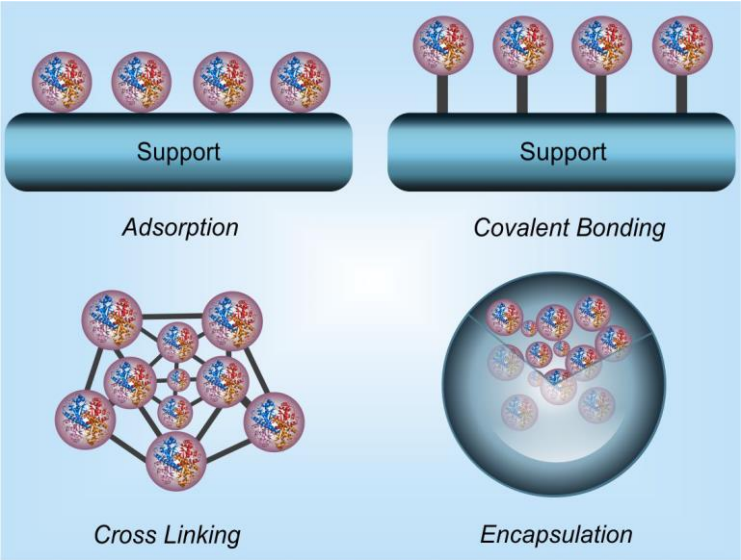

Figure 16. The methods used for the enzyme immobilization.

The immobilization of SOD on various supports is well-reported in the literature. For example, Zhu et al. reported how SOD may be immobilized onto Pt-Pd-multi-walled carbon nanotubes electrochemical sensor. The suggested sensor demonstrated high selectivity and sensitivity for superoxide detection due to the outstanding stability of the interface and superior biocompatibility, which provides SOD with a favorable immobilization environment.[259] In the study conducted on layered double hydroxide (LDH) nanoparticles, it was demonstrated that immobilized SOD was quantitatively adsorbed by electrostatic and hydrophobic interactions while maintaining its structural integrity. According to this research, the developed bionanocomposite, which has considerable enzymatic activity, is an excellent choice for application in biomedical treatments and chemical manufacturing processes, where stable dispersions with antioxidant activity are required.[260] In the case of another type of nanoparticles, such as titania nanosheets, the immobilization of the SOD enzyme on titania nanosheets functionalized with PDADMAC polyelectrolyte was accomplished. The developed nanocomposite demonstrated strong superoxide scavenging activity as a result of the enzyme maintaining its functional integrity after immobilization.[261] Using N-isopropylacrylamide, acrylic acid, dimethyl-butyrolactone acrylate, and the macromer hydroxyethyl

methacrylate-poly, the novel injectable and thermosensitive copolymers (trimethylene carbonate) were developed. The hydrogels included SOD and it showed sustained release kinetics. It was discovered that the SOD loading significantly reduced the penetration of superoxide into the cell membrane and hydrogel.[262] For instance, the SOD enzyme was embedded in the mesoporous silica and the conjugation with a cell-penetrating protein showed great ability in decreasing oxidative stress.[263] Another study demonstrated that SOD retained its activity upon encapsulation into polyacrylamide-based hydrogel nanoparticles.[264] It has also been reported that when SOD is covalently bound to the carbon nanoparticles, the enzyme is prevented from leaking out. The resulting material retained its superoxide-scavenging activity for a prolonged period and was found to be non-toxic.[265] Since the selection of a suitable nanocarrier is crucial, one of the ways to improve this material is surface functionalization. This has proven to be successful in several instances where carrier particles of clay[260] or titanium dioxide[261] have been modified with polyelectrolytes to prevent enzyme degradation and to improve the system's colloidal stability. This latter represents a key issue since the conjugates containing enzymes and nanoparticles are primarily intended to be applied in liquid media where aggregation of the biocatalytic particles results in a loss of enzymatic activity.

Similar to immobilized enzymes, the attachment of SOD-mimicking metal complexes also attracted widespread interest. Therefore, for their immobilization, proper preparation of nanocarriers and their functionalization is very important. Enzyme-mimicking complexes have been performed on multiple different nanocarriers. In particular, silica particles proved to be a good choice as solid supports for the immobilization of various Cu(II)-complexes by physical adsorption.[266,267] Besides, chlorinated polystyrene resin was used to graft Cu-containing enzyme mimics.[268] The surface of the LDH particles was modified by adsorbing poly(vinylpyridine-b-methacrylic acid) before Cu(II)-histamine complexes were immobilized.[269] In comparison to the functional stability determined for the complex in solution, structural alterations in the coordination geometry around the Cu(II) ions during immobilization resulted in improved functional stability in superoxide radical anions dismutation. Furthermore, even at high temperatures (80 °C), where the native or immobilized SOD enzyme lost its antioxidant activity, the obtained hybrid nanomaterial maintained its high level of activity. In a recent paper[270], two redox-active complexes (Cu(II)-bipyridyl and Fe(III)-citrate) were bound and attached by successive adsorption on the LDH nanoclay, functionalized with two polyelectrolytes (PSS and PDADMAC) and the generated antioxidant nanocomposite revealed remarkable activity in scavenging the superoxides.

3. Objectives

My PhD research was primarily focused on conducting a comprehensive investigation of HNT colloids from both a fundamental perspective on dispersion stability in the presence of charged species and an applied perspective on antioxidant composite development. The following sub-objectives assisted in attaining the main objective.

First, a quantitative evaluation of the colloidal stability of HNT particles in the presence of several monovalent (NaCl, KCl, and CsCl) and multivalent ($MgCl_2$ and $LaCl_3$) inorganic electrolytes in aqueous dispersions. The major goal of this study was to assess the affinities of the inorganic cations (Na^+, K^+, and Cs^+), which serve as counterions to the HNT surface, and to examine how these interactions affect the stability of the colloidal dispersions. Based on these results, we intended to clarify and establish the applicability of the Hofmeister series to simple ions in the HNT material as well as to assess the capability of the Schulze–Hardy rule to predict the impacts of multivalent counterions (Mg^{2+} and La^{3+}).

Second, elucidating the function of IL constituent structures in the formation and composition of the solid/liquid interface in HNT dispersions. Aqueous solutions of ILs were used to study the colloidal behavior of HNT. The charge and aggregation characteristics of HNT were examined in the presence of IL cations with various structures and imidazolium-based cations with different alkyl chain lengths. The goal was to involve IL cations in the Hofmeister series we established for HNT material.

The third sub-objective involved surface functionalization to adjust the colloidal stability of HNT particles with both natural and synthetic polyelectrolytes. Prior to enzyme immobilization, the surface of the HNT was modified using a natural PSP polyelectrolyte. Here, strengthening attractive enzyme-particle interactions was the main goal. In order to obtain the HNT-IP-2 particles, a synthetic polyimidazolium-based polyelectrolyte (IP-2) was used. The charging and aggregation properties of these particles were then examined in the presence of inorganic electrolytes with various valences and in aqueous solutions containing imidazolium-based ILs, and the results were compared with those obtained for the bare HNTs. The correct dose of the polyelectrolytes was ascertained by carefully examining the charging and aggregation characteristics at different polyelectrolyte doses.

Fourth, to form stable antioxidant colloids including HNT, polyelectrolytes, and bioactive compounds like enzymes and metal complexes with enzyme-mimicking functions. The development of antioxidant nanocomposites employing natural polyelectrolyte and SOD

enzyme as self-assembling biomacromolecules on HNT as a stable support, was one of the specific objectives. To the best of our knowledge, the immobilization of antioxidant enzymes in/on HNT support has not been reported before. The other sub-objective was the assessment of the influence of HNT-based supports on the SOD-mimicking Cu(Cit) metal complex by adsorbing the Cu(Cit) complex on bare and polyelectrolyte-modified HNTs. The impact of experimental conditions, including biomacromolecule dosage, pH, and ionic strength, on the colloidal and structural stability of the formed nanocomposites, was examined.

4. Experimental Part

4.1. Reagents and solutions

During this work all chemicals (listed in Table 1) were utilized as received. Ultrapure water (resistivity of 18.2 mΩ·cm) supplied from the VWR Purity TU+ instrument was applied for the sample preparations and measurements were conducted at 25 °C and pH 7. To elude the dust contamination during the light scattering experiments, all solutions such as water, salts and ILs were subjected to the filtration with a Millex syringe filter of 0.1 μm prior to sample preparation.

The raw HNT clay was purchased from Sigma-Aldrich. Alkaline treatment was performed utilizing a previously reported technique[79] to enhance surface properties. In short, 20 g/L of commercial HNT powder was dispersed in a 14.5 mM KOH solution for 24 hours under magnetic stirring. The prepared dispersion was then centrifugated for 10 minutes at 10 000 rpm and obtained slurry was redispersed in water after removing the supernatant and washing steps were repeated until the pH of the supernatant was close to 7. All slurries were then collected, placed in a glass container, and heated at 110 °C for 15 hours to generate a dry powder. The resulting hydroxylated HNTs were then dissolved in water at a concentration of 10 000 mg/L and used for further sample preparation. Hereafter (unless otherwise specified), the „h-HNT" term refers to the hydroxylated HNT. Then the basic charging and aggregation features were measured in stable dispersions by light scattering for both raw and hydroxylated HNT to ensure the improvement in particle size distribution after the alkaline treatment. The measured mobilities for both raw and h-HNT were $-2.5 \pm 0.07 \times 10^{-8}$ $m^2/(V \cdot s)$, while the hydrodynamic radii were 225 ± 5 nm for raw particles and 146 ± 9 nm for h-HNT. The polydispersity index was 20 ± 0.6 % for h-HNT, lower than the one measured for raw HNT (25 ± 0.8 %), confirming our prediction that the enhancement was successful.

The complete description of the synthesis of the polyimidazolium-based polyelectrolyte (IP-2) was previously described.[271] In brief, a Schlenk-flask was used to dissolve 1,4-bis(chloromethyl)benzene and 1-(trimethylsilyl)imidazole in acetonitrile in a molar ratio of 1:1, and the mixture was then heated to reflux for 48 hours. The white solid product obtained was extracted by filtration, then washed using diethyl ether and acetonitrile, and dried for 24 hours under a vacuum. The chemicals utilized in the synthesis were purchased from Sigma-Aldrich.

Table 1. List of compounds used throughout this research work.

Compound	Form	Purity	Supplier
Halloysite nanoclay	$Al_2Si_2O_5(OH)_4 \cdot nH_2O$	99.9%	Sigma-Aldrich
Potassium chloride	KCl	≥ 99.5%	VWR™
Sodium chloride	NaCl	99.9%	VWR™
Cesium chloride	CsCl	≥ 99.9%	VWR™
Magnesium chloride hexahydrate	$MgCl_2 \cdot 6H_2O$	99.9%	VWR™
Lanthanum(III) chloride, anhydrous	$LaCl_3$	99.9%	Alfa-Aesar
Potassium bromide	KBr	98%	VWR™
Potassium hydroxide	KOH	99.995%	VWR™
Ethanol	EtOH	absolute	VWR™
*BMPYCl	$C_{10}H_{16}ClN$	> 98%	Iolitec GmbH
*BMPYRCl	$C_9H_{20}ClN$	99%	Iolitec GmbH
*BMPIPCl	$C_{10}H_{22}ClN$	99%	Iolitec GmbH
*MIMCl	$C_4H_7ClN_2$	> 95%	Iolitec GmbH
*EMIMCl	$C_6H_{11}ClN_2$	> 98%	Iolitec GmbH
*BMIMCl	$C_8H_{15}ClN_2$	≥ 99%	Iolitec GmbH
*HMIMCl	$C_{10}H_{19}ClN_2$	> 98%	Iolitec GmbH
Protamine sulfate	$C_{264}H_{460}N_{128}O_{65}S_7$	≥ 98%	Sigma-Aldrich
Xanthine oxidase	enzyme	0.4–1.0	Sigma-Aldrich
Xanthine	$C_5H_4N_4O_2$	99%	Alfa-Aesar
*NBT	$C_{40}H_{30}Cl_2N_{10}O_6$	90%	Acros Organics™
Coomassie Brilliant Blue	$C_{45}H_{44}N_3NaO_7S_2$	-	Fisher Scientific
Ortho-phosphoric acid	H_3PO_4	85%	Carl Roth
Trisodium citrate dihydrate	$Na_3C_6H_5O_7 \cdot 2H_2O$	≥ 99.0%	VWR™
Copper(II) chloride dihydrate	$CuCl_2 \cdot 2H_2O$	99%	VWR™

*****BMPYCl: 1-butyl-2-methylpyridinium chloride; BMPYRCl:1-butyl-1-methylpyrrolidinium chloride; BMPIPCl: 1-butyl-1-methylpiperidinium chloride; MIMCl: 1-methylimidazolium chloride; EMIMCl: 1-ethyl-3-methylimidazolium chloride; BMIMCl: 1-butyl-3-methylimidazolium chloride; HMIMCl: 1-hexyl-3-methylimidazolium chloride; NBT: Nitro blue tetrazolium chloride monohydrate

4.2. Measurement techniques

4.2.1. Electrophoretic light scattering

An automated procedure for studying the surface charge characteristics of colloidal particles is electrophoretic light scattering (ELS).[82,130,272] The method allows the measurement of electrophoretic mobility and the zeta potential derived from it. It is based on the motion of charged particles in a liquid subjected to an external electric field. Coulomb forces cause charged particles suspended in an electrolyte to be attracted to the electrode with the opposite charge when an electric field is applied to the suspension/sample. ELS method is based on various operating principles, such as phase analysis light scattering and laser Doppler velocimetry, which is the most commonly used. Because of the Doppler effect, the frequency or phase shift between the reference light and the light scattered by the particles is used to determine the velocity. The dielectric constant and the viscosity of the medium, and strength of the electric field or voltage gradient all affect velocity of the charged particles. The electrophoretic mobility (u) and the velocity (v) of charged particles are proportional to each other and depend on the applied electric field (E). This dependence can be expressed as follows[83]:

$$v = uE \tag{10}$$

The practical mobility of an isolated charge moving due to the electric field is determined by the ratio between the charge (Q) and the friction coefficient (f), and it is given by the following relation[99]:

$$u = \frac{Q}{f} = \frac{ze}{6\pi\eta R} \tag{11}$$

The appropriate model used when determining the zeta potential or electrokinetic potential from the electrophoretic mobilities must take under advisement the size of the particles, the magnitude of surface charge, and ionic strength varied in dispersion.[82] The Debye length (κ^{-1}) is used to incorporate the concentration of electrolyte by the ionic strength (I), which is expressed as follows:

$$\kappa^{-1} = \sqrt{\frac{\varepsilon\varepsilon_0 k_B T}{2N_A e^2 I}} \tag{12}$$

Strong ionic strength causes small Debye screening length and low potential, ($|\zeta| \leq 50$ mV), but large particles (κR>>1). Here, ζ can be determined using the Smoluchowski model[83]:

$$\zeta = \frac{u\eta}{\varepsilon_0 \varepsilon} \tag{13}$$

However, when the ionic strength is low and particles are small (κR<<1), Hückel provides an applicable calculation model:

$$\zeta = \frac{2u\eta}{3\varepsilon_0 \varepsilon} \tag{14}$$

And in the case when κR ≈ 1, the appropriate model for calculation is given by Henry, as follows[273]:

$$\zeta = \frac{2u\eta}{3\varepsilon_0 \varepsilon} f(\kappa R) \tag{15}$$

where $f(\kappa R)$ denotes Henry's function. Depending on the ionic strength and particle size, this value can vary from 1 to 1.5. The aforementioned case, however, only applies to potentials with magnitude lower than or equal to 50 mV.

If the potential is high, a model proposed by O'Brien and White must be applied.[272] Figure 17 represents the comparison of three different models that can be used for zeta potentials calculation. In the present thesis, the results are presented using the electrophoretic mobilities, and the zeta potential values are obtained using the Smoluchowski model. These data are presented in the Supplementary Information chapter.

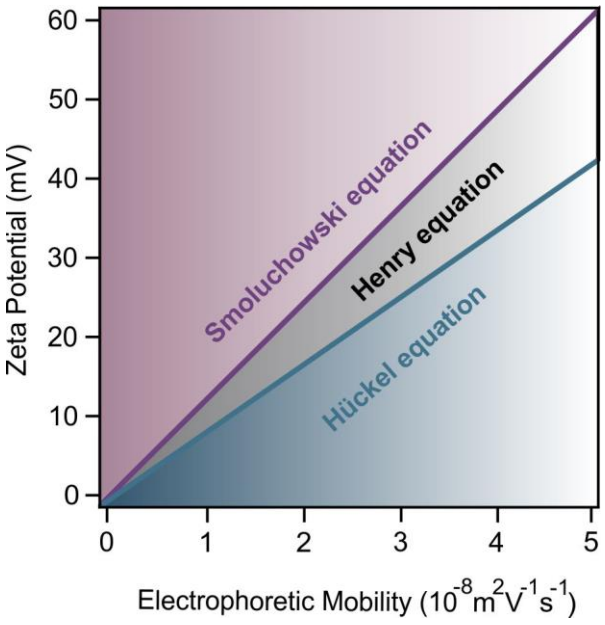

Figure 17. Comparison of different models for obtaining zeta potential from electrophoretic mobility.

The electrokinetic potentials can be used to evaluate the surface charge density of the particles, which is one of the fundamental parameters. The relation between the potentials and the ionic strength is described by two hypotheses. The surface charge density (σ) of charged planar surfaces submerged in electrolyte solutions was determined using the Gouy-Chapman

model. The hypothesis states that potential decreases with ionic strength. Grahame's equation is another term for the relation that describes this[274]:

$$\psi_0 = \frac{2k_BT}{e}\sinh\left(\frac{e\sigma}{2k_BT\varepsilon\varepsilon_0\kappa}\right) \tag{16}$$

The following Debye-Hückel model, which applies to spherical colloids or plane surfaces, characterizes the change in potential with electrolyte concentration, as follows[8]:

$$\sigma = \varepsilon\varepsilon_0\kappa\psi_0 \tag{17}$$

Poisson-Boltzmann theory, which defines the potential profile as a function of distance from the surface in the EDL, is the basis of both models. Equation (16) is used for high potential ranges[176,177,81], while equation (17) is used for lower potential ranges. Figure 18 represents a comparison of these models. Both the Debye-Hückel and Gouy-Chapman models allow valid results for low potentials, while the Gouy-Chapman theory is more useful for high potentials. Therefore, in this thesis, the surface charge densities of the various systems are calculated using the Gouy-Chapman model.

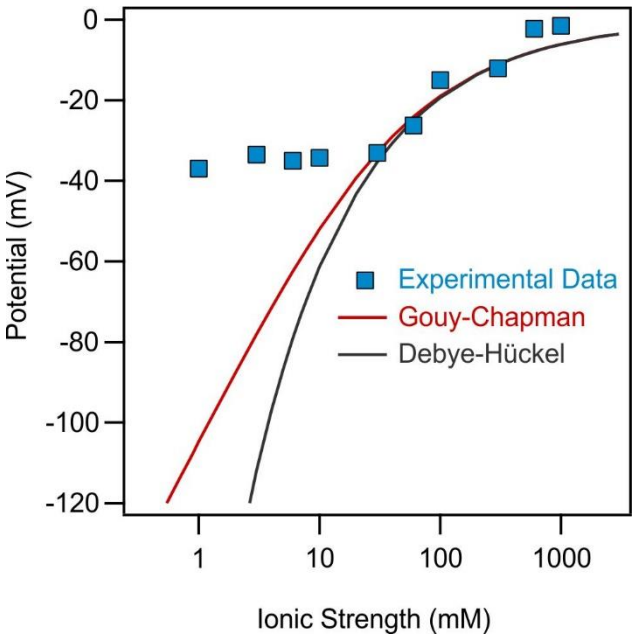

Figure 18. Electrokinetic potential values as a function of the ionic strength. Experimental points (blue squares) were measured by electrophoresis with negatively charged h-HNT particles in KCl solution at pH 7. The solid lines were calculated with the Gouy-Chapman (red line) and the Debye-Hückel models (black line) using a surface charge density value of -14 mC/m^2.

The ELS measurements were carried out utilizing an Anton Paar-purchased Litesizer 500 device which function with a 40 mW semiconductor laser with at wavelength of 658 nm and operates in backscatter mode with a scattering angle of 175°. The phase shift is determined using the continuously monitored phase analysis light scattering method. For all systems that were examined, the sample preparation process was the same. In general, each sample typically contained 1.8 ml of polyelectrolyte, salt, or IL solutions (at the proper concentration) and an additional 0.2 ml of a stable h-HNT dispersion at a

concentration of 100 mg/L. Omega-shaped plastic cuvettes (Anton Paar) with a volume of 700 µL were utilized to measure the samples. Before the samples were utilized for the electrophoretic mobility measurements, they rested for two hours at 25 °C. The results of the measurements were visible after one minute of equilibration in the instrument. The average values of five different measurements are presented.

4.2.2. Dynamic light scattering

The hydrodynamic radius (R_h) of particles was determined by applying the dynamic light scattering (DLS) measurement technique. Using the Tyndall effect and Brownian motion, as characteristics of colloids, the DLS method can measure the size of the particles and characterize the colloidal suspensions, in the submicron range.[275]

Figure 19 shows the basic configuration of a simple DLS instrument, which consists of a laser emitting coherent monochromatic light. When this light hits dispersed particles, they act as a new source of illumination due to scattering.[276] Most of the electromagnetic waves pass through the sample unaltered, but some of them are scattered and collected by the detector. The interference of the scattered waves with the particles causes the intensity to fluctuate over time as the relative positions of the particles change.

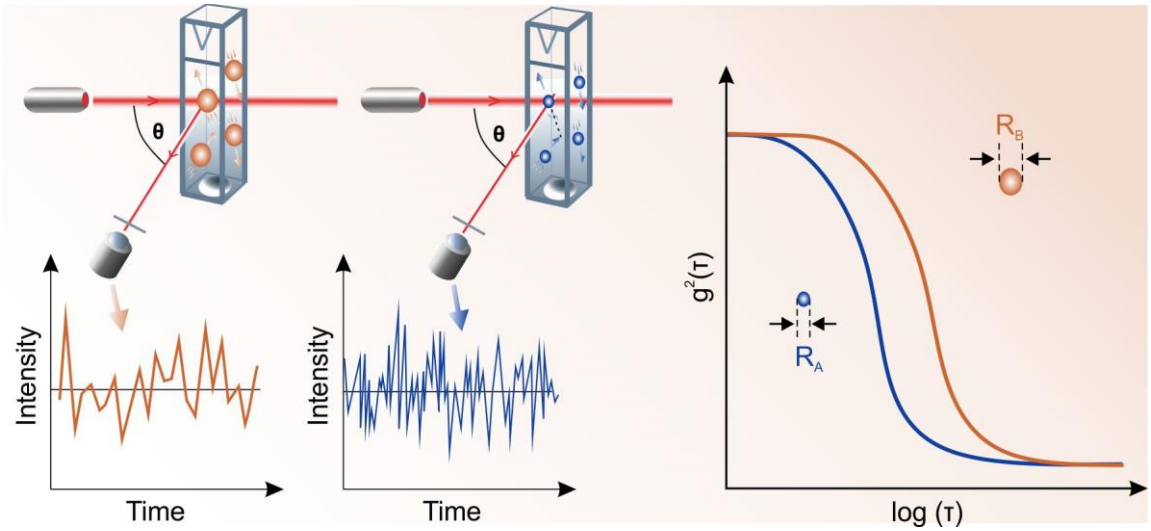

Figure 19. Schematic illustration of the DLS setup in backscattering mode with obtained fluctuation in scattering intensity and corresponding correlation functions for particles of different sizes.

The diffusion coefficient (D) of the particles, which is connected to the hydrodynamic radius(R_h), determines the fluctuations in the intensity of the scattered light.[275] Consequently, small particles fluctuate faster because they have a higher diffusion coefficient. The autocorrelation method can be used to collect quantitative data on these fluctuations. It is

necessary to take into account both the intensity at a specific time ($I(0)$) and the intensity after a short delay ($I(0+\tau)$) in order to understand the autocorrelation function of the varying scattering intensity. The following relation[277] can be used to express the intensity correlation function for these intensities:

$$\langle I(0)I(\tau)\rangle = \lim_{x\to\infty} \int_0^{T'} I(t)I(t+\tau)d\tau \tag{18}$$

where T′ is the entire measurement time, τ refers to the time delay, and t is the actual time. It can be observed that when τ reaches 0, the entire function is equal to $\langle I^2\rangle$, whereas if it tends to infinity, the function has a value of $\langle I\rangle^2$. Below is an example of the normalized intensity correlation function[276]:

$$g^2(\tau) = \frac{\langle I(0)I(\tau)\rangle}{\langle I^2\rangle} \tag{19}$$

Besides the correlation function for the intensity which is determined, also, a correlation function for the electric field was obtained which gives a correlation between particle positions at different τ[276]:

$$g^1(\tau) = \exp(-Dq^2\tau) \tag{20}$$

here, D represents the diffusion coefficient. The Siegert relation[276] connects the intensity correlation function $g^2(\tau)$ and the electric field correlation function $g^1(\tau)$:

$$g^2(\tau) = A[1 + B(g^1(\tau))^2] \tag{21}$$

where A refers to baseline and B denotes a coherence factor. This correlation function decreases exponentially, as shown by the following equation when considering a suspension of monodispersed spherical particles:

$$g_1(t) = exp(-\Gamma t) \tag{22}$$

where (Γ) refers to the decay rate constant and it is given by[278]:

$$\Gamma = q^2 D \tag{23}$$

Therefore, the Stokes-Einstein equation may be used to calculate the diffusion coefficient of monodisperse colloidal particles, as follows[278]:

$$R_h = \frac{k_B T}{6\pi\eta D} \tag{24}$$

where T is the temperature (expressed in *K*), η is the viscosity of the medium, and k_B is the Boltzmann constant.

Time-resolved light scattering techniques have been demonstrated to be suitable for determining the aggregation rates of dimer formation in the DLS mode, allowing researchers to study the early stages of aggregation. The dimer formation occurs when attractive forces predominate over repulsive forces. Aggregation is an irreversible process and the largest aggregates form at the final stages of aggregation. For the h-HNT particles, however, only the first stage of aggregation is discussed in this chapter. The aggregation process became irreversible since each collision between the main particles (A) produced a dimer (AA), and this can be described by the following relation[279]:

$$\frac{dN_{AA}}{dt} = \frac{1}{2} k N_A^2 \tag{25}$$

where N_A refers to the number concentration of monomer and N_{AA} is the number concentration dimer, *t* is time, and *k* is the aggregation rate constant. The Smoluchowski equation (eq 8 in *chapter 2.3.*) can be used to calculate the aggregation rate constant of dimer formation when the particles are subjected to Brownian motion and diffusion controlled aggregation at high ionic strength above the CCC. By combining a static (SLS) and dynamic (DLS) mode, the absolute particle aggregation rate may be determined.[280] However, the focus is on the calculation of the apparent rate constant (k_{DLS}) from time-resolved DLS measurements, which can be performed using the following equation[279, 281]:

$$k_{DLS} = \frac{1}{R(q,0)} \left(\frac{dR(q,t)}{dt} \right)_{t \to 0} \tag{26}$$

where t is time, q is the scattering vector, and $R(q,0)$ and $R(q,t)$ are the initial and subsequent hydrodynamic radii, respectively[278]:

$$q = \frac{4\pi n}{\lambda} sin\left(\frac{\Theta}{2}\right) \tag{27}$$

where λ is the light wavelength, n refers to the refractive index of the sample, and θ represents a scattering angle. It is important to know the scattering vector, which is obtained from the DLS setup, to calculate the diffusion coefficient using the Siegert equation, which was discussed earlier.[282]

The colloidal stability of the samples is usually expressed in terms of the stability ratio (W) which can be determined from the following relation[89,86,279,283,284]:

$$W = \frac{k_{DLS}^{fast}}{k_{DLS}} = \frac{\left(\frac{dR(q,t)}{dt}\right)_{t\to 0,fast}}{\left(\frac{dR(q,t)}{dt}\right)_{t\to 0}} \tag{28}$$

where k_{DLS} is the apparent rate constant derived from the measurement and k_{DLS}^{fast} denotes the fast (diffusion limited) rate at high ionic strength over the CCC.

When (W) is equal to unity, the process of aggregation becomes diffusion limited, resulting in fast aggregation (Figure 20). Therefore, in the case of unstable dispersions, the stability ratio is equal to 1, meaning that all particle collisions result in the creation of dimers. The presence of stable colloidal dispersions is indicated by results with higher stability ratios. At varied ionic strengths, IL concentrations, polyelectrolyte, or enzyme doses, the stability ratios can be determined. The salt/IL concentration or dose value at which transition from the slow $(W > 1)$ to fast $(W = 1)$ aggregation regimes occurs, is the so-called critical CCC (*chapter 2.3.*), which can be calculated by the following equation[285]:

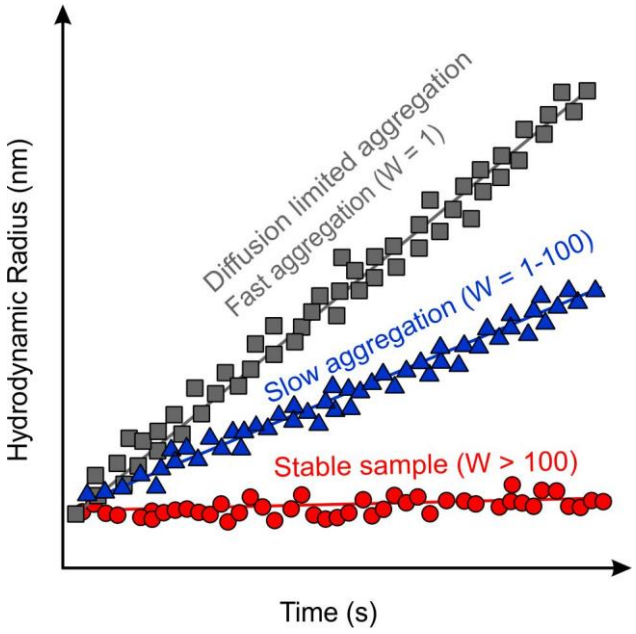

Figure 20. Schematic illustration of different suspension stabilities.

$$W = 1 + \left[\frac{CCC}{c_{salt/IL}}\right]^{\beta} \tag{29}$$

where $c_{salt/IL}$ refers to the salt or IL concentration, depending on the system, and the exponent β can be obtained from the slow aggregation regime (i.e., before the CCC) of the $(logW)$ versus $logc_{salt/IL}$ graphs as[285]:

$$\beta = \frac{dlog\ 1/W}{dlog\ c_{salt/IL}} \tag{30}$$

These examinations were carried out using the same the above-mentioned Litesizer 500 device that was previously utilized for the electrophoresis, at a scattering angle of 175°. After collecting correlation functions for 20 s to calculate hydrodynamic radii, the cumulant analysis was used to determine the decay rate constants. Depending on the speed of aggregation, the measurements were conducted for 40-100 min while the particle concentration (10 mg/L) remained constant. The samples were prepared following the prescribed procedure as for the ELS investigations. However, the DLS measurements were carried out immediately upon adding the h-HNT stock and mixing sample by Vortex for approximately 25 s, and the samples were equilibrated in the instrument for 30 s before data gathering started.

4.2.3. Refractive index and viscosity

An Abbemat 3200 refractometer was employed to determine the n values of the IL solutions. This Anton Paar refractometer is an automatic single-wavelength and operates at 589 nm wavelength. The data applied in equation (27) were introduce with a linear fit on the n versus IL concentration values:

$$n = c_{IL}a\ +\ b \tag{31}$$

where a and b refer to fitting parameters listed in Table S1, and C_{IL} is the molar concentration of the ILs. The obtained n data are presented in Figure S1a**.**

A Brookfield LVDV-II+ProC/P viscometer was utilized to measure the η of IL solutions in a cone-plate geometry, with a CPE-40 type of cone. The Casson viscosity model[286] was applied to fit the shear stress as a function of shear rate, allowing the determination of η for

different aqueous solutions of ILs. Subsequently, the measured values were plotted and fitted using the following equation[287]:

$$\eta/\eta_0 = 1 + A\sqrt{c_{IL}} + Bc_{IL} + Dc_{IL}^2 \quad (32)$$

where A, B, and D are constants specified in Table S1 and η_0 is the viscosity of water. Equation (32) was utilized to interpolate the η value used in equations (13) and (24). Figure S1b shows both the experimental results obtained within the used IL concentration range, with fits obtained from eq 32.

4.2.4. FT-IR and Raman spectroscopy

FT-IR spectra were acquired using BIO-RAD Digilab Division FTS-65A/896 instrument by applying 256 scans at 4 cm^{-1} resolution. The range of wavenumber utilized was from 4000 to 600 cm^{-1}. The presence of adsorbed PSP polyelectrolyte and later immobilized SOD enzyme on the h-HNT-PSP composite was determined by FT-IR spectroscopy. Measured spectra were compared with ones obtained for bare h-HNT particles. Spectra of each sample were recorded in the diffuse reflectance mode that operates with the angle of incidence fixed at 45° Prior to measurement the samples were prepared by mixing 30 mg of the solid composite with 300 mg of KBr.

Raman measurements were conducted with a Bruker Senterra II Raman microscope. The instrument operates with a 100 mW laser at an excitation wavelength of 765 nm and averaging 128 spectra with an exposure time of 6 s. Raman spectra were measured to verify the adsorption of the polyelectrolytes (PSP and IP-2) used for surface functionalization of the h-HNT particles, as well as to confirm the adsorption of the Cu(Cit) complex on the surface of h-HNT-PSP and h-HNT-IP-2. The acquired spectra were compared with those obtained for functionalized particles without the Cu(Cit) complex and ones measured for bare h-HNT particles.

4.2.5. Electron microscopy

Transmission electron microscopy (TEM) was performed using an FEI Tecnai G^2-20 X-Twin instrument, that acquired images in bright-field mode with an accelerating voltage of 200 kV and a LaB_6 cathode. The technique was used for morphological analysis of bare and functionalized h-HNT particles. After the surface modification with polyelectrolytes, the dispersions were dried on a copper-carbon mesh grid and measured.

For the same purpose, scanning electron microscopy (SEM) measurements were used, to

confirm that the surface modification did not change the morphology of the particles. In this method, a Hitachi S-4700 device was used, operating at an accelerating voltage of 10 kV. A double-sided carbon tape was used as the sample holder. The samples were coated with gold using a Quorum Technologies SC7620 device by physical vapor deposition, prior to measurements.

4.2.6. Thermal gravimetric analysis

Thermal gravimetric analysis (TGA) was carried out using a TGA/SDTA851e Mettler Toledo device under nitrogen. The method was used to examine the thermal degradation of bare and polyelectrolyte-coated h-HNT particles. The samples were heated to 700 °C at a rate of 10 °C/min after equilibration for several minutes at 30 °C in the instrument. Then the dispersions were centrifuged and dried in a desiccator to generate the solid samples for further testing.

4.2.7. UV-Vis spectroscopy

UV-Vis spectroscopy was used to measure the Bradford test and enzymatic assays. The technique used a Genesys 10S spectrophotometer (Thermo Scientific) and recorded the increase or decrease in absorbance of the agents used during the estimation of enzymatic or antioxidant activity of the composites. The tests were carried out within the wavelength range of 190-1100 nm using a scale of 0.1 nm.

4.2.8. Electron paramagnetic resonance

A Bruker EleXsys E500 spectrometer was used to record electron paramagnetic resonance (EPR) spectra. The instrument uses a 9.54 GHz microwave frequency, 5 G modulation amplitude, 13 mW microwave power, and a modulation frequency of 100 kHz. The EPR measurements were performed to investigate the coordination geometry surrounding the copper(II)ions in the systems containing Cu(Cit) complex. The EPR spectra were measured in the samples with and without nanoparticles. To prevent the water from crystallizing, small amount (0.05 mL) of methanol was added to 0.20 mL of the samples before measurements. Quartz EPR tubes were applied as the sample holders and then spectra were recorded in a Dewar which was filled with liquid nitrogen at 77 K.

4.2.9. Bradford test

The Bradford test[288] was used to determine the quantity of the SOD enzyme adsorbed to the h-HNT-PSP composite. Utilizing a 250 mL volumetric flask, Bradford's solution was

prepared according to the following recipe. Namely, 25 mg of Coomassie Brilliant Blue was dissolved in 15.5 mL of ethanol, then 25 mL of phosphoric acid was added, and the solution was diluted with ultrapure water to the final volume. A calibration curve was prepared utilizing SOD solutions in a concentration range from 1 to 100 mg/L. Samples were prepared by mixing 1.6 mL of the Bradford reagent with 400 μL of a SOD solution of specified concentration. The obtained mixture was then equilibrated for a few minutes and measured by UV-Vis spectroscopy.

The dispersions were prepared by mixing 10 mg of SOD per gram of h-HNT-PSP to achieve a final SOD concentration of 50 mg/L. In this way, it was possible to estimate the amount of SOD adsorbed onto the h-HNT-PSP particles. To measure only the quantity of free SOD (not adsorbed on the h-HNT-PSP particles), these dispersions were centrifuged, and the supernatant was collected and filtered utilizing a syringe filter (0.1 μm). Then, 1.6 mL of the Bradford reagent was added to 400 μL of this supernatant. The amount of free SOD in the samples was determined by the difference between the absorbances recorded at 595 nm and 465 nm wavelengths.

4.3. Enzymatic assay: SOD activity

A biochemical assay developed by Beaucham and Fridovich[289], was used with some minor modifications to test the activity of the superoxide radical scavenging activity. The compounds applied in the protocol, such as xanthine, NBT, and xanthine oxidase, were prepared utilizing the 10 mM concentrated phosphate buffer solution with an adjusted pH of 7± 0.1. The procedure was as follows: 0.2 mL of 3 mM xanthine, a given quantity of antioxidant composite, then 0.1 mL of 3 mM NBT, and a certain volume of water were added. This mixture with a volume of 2.7 mL was mixed well and finally, 0.3 mL of 3 mg/mL xanthine oxidase was added as a reaction initiator. Following this procedure, samples were prepared with a final volume of 3 mL each. Superoxide radical anions were generated as a result of oxidation reaction of xanthine to uric acid by xanthine oxidase as an initiator. The generated radicals reduced NBT to formazan, and this was accompanied by alteration in color from yellow to blue. UV-Vis spectroscopy was used to monitor the increase in the absorption band at 565 nm. The estimation of the inhibition of the NBT-superoxide radical reaction at various antioxidant concentrations required the estimation of blank reference samples. They were prepared by the same method, but without the antioxidant composite and with an additional amount of water to keep the volume to 3 mL. Six blank samples were prepared and recorded, and the absorbance alterations were utilized to calculate the inhibition at various antioxidant concentrations. In order to

quantify the SOD-like activity, the IC_{50} values which represent the concentration of the redox-active component needed to obliterate half amount of the generated radicals during the reaction were utilized. The inhibition was estimated with the following equation:

$$I = \frac{\Delta A_0 - \Delta A_s}{\Delta A_0} \cdot 100 \tag{33}$$

where ΔA_0 refers to the absorbance difference recorded for the blank samples averaged from six measurements, and ΔA_s represents the absorbance difference recorded at 565 nm after 6 minutes for samples containing the antioxidant composite. The average error of these evaluations was less than 5%.

4.4. Preparation of polyelectrolyte functionalized h-HNT particles

The surface of h-HNT particles was functionalized with two different polyelectrolytes, but the principle of functionalization was the same (Figure 21).

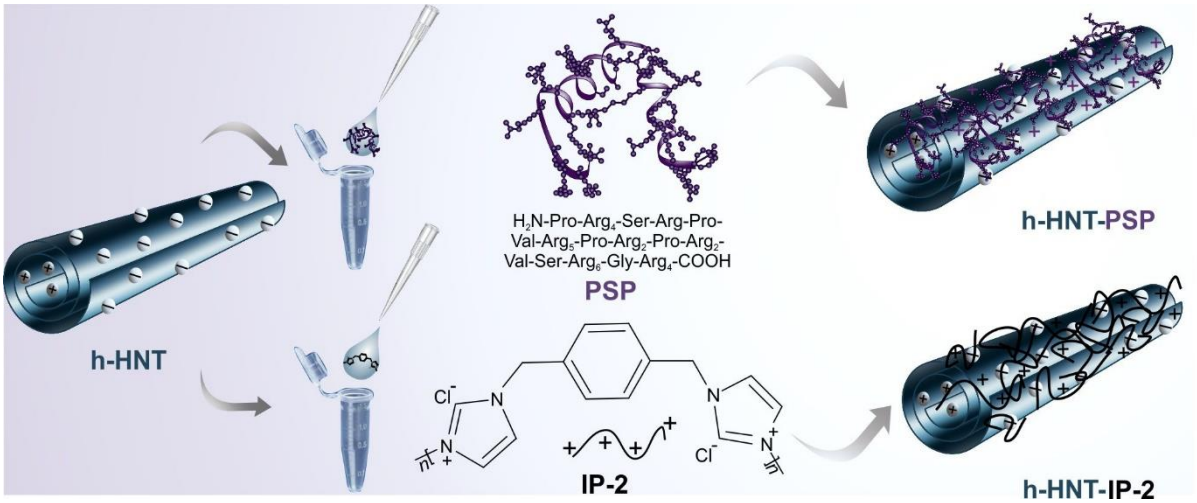

Figure 21. Schematic representation of the surface functionalization of h-HNT particles with two types of polyelectrolytes.

Both, natural (PSP) and synthetic (IP-2) polyelectrolytes are positively charged at physiological pH. ELS and time-resolved DLS were used to monitor the adsorption process of polyelectrolytes on the oppositely charged h-HNT surface. The polyelectrolyte dose of PSP was gradually increased from 1 to 1000 mg/g during the experiments, while the IP-2 dose was changed from 0.1 to 2000 mg/g. A constant particle concentration of 10 mg/L was maintained at neutral pH. KCl was used to regulate the ionic strength at concentrations of 1 mM for PSP or 10 mM for IP-2. The dose of polyelectrolyte required for complete functionalization was selected in accordance with the charging and aggregation data obtained. PSP polyelectrolyte

was, therefore, used at a dose of 100 mg/g, i.e., 100 mg PSP per 1 g h-HNT. Consequently, h-HNT-PSP particles were prepared by simply mixing the predicted amounts of 1 g/L PSP solution and 10 g/L h-HNT dispersion with water dilution.

ELS and time-resolved DLS studies for IP-2 polymer indicated that 200 mg/g was the required dose for complete particle coating. The method used to prepare the h-HNT-IP-2 particles at this dose was the same as the previous one; it consisted of mixing the required volumes of a 1 g/L IP-2 solution and a 10 g/L h-HNT dispersion followed by dilution with water. Both h-HNT-PSP (at 100 mg/g) and h-HNT-IP-2 (at 200 mg/g) were prepared as stock dispersions at concentrations of 1 g/L and then diluted in the experiments.

5. Results and Discussion

5.1. Colloidal stability of h-HNTs in the presence of inorganic electrolytes

The present chapter discusses the fundamental dispersion characteristics of bare h-HNT particles and the influence of mono- and multivalent salts on the colloidal behavior of particles. The direct Hofmeister series[106] for the monovalent ions in the presence of negatively charged h-HNT particles will be established. In addition, the dependence of dispersion destabilizing power on the ionic valence will be interpreted by the DLVO-based Schulze–Hardy rule.[112]

5.1.1. Dispersion characteristics of bare h-HNTs

Figure 22 shows the pH-dependent electrophoretic mobility and hydrodynamic diameter values determined for the h-HNT particles in the pH range of 3–11.

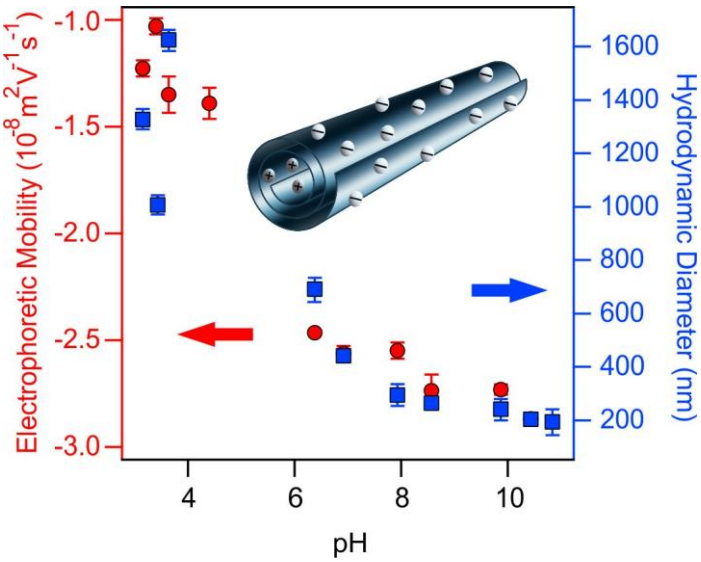

Figure 22. Electrophoretic mobility (red circles, left axis) and hydrodynamic diameter (blue squares, right axis) data of h-HNT as a function of the pH. The measurements were carried out at 1 mM ionic strength.

The presence of deprotonated Si–O–H groups on the outer surface of h-HNT induces a negative surface charge in the range of pH 3–11. It was not possible to detect positively charged protonated Al–O–H groups present on the inner surface of h-HNT, because electrophoresis can only measure the net charge of the particles.[52] In the pH range 4–6, the mobility values decrease since the pK_a value of the silanol**,** groups diminishes in this range,[290,291] while above pH 7 the mobilities remained nearly constant.

The electrophoretic mobilities of h-HNT designate a relatively high surface charge within a wide pH range in the alkaline region. All further colloidal stability investigations were conducted at pH 7. The particles have considerable negative charge under these conditions, as confirmed by the mobility value of $-2.55 \pm 0.03 \times 10^{-8}$ $m^2/(V \cdot s)$.

The trend observed for the measured size values as a function of pH is similar to the trend described above for electrophoretic mobility. The hydrodynamic size decreased with pH as the

surface charge increased, which prevents particle aggregation due to strong EDL repulsion. Since higher average hydrodynamic diameter values were observed at lower pH values due to weaker EDL forces, it is an indication that some aggregates are present. The hydrodynamic diameter and polydispersity index, measured at pH 7, were 442 ± 9 nm and 15 ± 0.9 %, respectively. The length of the h-HNT particles, as the longest dimension of the material, can be determined by DLS, since the technique uses an equivalent spherical diameter. Also, the polydispersity index refers to the length of the h-HNT particles and the measured value is low and thus, the particle size distribution is within the size range of the DLS. These findings showed that the h-HNT dispersions are suitable for the time-resolved DLS measurements, which we will be discussed later.

5.1.2. Surface charge and aggregation features in the presence of monovalent salts

The charging and aggregation properties of the h-HNT were examined with NaCl, KCl, and CsCl. Figures 23a and 23b represent the measured electrophoretic mobilities and stability ratios for the h-HNT, respectively. Inorganic cations behave as counterions for the negatively charged bare h-HNT in the samples, and their effects on colloidal stability were systematically examined. The ion specific interactions in particle aggregation and stability of the nanoparticle dispersions in salt solutions were studied.

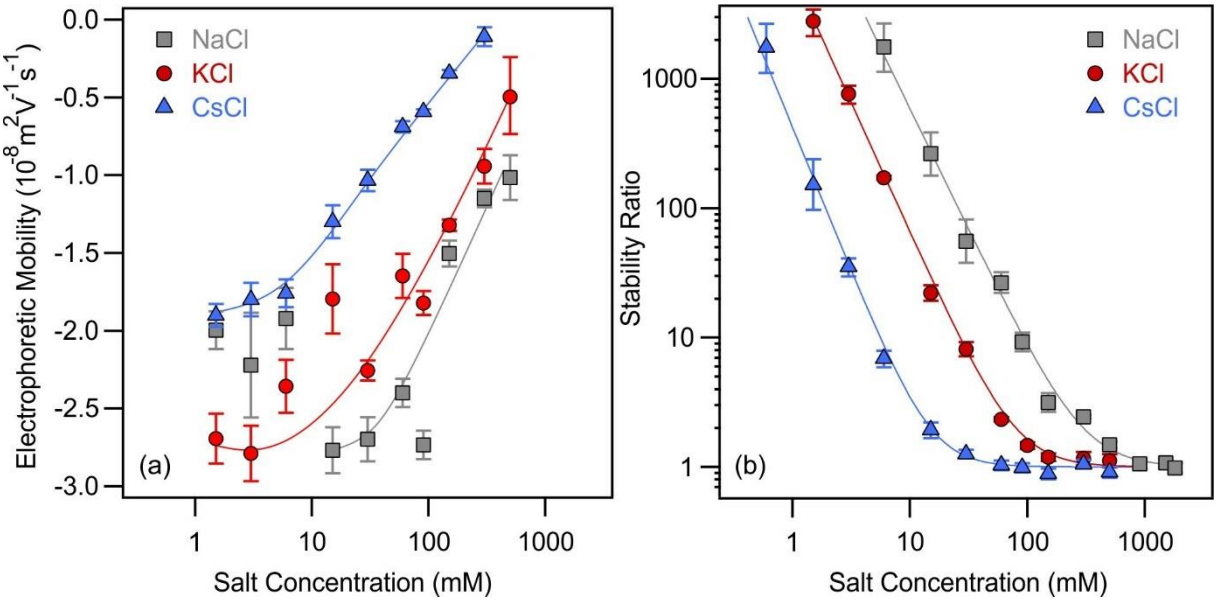

Figure 23. Electrophoretic mobility (a) and stability ratio (b) values of bare h-HNTs at different concentrations of monovalent salts (Reprinted (adapted) with permission from Ref. 292. Copyright (2022) American Chemical Society). The lines in (a) serve to guide the eyes, while the lines in (b) are calculated by equation (29). The measurements were performed at pH 7 and particle concentration was kept constant at 10 mg/L.

The magnitude of the electrophoretic mobilities decreased with the salt concentration, and they maintained negative values during the entire examined regime (Figure 23a). Despite the similar generic trends, the measured values were system specific at the same ionic strength. The zeta potentials, converted from the mobility data, were also used to interpret the results (Figure S2), and an increase in the magnitude of potentials (at the same salt level) can be noticed in the order $Cs^+ < K^+ < Na^+$ indicating ion specific interactions with the surface of h-HNT particles. The importance of the ion specific interactions is reflected in the extent of the ion adsorption for the monovalent counterions, which results in varying surface charge densities (Table 2), and therefore a significant deviation in the strength of the repulsive double layer forces.

Under the same experimental conditions used for the mobility measurements, time-resolved DLS experiments were performed to investigate the aggregation characteristics in the presence of monovalent salts by monitoring the changes in the hydrodynamic radius. The stability ratio exhibited the same trend across all systems (Figure 23b). Accordingly, a slow aggregation was confirmed by high measured stability ratio values at low ionic strengths; however, as ionic strength increased, the stability ratios decreased and stayed close to unity at higher concentrations, and this well corresponds with the qualitative prediction of the DLVO theory.[83,176,81] At low salt levels, a potent repulsion caused by the overlap of the EDLs around the charged particles leads to the formation of stable dispersion owing to the predominance of EDL forces over the attractive van der Waals forces. In addition, the surface charge screening effect of the salts causes the EDL forces to gradually diminish at high salt concentrations. As a result, rapid aggregation occurs owing to van der Waals forces, which become prevalent. These findings apply generally to all systems, however, the actual values of the stability ratios at certain ionic strengths change while the composition of the electrolytes was varied. The DLVO theory does not consider this effect, i.e., it predicts the same stability ratios in the presence of NaCl, KCl, and CsCl.

5.1.3. Ion specific effects: establishment of Hofmeister series

The CCC values were derived from the stability ratio versus ionic strength plots utilizing equation (29) to estimate the variations in aggregation rates for these systems comprising different counterions (Na^+, K^+, and Cs^+). The obtained CCC values are shown in Table 2 and Figure 24a. The obtained values declined in the following order: $Na^+ > K^+ > Cs^+$. This sequence is in line with the direct Hofmeister series for negatively charged hydrophobic surfaces (Figure 7).[293] Similar results were obtained with other clay particles, namely, CCC values measured for the K^+-montmorillonite clay, in the presence of different alkali ion solutions

(including Na^+, K^+, and Cs^+) showed the same trend.[294]

Table 2. Characteristic aggregation and charging data of h-HNTs particles in monovalent salt solutions.

Salt	NaCl	KCl	CsCl
CCC (mM)[a]	300	80	15
σ (mC/m^2)[b]	-16	-10	-5
ζ (mV)[c]	-13	-15	-17

[a]Critical coagulation concentration calculated by equation (29). [b]Charge density at the slipping plane determined with equation (17). [c]Zeta potential at the CCC. An average error for electrophoretic measurements and for the CCC determination is about 10%.

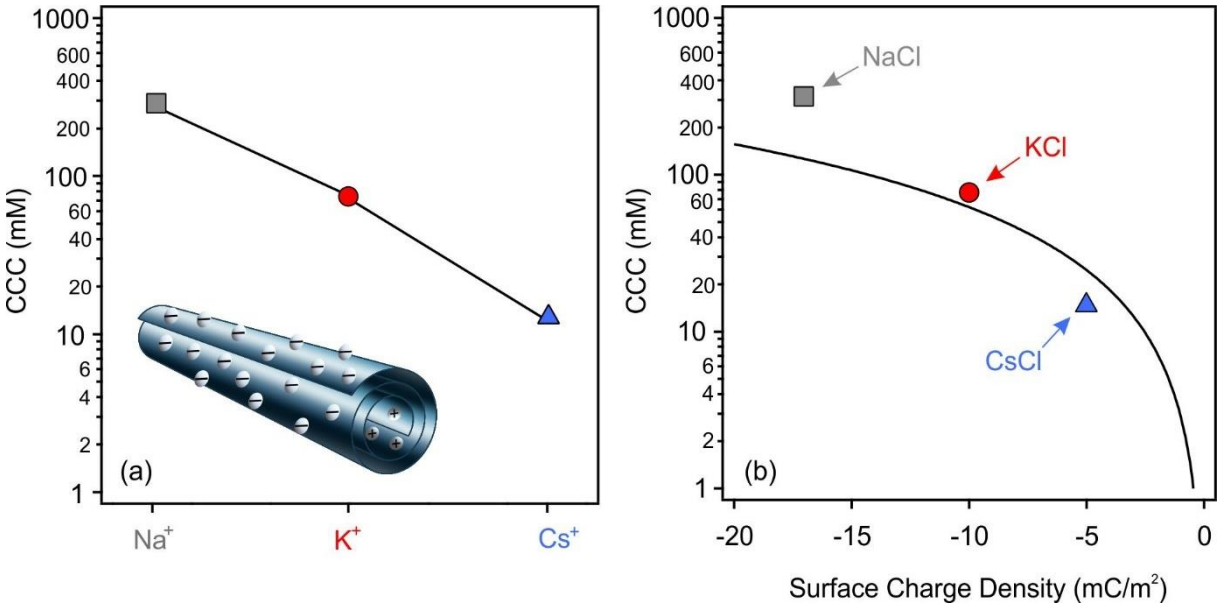

Figure 24. CCC values of bare h-HNT particles obtained with monovalent (KCl, NaCl, CsCl) salts (a), and CCC as a function of surface charge density data (b). The experimental CCC values and charge densities were calculated using equations (29) and (17), respectively. The lines in (a) are for eye guidance only, and the line in (b) is calculated by equation (34).

The significance of ion adsorption for colloidal stability has been highlighted in previous studies with various colloidal particle dispersions.[115, 116, 293] To investigate this, electrophoretic mobilities were first converted to zeta potentials using the Smoluchowski model (eq 13). Thereafter, the surface charge density (σ) value was determined by fitting the zeta potentials measured at different salt concentrations with the Debye–Hückel charge-potential relation[83] (eq 17) (Figure S2). The obtained surface charge density values in the presence of Na^+, K^+, and Cs^+ are shown in Table 2, and it can be noticed that the order of these quantified values was the same as the one for the CCCs previously discussed. Correspondingly, the highest charge was found in the presence of Na^+, and the lowest one in the presence of Cs^+.

Figure 24b illustrates the charge-aggregation relation after plotting the CCC data as a function of surface charge densities and it can be interpreted as follows. The strongest adsorption was observed for the Cs^+ cation and the lowest one for the Na^+. In the case of Na^+, weak adsorption on the negatively charged h-HNTs does not influence the charge of the particles significantly resulting in strong EDL forces which can be screened at higher salt levels generating a higher CCC value. On the contrary, considerable Cs^+ adsorption partially neutralizes the h-HNT surface charge and thus, weakens the EDL forces giving rise to lower CCC.

When the identical particles are dispersed in various monovalent salt solutions, the DLVO theory assumes that the CCC is less dependent on the nature of the ions. Nevertheless, the surface charge of the particles changes during ion specific adsorption, so h-HNT cannot be assumed to behave the same in all systems. The relationship developed from DLVO theory (more details in *chapter 2.3.*), which allows the calculation of CCC values from charge densities, can be used to further investigate the origin of interparticle interactions[83,295]:

$$CCC = 0.365/N_A L_B \, (H\varepsilon\varepsilon_0)^{-2/3}\sigma^{4/3} \tag{34}$$

where L_B is the Bjerrum length which is equal to 0.72 nm for monovalent electrolytes in water at 25 °C.[293] In equation (34), a Hamaker constant of 7.0 x 10^{-21} J was used to achieve the best agreement with the experimental data (Figure 24b).

Since the experimental and calculated results agree (Figure 24b), it can be inferred that the DLVO theory accurately predicts the CCC values once the corresponding charge densities are included in equation (34). This agreement suggests that the aggregation process or the source of the main forces between the particles can be inferred from the DLVO model. However, the positions of the CCCs depend on the affinity of the counterions to the surface, which affects the strength of the EDL repulsion. Various CCC values and, hence, the development of the Hofmeister series of cations for the h-HNT particles were generated as a consequence of the combined influences of DLVO forces and ion specific adsorption on the colloidal stability. In other words, the aggregation mechanism is governed by EDL and van der Waals forces, while the CCC data are influenced by charge neutralization that occurred due to the adsorption of counterions to different extents.

5.1.4. Surface charge and aggregation features in the presence of multivalent salts

The charging and aggregation characteristics were studied with multivalent salts ($MgCl_2$ and $LaCl_3$) and compared to the monovalent KCl discussed above. The obtained electrophoretic mobility and stability ratio values are presented in Figures 25a and 25b, respectively.

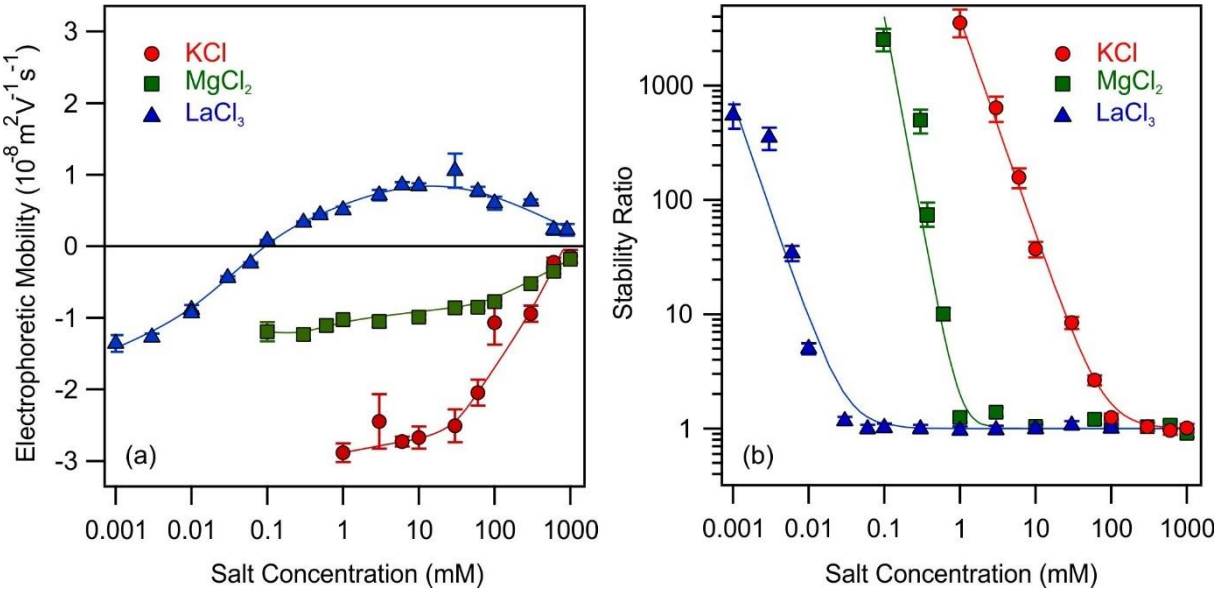

Figure 25. Electrophoretic mobility (a) and stability ratio (b) values of negatively charged h-HNTs as a function of multivalent salt concentration (Reprinted (adapted) with permission from Ref. 296. Copyright (2022) American Chemical Society). The lines in (a) serve to guide the eyes, while the lines in (b) are evaluated by equation (29). The measurements were performed at pH 7 and particle concentration was kept constant at 10 mg/L.

Considering the charge balance, monovalent (K^+) and multivalent (Mg^{2+} and La^{3+}) cations serve as counterions for h-HNTs. In each system, the measured electrophoretic mobilities were negative at low ionic strengths and increased with the addition of salts (Figure 25a). It can be observed that at higher salt concentrations, the mobilities of K^+ and Mg^{2+} were almost zero, whereas in the case of La^{3+}, the adsorption of the multivalent cation resulted in charge neutralization and reversal behavior of the particles at adequately high salt concentrations. This behavior is the confirmation that the affinity of the cations to the surface becomes higher with increasing the valence.

To interpret the results, the zeta potentials were calculated from the mobilities (Figure S3). Furthermore, from the electrolyte concentration dependence of the zeta potentials, the surface charge density at the slip plane was determined and used to interpret the colloidal stability as one of the fundamental factors. As previously described in *subchapter 4.2.1.*, this calculation is possible within the framework of the Debye-Hückel model, which is applicable only for

indifferent ions, whose adsorption on the surface is insignificant.[122] Furthermore, significant deviations between the measured and calculated zeta potentials (Figure S3) appeared at lower ionic strengths due to the electrokinetic effect.[297] The calculated surface charge densities for the bare h-HNTs were –14 mC/m^2 (K^+), –6 mC/m^2 (Mg^{2+}), and –0.062 mC/m^2 (La^{3+}). Since the model provided by equation (17) does not consider the ion specific adsorption, when one compares the quantified and experimental zeta potentials for Mg^{2+} and La^{3+} we can notice that these values are quite inaccurate. This is evident from the discrepancy between the experimental and calculated zeta potentials.

Figure 25b shows the stability ratios for the h-HNT determined in the presence of these inorganic electrolytes. The stability ratios generally followed the same trends, in each case, hence, the values decreased with increasing salt concentrations, and they remained close to unity at high salt levels. Consequently, the occurrences of slow and fast aggregation at low and higher salt concentrations, respectively, agreed with DLVO theory.[81, 176] In relation to the previous subchapter, an explanation of this theory and this type of behavior has already been given (*subchapter 5.1.2.*). The stability ratio curves for the multivalent counterions followed the same general trend as that found for the monovalent counterions. Nevertheless, compared to the CCC found for K^+ (Table 2), the CCCs recorded for the divalent and trivalent ions were significantly lower. As a result, a CCC values of 1 mM for Mg^{2+} and 0.03 mM for La^{3+} were determined. The obtained CCC values show a valence-dependent decrease, which is consistent with the Schulze–Hardy rule.[108,123] A detailed explanation of this phenomenon, in general, is given in *subchapter 2.4.1.* Regarding these systems, more information on the CCC dependence on the valence will be provided below.

5.1.5. CCC dependence on the valence: Schulze–Hardy rule

The DLVO-based Schulze–Hardy rule, which states that CCC values decrease as the valence of the dissolved ions increases (eq 9),[123,122] was used to interpret the dispersion-destabilizing power of inorganic salts with different ionic valence (KCl, $MgCl_2$, and $LaCl_3$). In eq 9, the exponent for weakly charged particles is $n = 1.6$, however, if one takes into consideration asymmetric electrolytes, the exponent for particles with a high surface charge is $n = 6.5$.[124] In the latter case, the number is not typical for h-HNT particles, and it can be calculated from the DLVO theory only for surfaces with exceptionally high magnitude of charge (more details in *subchapter 2.4.1.*).

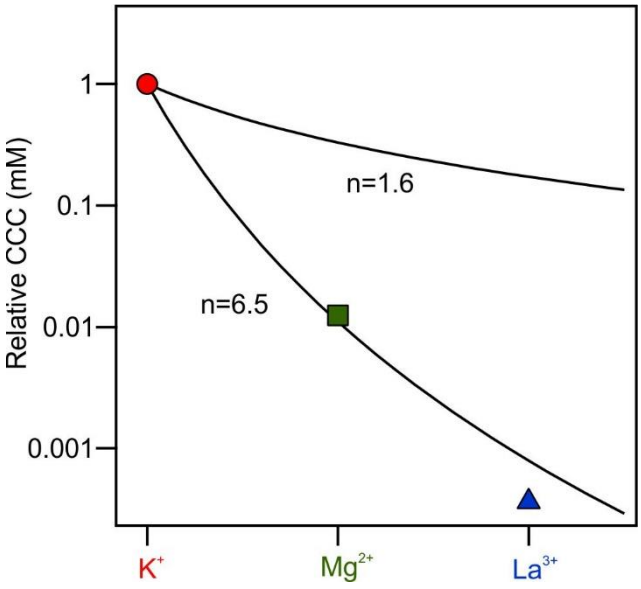

Figure 26. Relative CCCs (normalized to the CCC determined with KCl) of bare h-HNTs for cations of different valences. Solid lines indicate the direct (for n = 1.6 and n = 6.5 in eq 9) Schulze–Hardy rule.

Figure 26 presents the determined relative CCC values, which are normalized to the CCC value found for the K^+, as well as the CCCs predicted by the Schulze–Hardy rule (eq 9) according to the noted limitations. The CCC values declined with valence in the following order: $K^+ > Mg^{2+} > La^{3+}$ (Figure 26). This was as expected, and the decrease fit better to the dependence of n = 6.5 in eq 9.

The surface charge density for h-HNT in attendance of KCl is around –14 mC/m^2, but the n = 6.5 dependence might only be inferred from the DLVO theory for highly charged surfaces (magnitude of surface charge density above 1000 mC/m^2). One may notice here that the adsorption ability of cations, i.e., their affinity, is one of the most important factors in colloidal stability. This leads to a stronger reduction of the surface charge by stronger adsorption of multivalent ions. These findings are well-aligned with the zeta potential values shown in Figure S3. The CCC is lower because the surface charge density decreases due to counterion adsorption, requiring less salt concentration to destabilize the colloids. Owing to the prominent sensitivity to the valence of counterions, the n = 6.5 dependence of CCC on valence represens the combined impact of ion adsorption and prediction of DLVO theory (*subchapter 2.4.1*).

The CCC tendencies, described above, agree well with previously reported results on colloidal particles in the presence of different metal salts[115,116,120,298], or multivalent oligoamine cations.[299]

5.2. Colloidal stability in the presence of IL constituents

The colloidal stability of h-HNT particles in the presence of aqueous solutions of IL constituents was examined and the present chapter summarizes these findings. The direct Hofmeister series established for the h-HNTs will be extended to include the IL cations.

5.2.1. Surface charge and aggregation with IL cations of different structure

The surface charge densities and aggregation rates of h-HNTs were examined in the presence of aqueous solutions of various ILs, such as BMIMCl, BMPYRCl, BMPYCl, and BMPIPCl (structures presented in Figure 11). The electrophoretic mobilities were measured at various IL concentrations and the data are shown in Figure 27a.

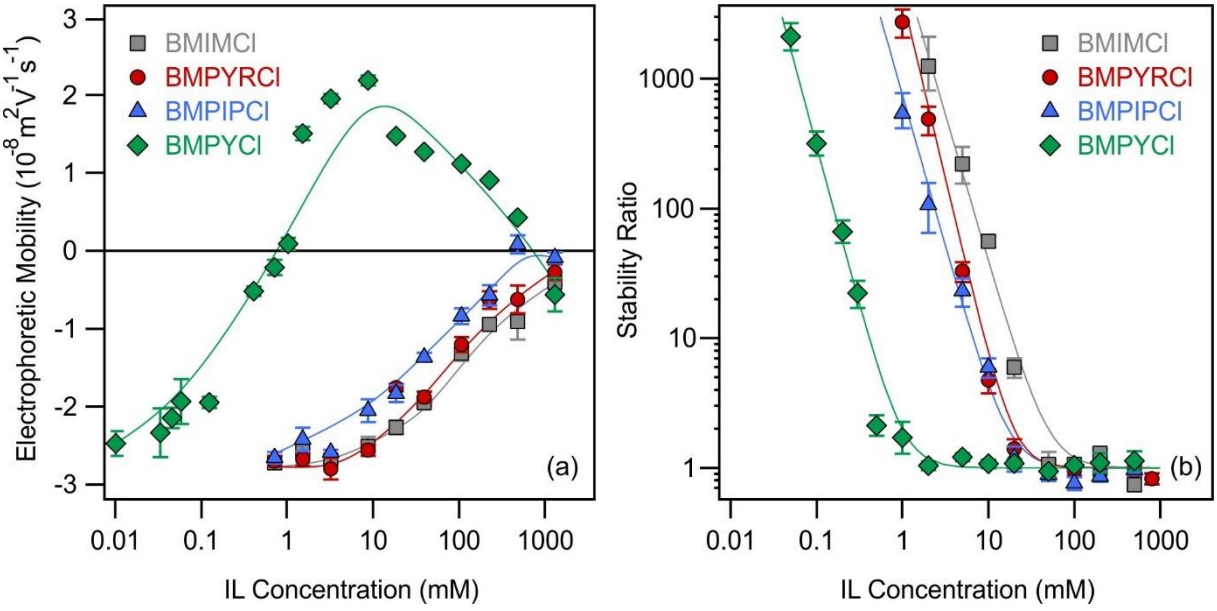

Figure 27. Electrophoretic mobility (a) and stability ratio (b) values of negatively charged h-HNTs at different concentrations of ILs with different cationic structures (Reprinted (adapted) with permission from Ref. 292. Copyright (2022) American Chemical Society). The lines in (a) serve to guide the eyes, while the lines in (b) were estimated by equation (29). The measurements were performed at pH 7 and h-HNT concentration was kept constant at 10 mg/L.

Under these experimental conditions, ILs can be thought to be entirely dissociated into hydrated anions and cations.[154,181,300] The findings exhibited that the system containing $BMPY^+$ cation functions somewhat differently than the other systems. As a result, charge neutralization and reversal manifested, demonstrating a pronounced affinity with $BMPY^+$ cation adsorption on the surface of h-HNT. This is unusual for a monovalent counterion, despite the fact that several other IL cations with either hydrophilic[301] or hydrophobic[179] surfaces had similar activity. The mobilities quantified with BMIMCl, BMPYRCl, and BMPIPCl solutions declined with rising IL concentration, and the data retained negative value even at high IL levels. The

magnitude of the zeta potentials when applied the same IL concentration range, followed the sequence of $BMPY^+$ < $BMPIP^+$ < $BMPYR^+$ < $BMIM^+$ (Figure S4). The fact that the methyl group is coupled to the carbon atom in the $BMPY^+$ cation and not to nitrogen as in the other ILs (structures presented in Figure 11), may influence its pronounced affinity to the surface. However, there is no clear experimental confirmation to unambiguously clarify this issue and further studies are needed.

Figure 27b shows the stability ratio data determined for the h-HNT for the same ILs as above. In each case, the general trends in the stability ratios were similar and resembles to those obtained for inorganic salts discussed earlier. When the IL concentration is low, higher stability ratio values are measured; this signifies slow particle aggregation, however, when the IL concentration is increased, after the threshold value (CCC), the stability ratios approach unity and remain constant, indicating rapid particle aggregation. This behavior is consistent with the predictions of the DLVO theory discussed in previous *chapter 5.2*. These findings apply to all systems studied, however, the actual values of the stability ratio change by altering the composition of the ILs. However, this impact of electrolyte type on colloidal stability is not assumed by the DLVO predictions. In the sample with h-HNT-BMPYCl, there was no restabilization by charge reversal, as is the case with the most hydrophobic ions, such as 1-hexyl-3-methylimidazolium and 1-octyl-3-methylimidazolium, which show a more pronounced charge reversal and subsequent restabilization of the sulfate latex particles.[179] In the case of the h-HNT-BMPYCl system, this results from the combined effect of the relatively low magnitude of electrophoretic mobilities and charge screening by the nonadsorbed IL constituents.

5.2.2. Surface charge and aggregation with IL cations of different alkyl chain lengths

The influence of ILs of various alkyl chain lengths derived from imidazolium, such as MIMCl, EMIMCl, BMIMCl, and HMIMCl on the mobilities and stability ratios of h-HNT was investigated. The co-ion (which has the same charge sign as h-HNT) applied in all systems was the same, but the counterion (which has the opposite charge sign of h-HNT) was systematically altered.

Figure 28a shows the electrophoretic mobility values recorded for the h-HNT in the presence of ILs with different alkyl chain lengths. In general, mobility values increase with the concentration of ILs. The particles in the MIM^+, $EMIM^+$, and $BMIM^+$ cases were negatively charged throughout the IL concentration range studied. The increase is mostly caused by the

joint effect of charge screening by ions of IL components and ion adsorption with different affinities to the surface. Accordingly, $BMIM^+$ has the highest affinity to the surface compared to MIM^+ and $EMIM^+$. Additionally, it can be deduced that counterions, like $HMIM^+$, that have longer aliphatic chains exhibit higher surface adsorption which leads to charge reversal. After the intermediate maximum, charge screening causes the electrophoretic mobilities in this system to decrease at higher IL concentrations. The zeta potential values were also interpreted for these IL systems (Figure S5). The calculated surface charge density values for the h-HNTs with MIMCl, EMIMCl, BMIMCl, and HMIMCl, are listed in Table 3. Though, the obvious discrepancy between the estimated and measured zeta potential values for $BMIM^+$ and $HMIM^+$ indicates that the Debye-Hückel model is not appropriate in this situation at higher IL concentrations because of the pronounced adsorption of the counterion on the surface.

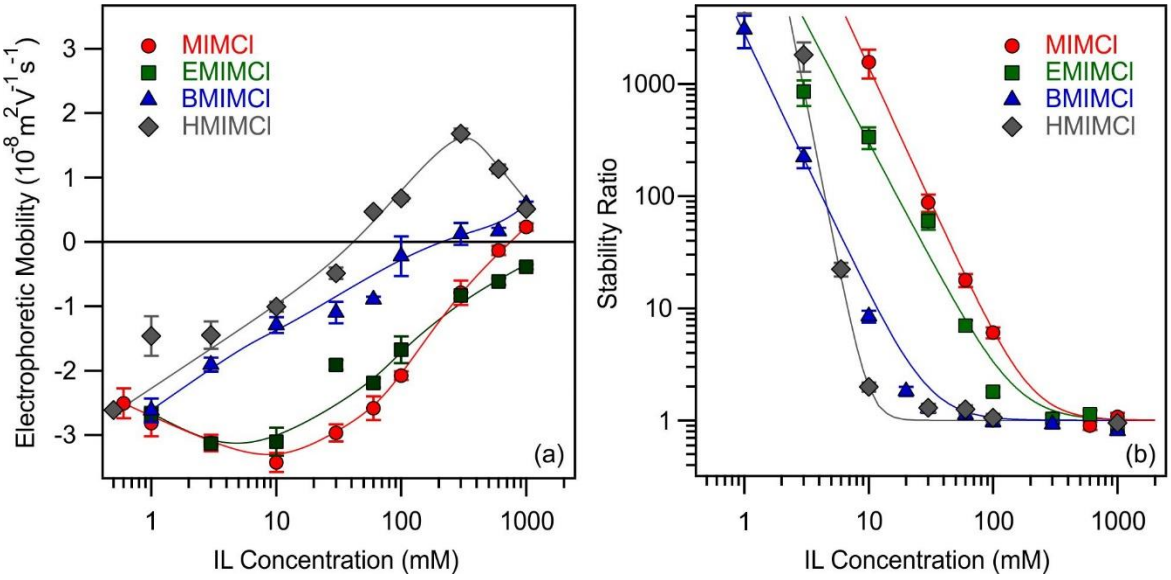

Figure 28. Electrophoretic mobility (a) and stability ratio (b) data of negatively charged h-HNTs with different concentrations of imidazolium-based ILs with different alkyl chain lengths (Reprinted (adapted) with permission from Ref. 296. Copyright (2022) American Chemical Society). The lines in (a) serve to guide the eyes, while the lines in (b) were calculated by equation (29). The measurements were performed at pH 7 and particle concentration was kept constant at 10 mg/L.

Figure 28b shows the stability ratios determined for the h-HNT with MIMCl, EMIMCl, BMIMCl, and HMIMCl. In the IL solutions, the h-HNT particles aggregated similarly and exhibited DLVO-type behavior. Accordingly, at low IL concentrations, slow particle aggregation was observed, while in the range above the CCC, rapid particle aggregation took place. However, in the presence of $HMIM^+$, the slope in the slow aggregation regime was markedly steeper than in other systems, which was expected due to the more pronounced hydrophobicity. This behavior has already been reported in the case of

1-octyl-3-methylimidazolium with the longest alkyl chain adsorbed on the sulfate latex particles[179], or in the case of adsorption of anionic alkyl sulfates and sulfonates on anatase and hematite, which alters the surface and cause the particles to become hydrophobic.[302] Here, also, the $HMIM^+$ cation showed the strongest adsorption, which produces surface properties that differ from those of the other systems where the adsorption of the counterion is less intense. In contrast to the DLVO theory, which assumes that all monovalent salts have the same CCC values regardless of their ion types, the discovered CCC values varied in each case.

5.2.3. Ion specific effects and charge-aggregation relation

The CCC values were derived from the stability ratio plot as a function of the IL concentration. The origin of the interparticle interactions was studied using the relation (eq 34) that allows the calculation of the CCC values from charge densities.

The determined CCCs for the h-HNT particles in the presence of the IL constituents are presented in Figure 29a and Table 3.

Table 3. Characteristic aggregation and charging data of h-HNTs particles measured in IL solutions.

IL cations	MIM^+	$EMIM^+$	$BMIM^+$	$BMPYR^+$	$BMPIP^+$	$HMIM^+$	$BMPY^+$
CCC (mM)[a]	200	150	50	20	17	10	1
σ (mC/m^2)[b]	-18	-15	-8	-6	-5	-2	-1
ζ (mV)[c]	-20	-17	-15	-20	-19	-12	-6

[a]Critical coagulation concentration calculated by equation (29). The average accuracy of the CCC calculation is about 10%. [b]Charge density determined with equation (17). [c]Zeta potential at the CCC. An average error for the electrophoretic measurements is about 10%.

The sequence of the CCC values decreases in the following order:

$$MIM^+ > EMIM^+ > BMIM^+ > BMPYR^+ > BMPIP^+ > HMIM^+ > BMPY^+$$

The highest CCC value was measured in the presence of MIM^+, whereas in the presence of $BMPY^+$ cation, the lowest CCC was obtained (Figure 29a). This effect can be explained by the strong adsorption of the cation to the h-HNT surface, which was accompanied by charge neutralization and reversal (Figure S4).

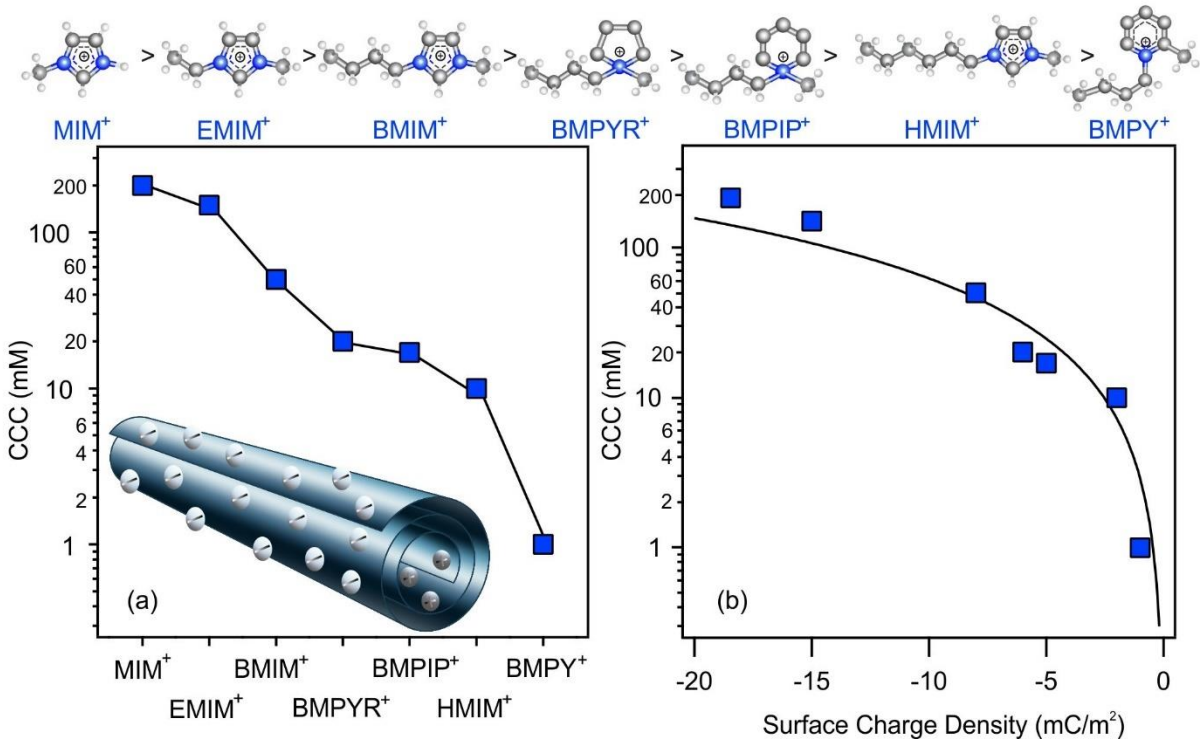

Figure 29. CCC values of h-HNT particles determined in the presence of ILs (a). CCC versus the surface charge density data (b). The experimental CCC and charge density data were calculated with equations (29) and (17), respectively. The lines in (a) are just to guide the eyes, while the line in (b) was estimated by equation (34). The structures of IL cations are presented at the top in order of decreasing CCCs from left to right.

Considering only the imidazolium-based IL cations, the CCC values decrease in the sequence of MIMCl > EMIMCl > BMIMCl > HMIMCl. Such a trend indicates that the length of the alkyl chain modulates the interfacial processes.[303] In fact, on the right-hand side of the sequence, the more hydrophobic cations take place, resulting in lower CCC values, and they adsorb more strongly to the particle surface. In contrast, the more hydrophilic cations are located on the left side of the sequence, owing to the shorter hydrocarbon chains, and they adsorb weaker to the surface, leading to higher CCC values.

The experimental and calculated CCC data in the presence of ILs, exhibited reasonably good agreement once the specific charge densities are implemented in eq 34 (Figure 29b). These observations indicate that aggregation processes, and thus, the origin of the interparticle forces might be derived from the DLVO theory (*subchapter 5.2.3*). However, the position of the CCCs is system specific, and it is defined by the affinity of counterions to the surface, which influences the strength of the EDL repulsion. Ion specific adsorption and the DLVO-type of forces have such a combined influence on the colloidal stability and resulting in the alteration of CCCs.

5.2.4. Extension of Hofmeister series with ILs

Based on the results from the charging and aggregation studies, the direct Hofmeister series was established for the negatively charged h-HNT particles in the presence of simple monovalent inorganic electrolytes and extended with IL cations (Figure 30).

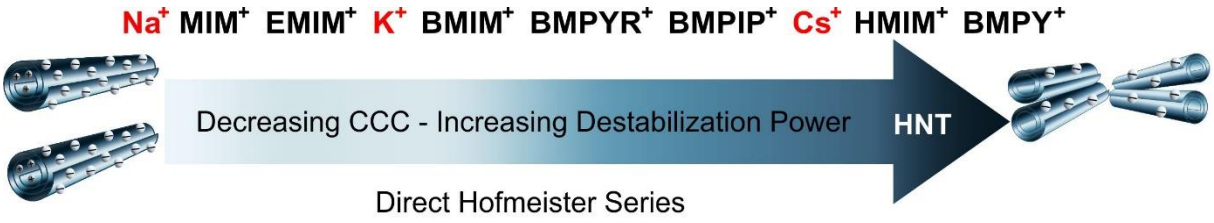

Figure 30. Schematic representation of the direct Hofmeister series established for the negatively charged h-HNTs for inorganic (red) and IL (black) cations.

In the case of $BMPY^+$, the repulsive EDL forces are the weakest owing to the higher extent of charge compensation after the adsorption and thus, the destabilization occurs at low CCC. However, for Na^+, the weak or insignificant adsorption on the oppositely charged surface does not significantly reduce the charge of h-HNT resulting in strong EDL forces. In other words, the remarkable adsorption of the $BMPY^+$ cation results in different charge characteristics and different strength of EDL forces than in the case of Na^+, where the surface charge is comparable to one determined for bare h-HNT particles. The obtained CCCs in the presence of other IL solutions are located between those determined in the presence of salts, which resulted in an extended Hofmeister series for h-HNT particles, where the hydrophobic IL constituents resulted in lower CCCs, while the hydrophilic Na^+ produced the highest CCC. An interesting observation was that higher CCC values were found for MIM^+ and $EMIM^+$ cations compared to the ones obtained in the case of K^+. This behavior may outcome from the ion pair of ILs forming both at the surface and in the bulk. The former situation has already been described[148], and these interactions of the IL constituents in an aqueous solution reduces the ionic strength. As a result, the repulsion between the EDLs becomes stronger, resulting in a higher CCC value. Those adsorbed IL cations, however, have the ability to attract chloride anions from the liquid phase and to create ion pairs on the surface. This outcomes in a weaker charge neutralization and, as a result, a greater negative surface charge, which results in a larger CCC value than in the case of entirely dissociated KCl.

When the cation adsorption is more prominent, as in the case of $BMIM^+$ and $HMIM^+$ cations, the impact of ion pair creation on the surface charge and the related interparticle interactions becomes minor.

5.3. Functionalization of h-HNT particles with polyelectrolytes

The present chapter discusses the functionalization of the h-HNT surface with two different polyelectrolytes through the adsorption process onto the oppositely charged particle surfaces. The charging and aggregation properties were investigated to optimize the experimental conditions for later studies with the polyelectrolyte coated h-HNT. Besides, a powerful masking effect of the IP-2 polymer against ion specific adsorption was revealed during the examination of the colloidal behavior of h-HNT-IP-2 particles in salt and IL solutions.

5.3.1. Interaction of PSP with h-HNT

Due to the occurrence of arginine amino acids that contain positively charged side chain groups, protamine sulfate which is a natural polyelectrolyte, possesses an overall positive charge at physiological pH.[304]

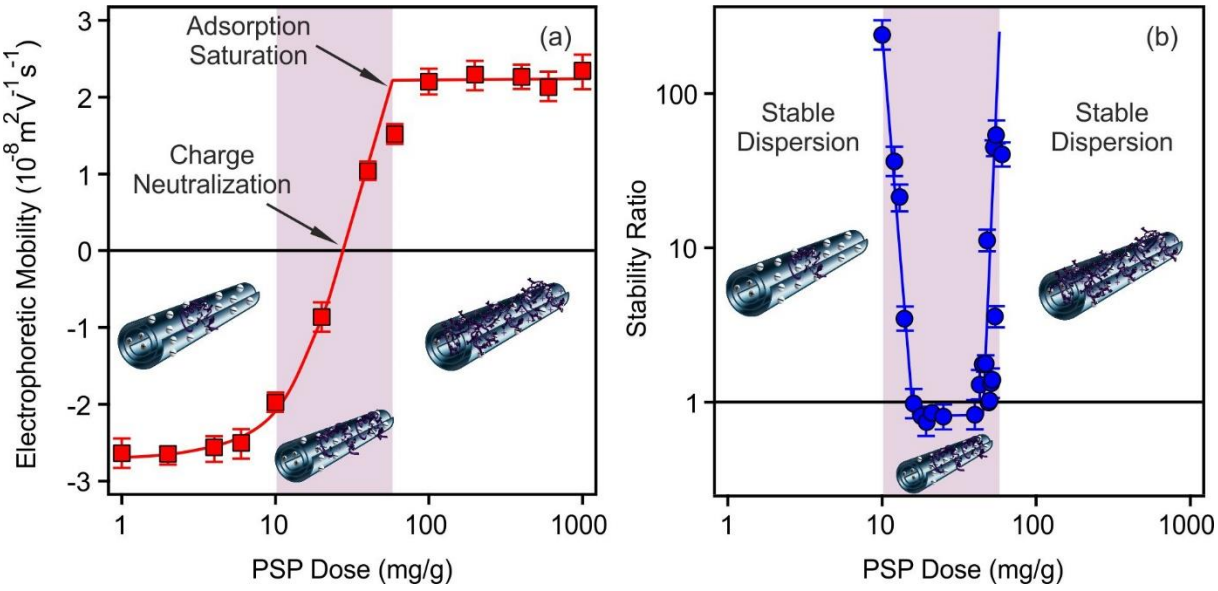

Figure 31. Electrophoretic mobility (a) and stability ratio (b) values of negatively charged h-HNTs at different PSP doses. The measurements were carried out at pH 7, 1 mM ionic strength adjusted by KCl, and at 10 mg/L h-HNT concentration. The mg/g unit on the x-axis refers to mg of PSP per 1 gram of h-HNT. The shaded area represents the PSP dose range corresponding to the aggregation regime. The lines are for eye guidance. Reprinted (adapted) with permission from Ref. 305. Copyright (2022) American Chemical Society.

First, the electrophoretic mobilities of h-HNT at various PSP doses were measured (Figure 31a). The mobilities were negative at low PSP doses (approximately –2.60 ± 0.08 x 10^{-8} $m^2/(V{\cdot}s)$). They increased steeply at PSP doses of more than 10 mg/g, which designates PSP adsorption on the negatively charged h-HNT surface. At the proper PSP doses, the adsorption results in charge neutralization and charge reversal. A constant electrophoretic mobility value

(2.38 ± 0.04 x 10^{-8} $m^2/(V \cdot s)$) occurred above 100 mg/g PSP doses, indicating the formation of a saturated PSP layer. No further adsorption took place with the additional polyelectrolyte doses; instead, they remained dissolved in the bulk solution.

Time-resolved DLS was used to study the aggregation of the PSP-coated h-HNT at different doses of PSP (Figure 32). At low PSP concentrations (e.g., at 10 mg/g), the hydrodynamic radius was constant within the experimental error, but increased somewhat at a dose of 50 mg/g and significantly at 20 mg/g. These three doses, which correlate to the mobility values, are below, above, and at the charge neutralization point. By considering the stability ratios quantified under the identical experimental conditions as in the electrophoretic measurements, the aggregation tendencies were additional evaluated. Data in Figure 31b shed light on that the stability ratios formed a U-shape trend when recorded within the PSP concentration range of 10-60 mg/g, with a minimum near the charge neutralization point. Once stability ratios were near unity at the minimum, the aggregation occurred rapidly, while when the h-HNT surface had a sufficiently high surface charge, the dispersions were stable both before and after the dose that needed to neutralize the surface charge by PSP adsorption. These findings are qualitatively consistent with the predictions of the DLVO theory (*chapter 2.3.*). Accordingly, owing to the lack of surface charge there are no repulsive EDL forces at the point of charge neutralization, and thus, the dispersions become unstable since attractive van der Waals forces predominate.

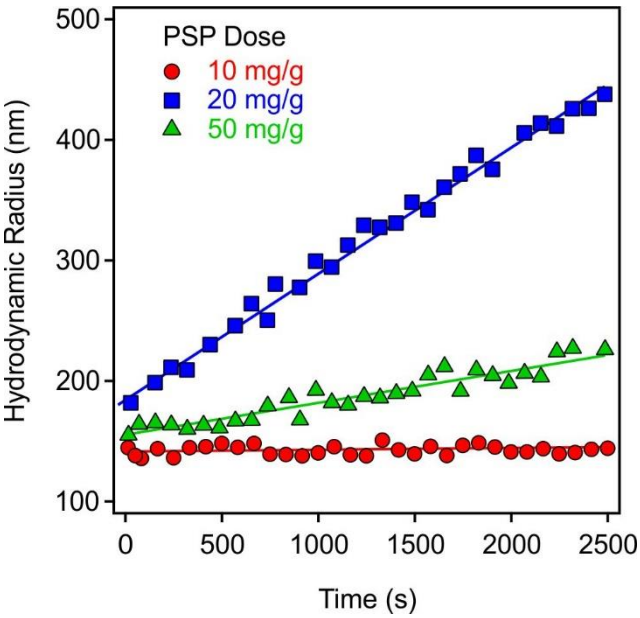

Figure 32. Hydrodynamic radius of the h-HNT particles as a function of time for different PSP doses measured by time-resolved DLS. The experiments were conducted at neutral pH, 1 mM KCl and 10 mg/L h-HNT concentration. The mg/g unit refers to mg of PSP per 1 gram of h-HNT and the lines are linear fits used to calculate the stability ratios with equation 28. Reprinted (adapted) with permission from Ref. 305. Copyright (2022) American Chemical Society.

5.3.2. Surface modification of h-HNT with IP-2

Similar to the previous case, functionalization with a new type of polyelectrolyte (IP-2) was achieved through surface adsorption and subsequent altering of the charge. To determine the proper dose for coating the h-HNT, electrophoretic mobility studies of the h-HNT particles

were performed at different IP-2 doses. The negative mobility values were measured at low polyelectrolyte concentrations, as illustrated in Figure 33.

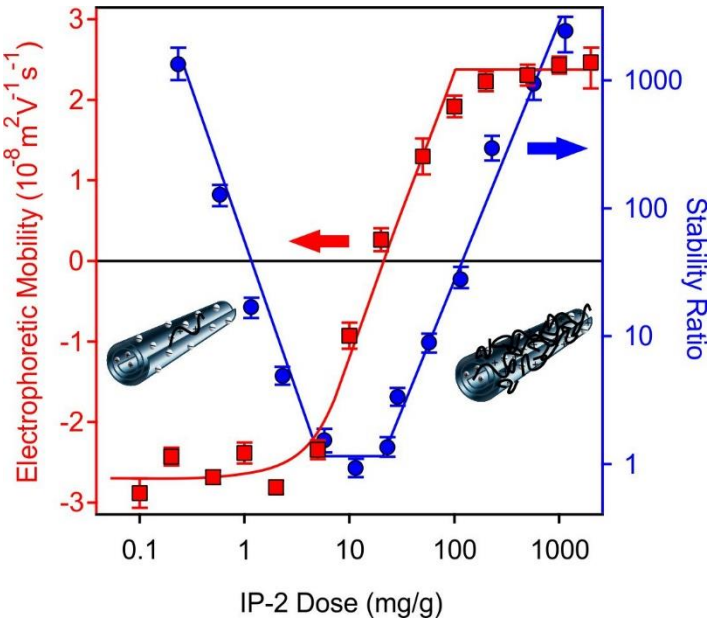

Figure 33. Electrophoretic mobility (red squares, left axis) and stability ratio (blue circles, right axis) values of h-HNT particles versus the IP-2 dose at neutral pH and at 10 mM ionic strength adjusted by KCl. Unit mg/g refers to milligrams of IP-2 per 1 gram of h-HNT. The lines serve to guide eyes. Bare h-HNT (left) and IP-2-coated h-HNT (right) are depicted in two inset pictures. Reprinted (adapted) with permission from Ref. 296. Copyright (2022) American Chemical Society.

The charge neutralization and reversal of the h-HNT particles occurred by increasing the amount of the polyelectrolyte. A saturated IP-2 layer was formed on the h-HNT surface at polyelectrolyte doses greater than 200 mg/g, where mobility values remained constant. At this stage, a relatively high positive surface charge accumulated on the surface of the particles.

The aggregation properties of the h-HNT-IP-2 particles were studied at different doses of IP-2 through following the hydrodynamic radii (Figure 34). At an IP-2 dose of 1 mg/g, the hydrodynamic radius changed slightly due to the partial neutralization of the h-HNT surface by polyelectrolyte and presence of remarkably strong EDL forces, which prevent aggregation. A greater increase was observed at a dose of 25 mg/g, where the particles were positively charged, and the highest increase was observed at an IP-2 dose of 10 mg/g. Compared to mobilities, these doses occur below, above, and at the charge neutralization point, respectively. No aggregation was observed at a dose of 200 mg/g, where electrophoretic measurements signify the creation of a saturated IP-2 layer on the surface.

The stability ratios, determined for the h-HNT in the presence of IP-2, followed a U-shape curve and showed the same behavior as in the case of PSP surface functionalization of h-HNT

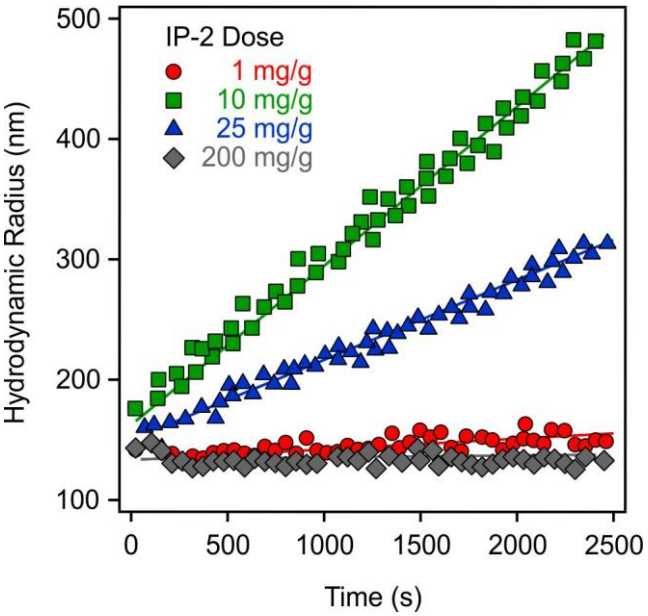

Figure 34. Hydrodynamic radius as a function of time for different doses of IP-2 measured in time-resolved DLS experiments. The measurements were carried out at neutral pH, 10 mM ionic strength adjusted by KCl and at 10 mg/L h-HNT concentration. Unit mg/g refers to milligrams of IP-2 per 1 gram of h-HNT. The lines represent linear fits used to calculate the stability ratios applying equation 28. Reprinted (adapted) with permission from Ref. 296. Copyright (2022) American Chemical Society.

(Figure 33). Specifically, rapid particle aggregation occurred close to the charge neutralization point, and as a result, the stability ratio values rose, showing stable dispersions at low and high doses. Namely, near the charge neutralization point, rapid particle aggregation occurred, while stability ratio values increased before and after this regime indicating stable dispersions at low and high doses. As a result, stable systems were observed at IP-2 doses of 1 and 200 mg/g, while rapid aggregation occurred at a dose of 10 mg/g. The findings agree well with the prediction of the DLVO theory (*chapter 2.3.*). Note that the tendencies in both mobilities and stabilities were similar for the PSP and IP-2 systems, however, the absolute values were system specific, e.g., charge neutralization or surface saturation of h-HNT occurred at different polyelectrolyte doses in these dispersions. Considering the electrophoretic and DLS data, an IP-2 dose of 200 mg/g was selected for later measurements, since at this dose the surface of the h-HNT was entirely covered with IP-2 polyelectrolyte and a stable dispersion was formed.

5.3.3. Effect of surface functionalization on the resistance against salt-induced aggregation

Figure 35 shows the charging and aggregation data of h-HNT-PSP and h-HNT-IP-2 investigated in KCl solutions and compared to the one observed with bare h-HNT particles. Table 4 summarizes the dispersion properties of the above-mentioned particles.

The trends in the magnitude of the mobilities and the stability ratios as the KCl concentration increased were quite comparable to those found for bare h-HNT. The electrophoretic mobility values of h-HNT-PSP and h-HNT-IP-2 decreased with the salt concentration due to charge screening and remained positive except in the case of h-HNT-PSP for the mobility measured at the highest salt level (Figure 35a).

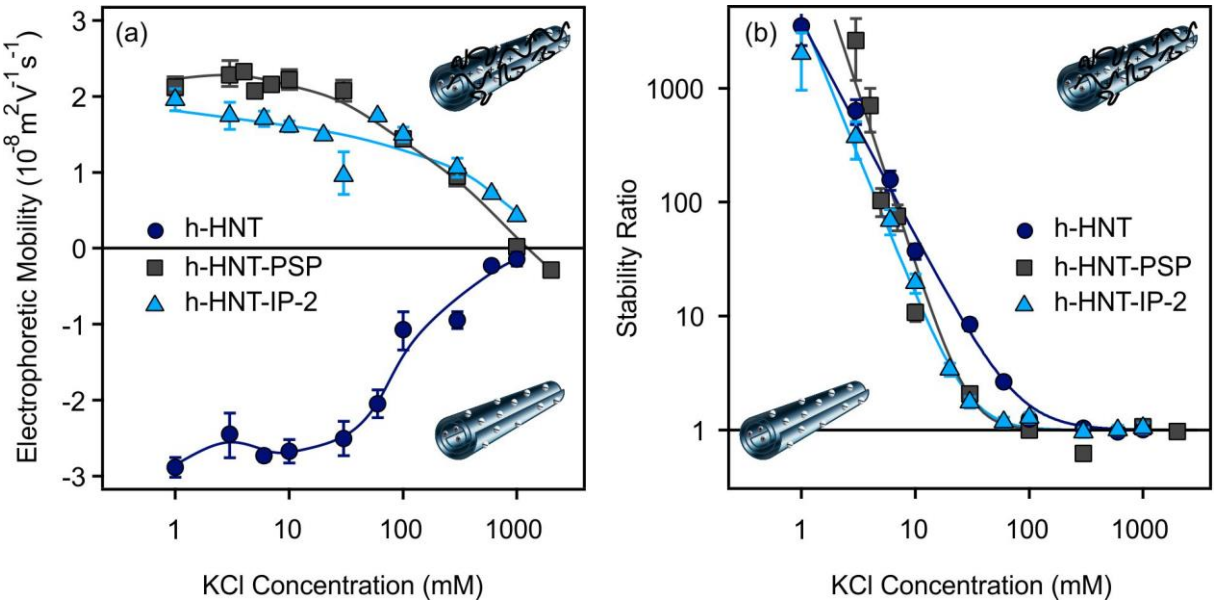

Figure 35. Electrophoretic mobilities (a) and stability ratios (b) of bare h-HNT (dark blue circles), h-HNT-PSP (gray squares), and h-HNT-IP-2 (light blue triangles) at different KCl concentration. The lines in (a) are just to guide the eyes, while the lines in (b) are estimated by equation (29). The measurements were conducted at pH 7 and at 10 mg/L particle concentration. The h-HNT-PSP and h-HNT-IP-2 particles were prepared applying PSP and IP-2 doses of 100 mg/g and 200 mg/g, respectively.

Aggregation properties of bare and functionalized h-HNT were studied within the same KCl concentration range (Figure 35b**)**. The stability ratios were quantified, and slow and fast aggregation regimes were observed, indicating the presence of the DLVO-type forces. The CCC value of the h-HNT-PSP was very similar to the one determined for the h-HNT-IP-2.

Table 4. Characteristic aggregation, size and charging data of the bare h-HNT, h-HNT-PSP and h-HNT-IP-2 nanocarriers.

Compound	R_h[a] (nm)	EM[a] (10^{-8} m^2/Vs)	CCC^b (mM)	PE dose[c] (mg/g)	σ^d (mC/m^2)	PDI[a] (%)
h-HNT	150	-2.88	80	-	-14	19.9
h-HNT-PSP	190	2.12	30	100	10	25.4
h-HNT-IP-2	130	1.96	30	200	14	20.8

[a]Hydrodynamic radius (R_h), electrophoretic mobility (EM), and polydispersity index (PDI) were determined at 1 mM ionic strength. [b]Critical coagulation concentration (CCC) was measured by DLS in KCl solutions and calculated by equation (29). [c]PE dose refers to the polyelectrolyte dose in terms of mg of polyelectrolyte/1 g of particles. [d]Surface charge density was calculated from the ionic strength dependence of the zeta potentials with equation (17). An average error for electrophoretic measurements and for the CCC determination is about 10%.

5.3.4. Particle characterization in solid state

The Raman spectra of h-HNT-PSP and h-HNT-IP-2 were measured and compared with the spectra of bare h-HNT, PSP, and IP-2 polyelectrolytes to prove the functionalization and reveal structural characteristics. The entire set of recorded spectra is displayed in Figure 36, and Table 5 lists the complete assignment of the Raman bands to the functional groups.

Table 5. Assignation of the Raman peaks observed in the spectra of h-HNT-IP and h-HNT-PSP.

Wavenumber (cm^{-1})	Assignment	Compound	Reference
1767	β(OH)		
1645	ν(C=O) (amide I)		
1539	ν_{sym}(aromatic ring)		
1407	ν_{asym}(aromatic ring)	PSP	306
1298	ν(C−N)		
~1100	$\delta_{in\text{-}plane}$ (N−H)		
<1100	δ(aromatic ring)		
1617	ν(C=N)		
~1550	ν_{asym}(aromatic ring)		
~1400	ν_{asym}(hetroaromatic ring)	IP-2	307
~1200	δ_{asym}(aromatic ring)		
~1100	δ_{sym}(hetroaromatic ring)		
909	$\Gamma_{(T')}$(Al–OH)		
708, 750, 792	$\Gamma_{(T)}$(Al–OH)	h-HNT	308
~1200	ν(Si–O–Si)		

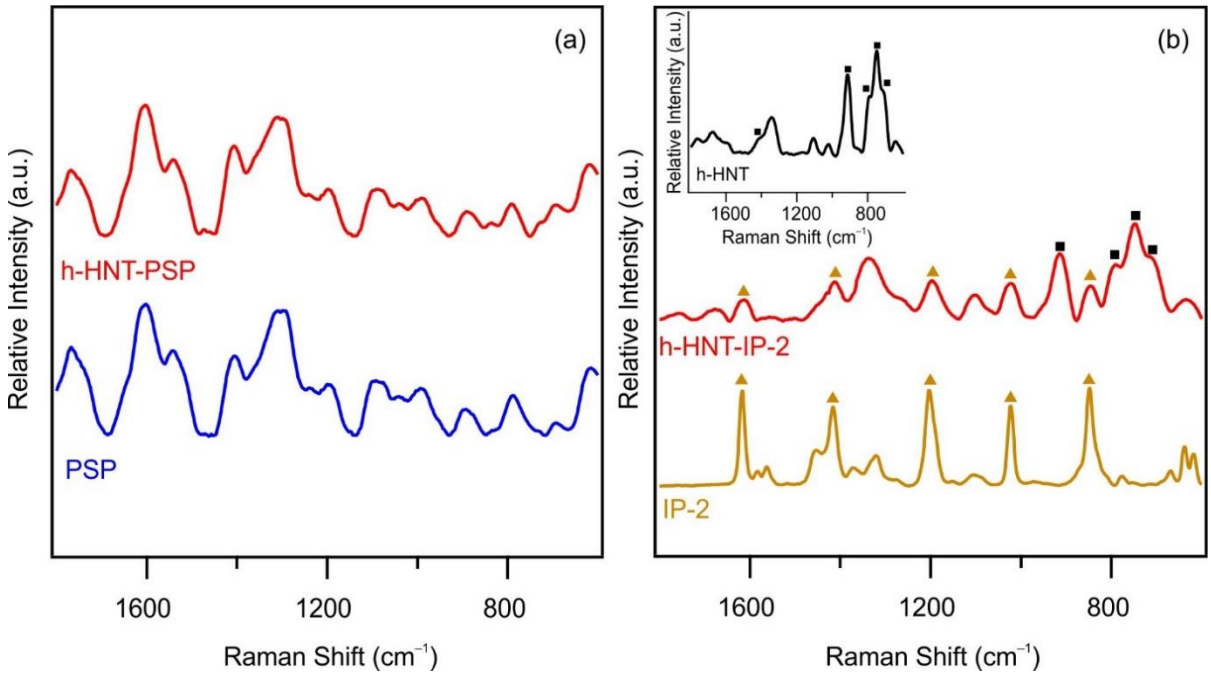

Figure 36. Raman spectra of the PSP, h-HNT-PSP (a), and IP-2, h-HNT-IP-2 (b). The spectrum recorded for bare h-HNT is illustrated in the inset of (b). Characteristic vibrational bands of h-HNT and IP-2 are indicated with squares and triangles, respectively.

Based on the theoretical considerations, only the characteristic Raman bands of the PSP in h-HNT-PSP could be found, as illustrated in Figure 36a. The PSP bands dominate the spectra of the composites since their Raman scattering coefficients are higher than those of the h-HNT. As a result, the amide mode vibrations of PSP were attributed to the strong and relatively broad Raman shifts at about 1406, 1645, 1563, and 1298 cm^{-1}.[306]

In the case of the IP-2 polymer, the Raman bands of the polyelectrolyte and particles were well separated (Figure 36b). There were no comparable Raman masking effects as in the case of PSP since the Raman scattering intensities of the building block species are relatively similar. The spectra illustrated the various stretching modes (between 1600 and 1500 cm^{-1}), deformation bands (from 1200 to 1100 cm^{-1}), aromatic rings of IP-2, and translational mode vibrations of the Al–OH groups of h-HNT. In particular, a single band was found at 909 cm^{-1}, representing the corresponding vibrational mode of the inner Al–OH groups.[309] Aromatic ring deformation bands were recorded at 1023 and 1105 cm^{-1}, and in the 1321 – 1583 cm^{-1} range additional stretching vibrational bands of this organic moiety were observed. The N–C bending vibrations were responsible for one of the strongest peaks at 849 cm^{-1}.[307] At 1617 cm^{-1}, the stretching vibration of the C=N component was also discovered. The presence of the polyelectrolytes and particles in both the h-HNT-PSP and h-HNT-IP-2 composites was confirmed based on peak assignment. At the selected excitation wavelength, the technique was

more sensitive to detect the h-HNT than IP-2 considering their Raman coefficients (Figure 36).[310,311]

TEM measurements were utilized to follow how the shape of the nanoparticles might alter in response to surface modification (Figure 37).

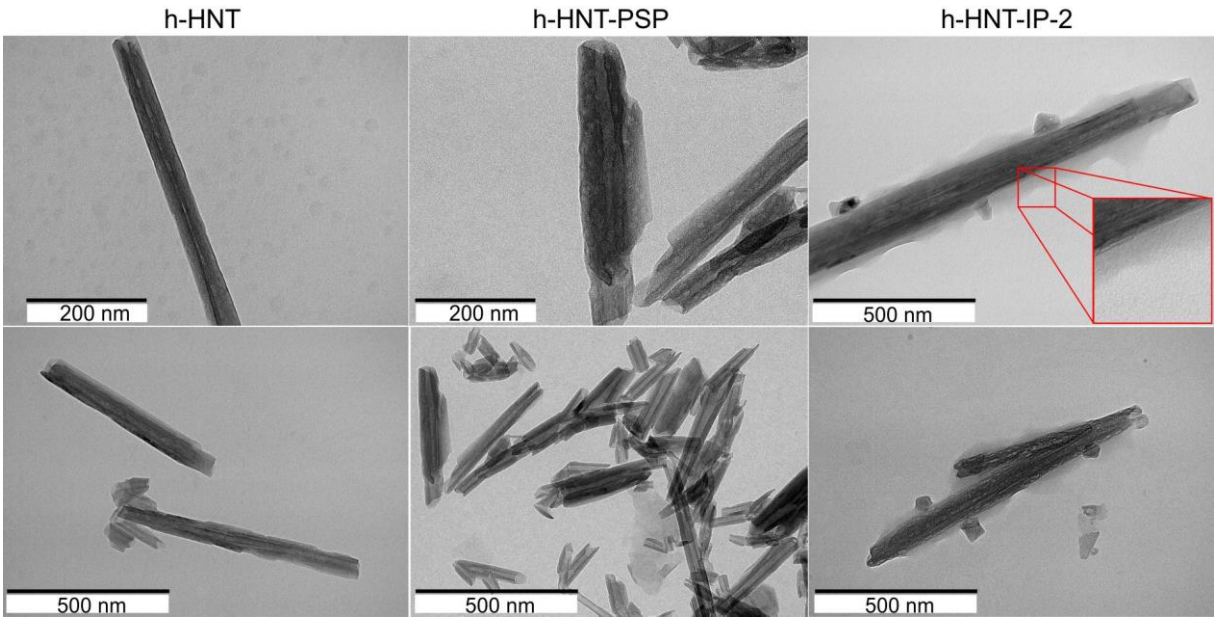

Figure 37. TEM images of bare h-HNT (left column), h-HNT-PSP (middle column), and h-HNT-IP-2 (right column) materials. Images were recorded after drying 10 mg/L dispersion on a copper–carbon mesh.

Since the micrographs were recorded after the sample dried, aggregates of the nanotubes were evident. However, bare and surface-functionalized nanotubes can be distinguished based on their usual morphological characteristics. The tubular shape of the modified h-HNT-PSP and h-HNT-IP-2 particles, as well as bare h-HNT, can be clearly distinguished in the images. The elongated shape of the particles was validated in all cases, which signifies that the adsorption of polyelectrolytes did not affect the morphology of the nanotubes. In surface-modified h-HNTs (h-HNT-PSP and h-HNT-IP-2), the particles are surrounded by a thin shadow-like layer, which may represent the adsorbed PSP or IP-2 layer on the h-HNT surface.

5.3.5. Masking ion specific effects by IP-2 coating

As discussed before in *chapters 5.1 and 5.2*, colloidal stability of h-HNT depended strongly on the composition or structure of salts and ILs leading to different CCCs in these systems. However, a surprising behavior of the IP-2 polyelectrolyte was observed during charging and aggregation measurements performed for h-HNT-IP-2 particles in the presence of

multivalent cations and IL constituents. Figure 38 shows the results of electrophoretic mobility and aggregation measurements of the IP-2-coated h-HNT particles in the presence of monovalent (KCl) and multivalent ($MgCl_2$ and $LaCl_3$) salts.

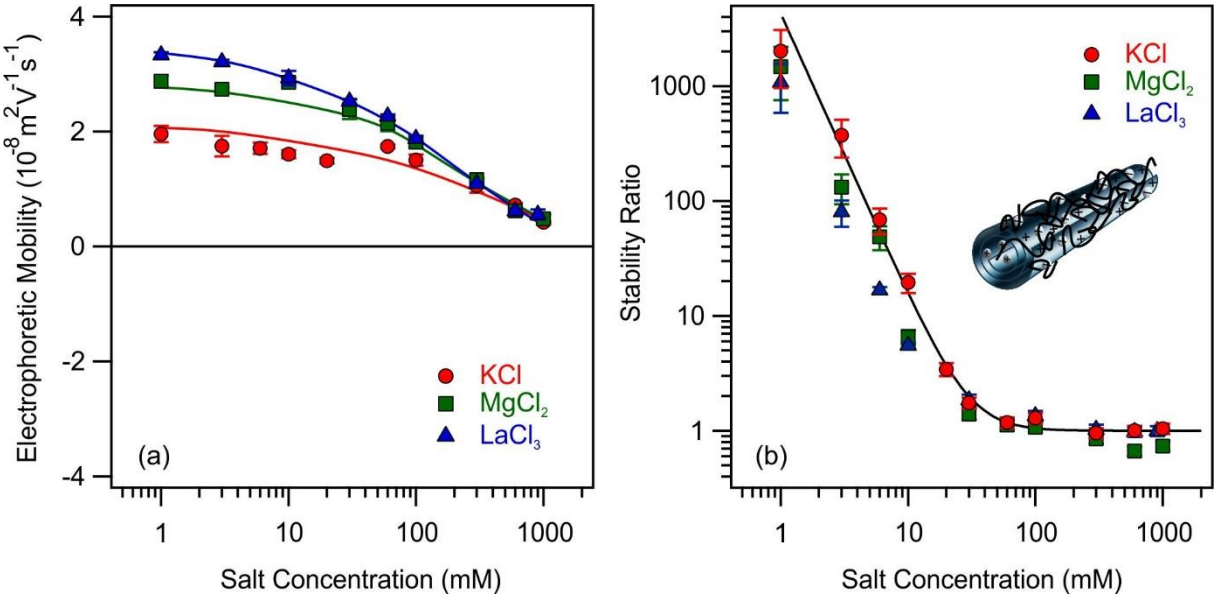

Figure 38. Electrophoretic mobility (a) and stability ratio (b) data of the h-HNT-IP-2 in the presence of multivalent salts at different concentrations (Reprinted (adapted) with permission from Ref. 296. Copyright (2022) American Chemical Society). The lines in (a) are just to guide the eyes, while the line in (b) was estimated by equation (29). The schematic representation of IP-2-coated h-HNT is illustrated in the inset of (b).

The IP-2-coated h-HNT particles interact with the monovalent (K^+) and multivalent (Mg^{2+} and La^{3+}) ions which function as co-ions as they have the identical charge sign as the surface. As one can see, there were variations at lower salt concentrations, but above 30 mM concentration while the mobilities remained constant (Figure 38a). In addition, zeta potentials were quantified (Figure S6) and the results illustrated that after an intermediate small maximum triggered by the electrokinetic effect,[297] they declined and remained positive throughout the range of salt concentrations studied. The estimated charge densities were the identical within the experimental error with a value of +14 mC/m^2, regardless of the type of metal salt. This fact also shed light on that there was no specific adsorption of the co-ions. The findings indicate that the adsorption of inorganic constituents on the h-HNT-IP-2 surface is insignificant and that electrostatic screening of the surface charge leads to a reduction in mobilities with increasing ionic strength.

Figure 38b demonstrates that the quantified stability ratio values for the h-HNT-IP-2 particles were the same for KCl, $MgCl_2$, and $LaCl_3$. As a result, a single CCC value was found for all systems at a salt concentration of about 30 ± 5 mM. In general, the inverse

Schulze–Hardy rule[121,125] states that the valence of the co-ions will affect the CCC value. In addition, the inverse Schulze–Hardy rule states that when multivalent ions are the co-ions, the CCC dependence on co-ion valence is not as considerable (n = 1 in eq 8, *subchapter 2.4.1.*)[123,124,125] as in the case of oppositely charged multivalent ions. Although weaker, this dependence on valence is typical in the case of multivalent co-ions. For example, in the study conducted for boron nitride nanospheres in the presence of ions of different compositions and valences, although the co-ions did not have as strong an effect on the CCC by changing their valence as the counterions did, weak dependence was still evident in line with the inverse Schulze–Hardy rule.[120] Similar behavior was reported in the case of negatively charged sulfate latex and positively charged amidine latex particles in the presence of multivalent co-ions where the decrease in the CCCs by increasing the valence of co-ions was observed for both types of particles.[121,312] Nevertheless, in this case, there is no evidence for a decrease in the CCC values by increasing the valence of the co-ions.

The charging and aggregation properties of h-HNT-IP-2 particles were assessed in the presence of aqueous solutions of imidazolium-based ILs with different alkyl chain lengths (MIMCl, EMIMCl, BMIMCl, and HMIMCl) at various concentrations (Figure 39).

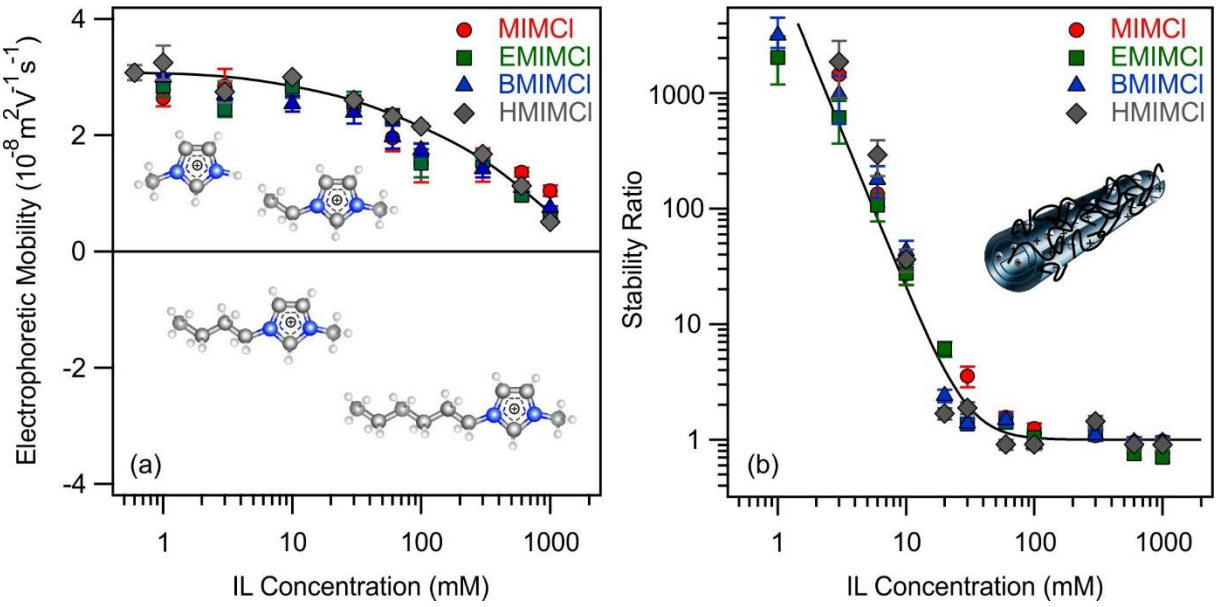

Figure 39. Electrophoretic mobility (a) and stability ratio (b) values of the h-HNT-IP-2 in the presence of imidazolium-based ILs with different alkyl chain lengths at various concentrations (Reprinted (adapted) with permission from Ref. 296. Copyright (2022) American Chemical Society). The line in (a) is just to guide the eyes, while the line in (b) is estimated by equation (29). Structures of IL cations are illustrated in the inset of (a), and a sketch of IP-2-coated h-HNT is shown in the inset of (b).

IL cations serve as co-ions on the surface of h-HNT-IP-2. Figure 39a shows that, like the above results with salt solutions, the addition of different IL co-ions results in the same

electrophoretic mobilities within the experimental error. In addition, mobilities decreased for all systems as concentrations of IL increased, after reaching an initial maximum.[297] If compare the mobilities measured at low IL concentrations, they are slightly higher than in the case of KCl, which indicates some IL cation adsorption. However, the surface charge density calculated based on the measured zeta potentials (Figure S7) was the same for all systems within the experimental error +14 mC/m^2, as in the case of metal salts. Regarding the aggregation characteristics, no changes were observed in the colloidal behavior of h-HNT-IP-2 particles in the presence of IL constituents (Figure 39b). All systems had the identical CCC (30 mM) value since the quantified stability ratios exhibited the same trend. Slightly higher mobility values measured at low IL concentrations do not affect the CCC, which occurs at higher concentrations, indicating that ILs destabilize the h-HNT-IP-2 by charge screening.

These results indicate a strong masking ability of the IP-2 polymer used to functionalize the h-HNT surface, or, in other words, the IP-2 coating produced surfaces indifferent to co-ion specific effects. The results support the previous findings that the saturated IP-2 layer masks ion specific effects and that the only factor affecting the colloidal stability of h-HNT-IP-2 is the ionic strength utilized in the dispersions.[313]

5.4. Immobilization of SOD enzyme and SOD-mimicking metal complex

This chapter discusses the preparation of stable nanocomposite colloids using the h-HNT as solid support and self-assembling biomacromolecules such as PSP polyelectrolyte and SOD enzyme. The SOD enzyme was immobilized on the h-HNT-PSP surface, whose preparation was described in the above chapter. In addition, the interaction between Cu(Cit) complexes, potential SOD mimicking substance, with possible nanotubular supports such as h-HNT, h-HNT-PSP, and h-HNT-IP-2 was investigated. An extensive characterization of the generated nanocomposites in terms of basic colloidal and structural properties was carried out by light scattering methods and spectroscopy, while superoxide scavenging activity was examined in an enzymatic test reaction.

5.4.1. Adsorption of SOD onto h-HNT-PSP

The h-HNT-PSP-SOD bionanocomposite was prepared by adsorption of SOD on h-HNT-PSP using a SOD dose of 10 mg/g, based on former experience with the immobilization of this enzyme on polyelectrolyte-modified particles.[260, 261] Accordingly, the prepared h-HNT-PSP-SOD nanotubes contained 100 mg PSP and 10 mg SOD per 1 g h-HNT. The preparation of the samples and the ivestigations were performed at neutral pH, and under these

conditions, the SOD enzyme is negatively charged since it has an isoelectric point of 4.95.[314] The enzyme was assumed to adsorb to the oppositely charged h-HNT-PSP surface.

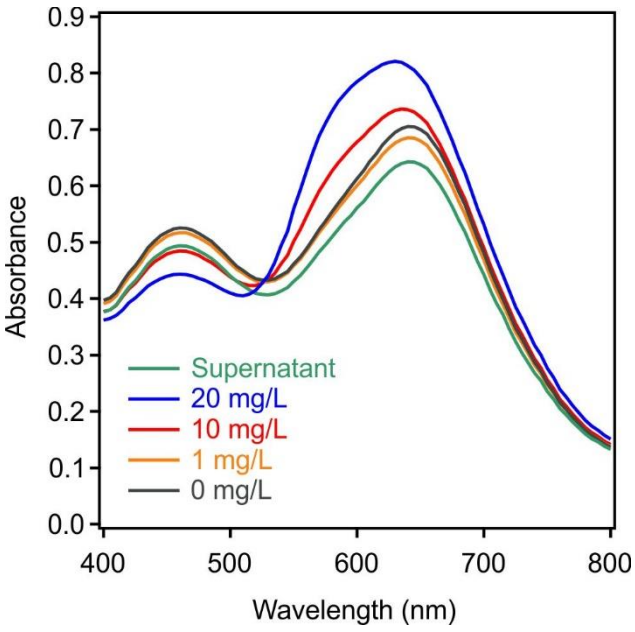

Figure 40. Bradford assays for standard solutions of SOD at 1 mg/L, 10 mg/L, and 20 mg/L concentrations and for the reference system without enzyme (0 mg/L), and for the solution phase after the SOD adsorption procedure (supernatant). Reprinted (adapted) with permission from Ref. 305. Copyright (2022) American Chemical Society

The Bradford test[288] (*subchapter 4.2.9.*) was utilized to estimate the adsorption procedure and to determine the SOD concentration in the solution after removing the h-HNT-PSP-SOD particles by centrifugation. After this removal step, if SOD partitioning occurs between the solution and the particle surface, the applied test should exhibit it. This test can be performed to examine possible leakage of the enzyme too. Figure 40 shows the results along with four reference systems that were prepared with SOD solutions at different doses. It is possible to observe that at higher enzyme concentrations the absorbance values at 465 nm decrease and those at 595 nm rise. Further assessments of the spectra elucidated that the spectrum of the supernatant recorded after adsorption of SOD on PSP-coated h-HNT was comparable to one of the reference samples without SOD molecules. Thus, at an enzyme dose of 10 mg/g, the result clearly demonstrates that the enzyme was quantitatively adsorbed on PSP-modified h-HNTs, and that there was no partitioning between the bulk and the surface. The absence of SOD after the removal of the h-HNT-PSP-SOD hybrid from the dispersions indicates that an insignificant amount of the enzyme leaked from the composite. It is assumed that electrostatic interactions, hydrophobic forces, and hydrogen bonding might be the reason of the significant attractive forces between the enzyme and the carrier.[260,261]

The adsorption of the enzyme on the h-HNT-PSP was proved by recording the FT-IR spectrum of the h-HNT-PSP-SOD composite and comparing it with the spectra obtained for bare h-HNT and PSP-coated h-HNT (Figure 41). In the FT-IR spectrum of bare h-HNT, two distinctive Al–OH stretching bands were discernible at 3702 and 3615 cm^{-1}.[315] The stretching vibration mode of apical Si–O is related to the strong peak at 1089 cm^{-1}, and the band at

1021 cm^{-1} is ascribed to the stretching vibration of Si–O–Si.[51] Moreover, the intense peak at 900 cm^{-1} can be assigned to a single Al–OH bending vibration.[316] In addition, the attendance of PSP is indicated by the absorption bands at approximately 1677 and 1541 cm^{-1} associated with the shifted amide I and II vibrations in the spectra of the PSP-modified h-HNT and h-HNT-PSP-SOD composite.[317] The peak at 1035 cm^{-1} recorded for the developed nanocomposite is related to the shifted C–O stretching vibration of the histidine unit of the SOD enzyme.[268] A significant interaction between h-HNT, PSP, and SOD is apparent from the observed shifts.

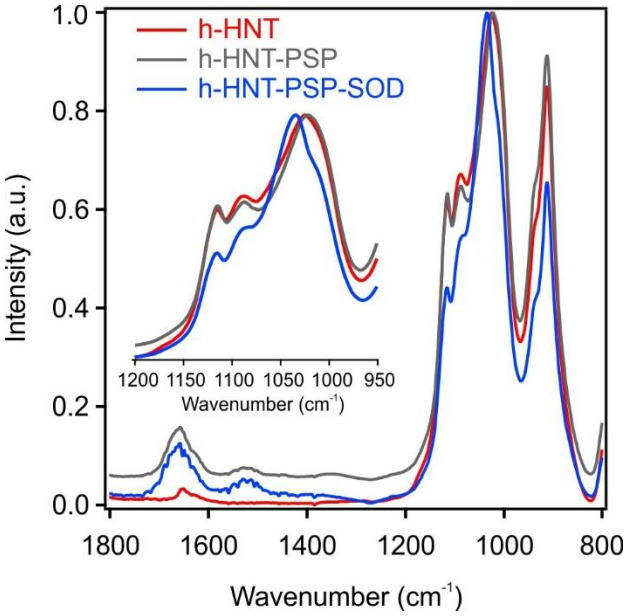

Figure 41. Diffuse reflectance FT-IR spectra of bare h-HNT (red), h-HNT-PSP (grey), and h-HNT-PSP-SOD (blue) in the solid state. Reprinted (adapted) with permission from Ref. 305. Copyright (2022) American Chemical Society.

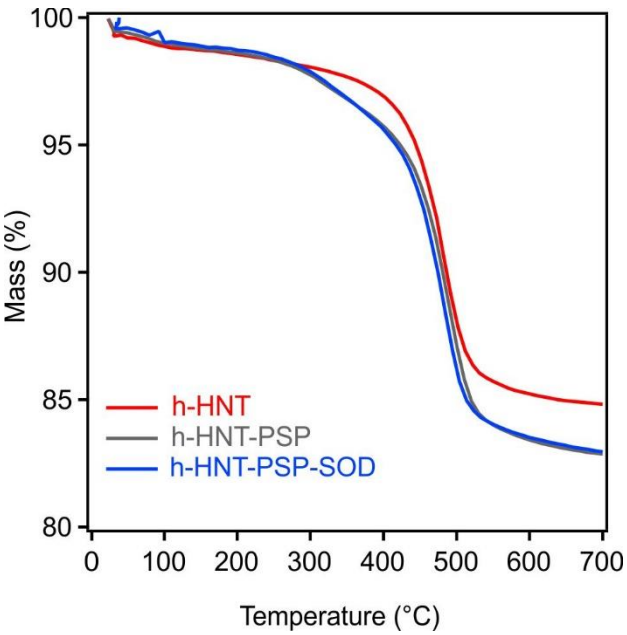

Figure 42. TGA analyses show the mass decrease of h-HNT (red), h-HNT-PSP (grey), and h-HNT-PSP-SOD (blue) materials versus temperature. Reprinted (adapted) with permission from Ref. 305. Copyright (2022) American Chemical Society.

Thermal decomposition of the materials was also investigated by TGA measurements performed on the bare h-HNT, h-HNT-PSP, and h-HNT-PSP-SOD samples (Figure 42). In all samples, the dehydration occurred between 30 and 200 °C, which is common for h-HNT derivatives.[318] Subsequently, the organic molecule was partially degraded between 200 and 400 °C. Thereafter, from 400 to 700 °C, the organic material continued to decompose, and during this time the dehydroxylation of the h-HNT occurred.[319] Due to the low concentration (10 mg/g) of the enzyme in the obtained composite, the TGA curves for h-HNT-PSP and h-HNT-PSP-SOD were identical within experimental error. Nevertheless, the

thermal degradation of h-HNT h-HNT-PSP differed significantly, indicating the presence of PSP macromolecules on the h-HNT surface.

Utilizing TEM and SEM techniques the potential alterations of the nanoparticle morphology were evaluated. From the SEM micrographs, the tubular shape of the h-HNT and h-HNT-PSP-SOD particles can be adequately observed (Figure S8). TEM images illustrated that the outside diameter of the particles was found to be between 50 and 60 nm, and that their usual length was from 200 to 500 nm (Figure 43). Immobilization of the SOD enzyme on the polyelectrolyte-modified particles did not affect the tubular properties of the carrier.

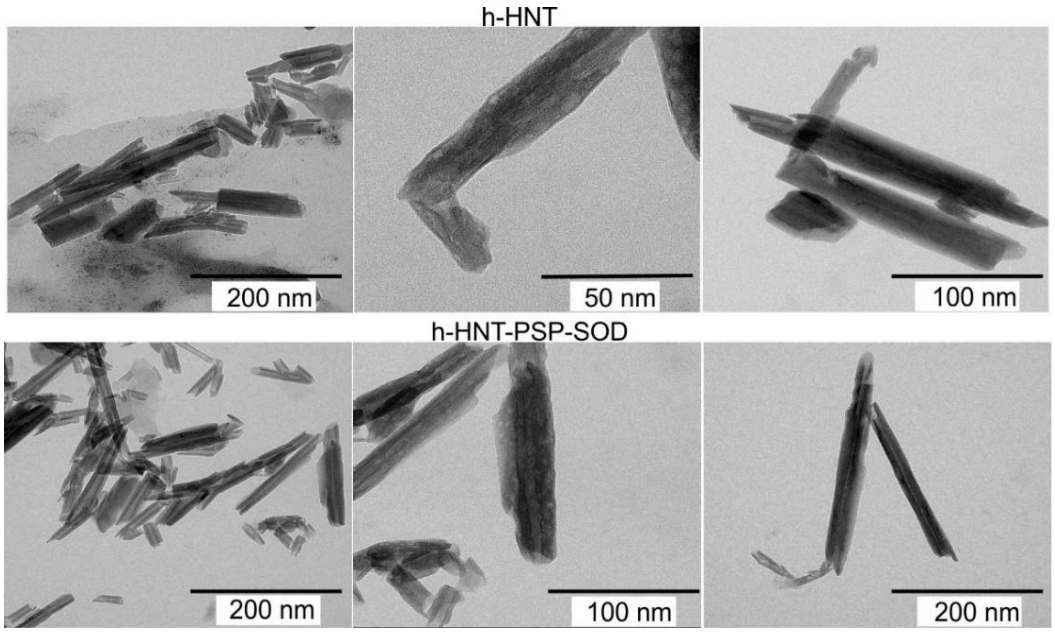

Figure 43. TEM micrographs of bare h-HNT (top row) and h-HNT-PSP-SOD (bottom row) materials. The images were recorded after drying dispersions of 10 mg/L concentration.

The effect of adsorption of SOD on the electrophoretic mobility values and stability ratios was also studied to estimate the charging and aggregation properties of the h-HNT-PSP-SOD containing a dose of 10 mg/g enzyme. SOD concentrations up to 30 mg/g were used to determine the electrophoretic mobilities and hydrodynamic radius values of the h-HNT-PSP.

As shown in Figure 44, the electrophoretic mobilities (2.3 ± 0.08 x 10^{-8} m^2 /(V·s)) were very similar to the value obtained for h-HNT-PSP (2.3 ± 0.06 x 10^{-8} m^2/ (V·s)) within experimental error, indicating that enzyme adsorption did not affect the surface charge of the h-HNT-PSP composite. Moreover, no particle aggregation was noticed within the utilized enzyme dose range under the same experimental conditions, and the measured hydrodynamic radii were found to be approximately 182 ± 9 nm. Despite the addition of SOD, the remarkable colloidal stability of the h-HNT-PSP was maintained.

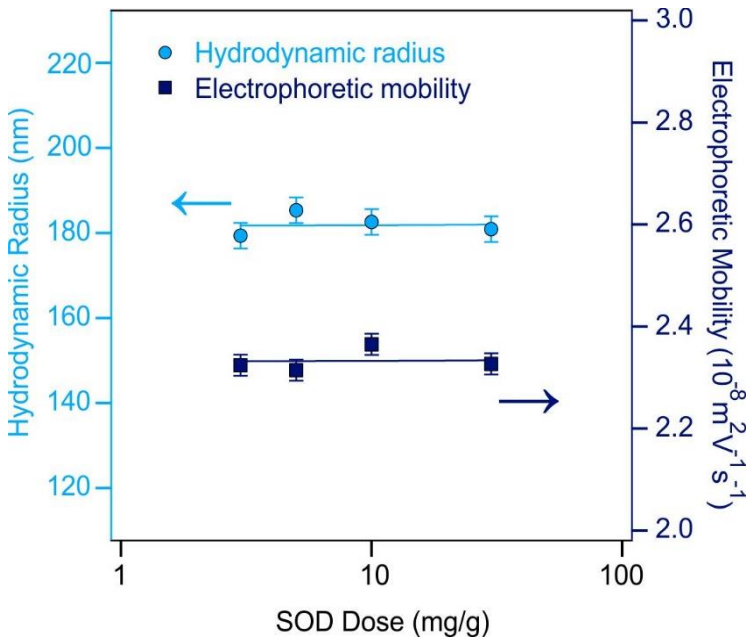

Figure 44. Electrophoretic mobility and hydrodynamic radius data of h-HNT-PSP as a function of different SOD doses. The experiments were conducted at 10 mg/L particle concentration and 1 mM ionic strength. Reprinted (adapted) with permission from Ref. 305. Copyright (2022) American Chemical Society.

5.4.2. Enzyme-like activity of developed nanocomposite

An enzymatic assay[289] (*chapter 4.3.*) was applied to determine whether immobilized SOD enzymes are able to dismutate the superoxides as effectively as native SOD enzymes. Figure 45 illustrates the quantified values for the inhibition of the superoxide radical-NBT reaction in relation to SOD concentration.

The observed inhibition curves for native SOD and h-HNT-PSP-SOD revealed similar shapes, indicating that the enzyme maintained its functional integrity after immobilization on the PSP-modified h-HNT. In both systems, total inhibition (100%) was accomplished. The IC_{50} for h-HNT-PSP-SOD was determined to be lower (0.02 mg/L) than for the native SOD (0.04 mg/L). This rise in SOD activity is most likely caused by the electrostatic interactions between the substrate and the generated nanocomposite. The negatively charged superoxides are attracted by oppositely charged protamine chains adsorbed on the h-HNT surface, and thus, they are more accessible to the entrapped SOD. The aforementioned results are somewhat surprising, as enzyme immobilization frequently results in a significant decrease in enzyme activity.[260] The intrinsic loss of activity caused by deactivation must be distinguished from the apparent loss of activity caused by the inaccessibility of some immobilized enzyme molecules. For instance, the cross-linking type of immobilization using higher enzyme loadings may result in reduced activity, due to the non-catalytic ballast formed. In addition, some enzyme molecules

have limited accessibility when there are multiple layers on the surface of the carrier or located deeply within the carrier pores, where they are inaccessible to the substrate.[320] Increasing the particle size might cause activity loss due to diffusion restrictions, or limited diffusion of the substrate through the large particles.[245] However, in this case, the developed h-HNT-PSP-SOD system proved to be a viable antioxidant option due to its high scavenging activity.

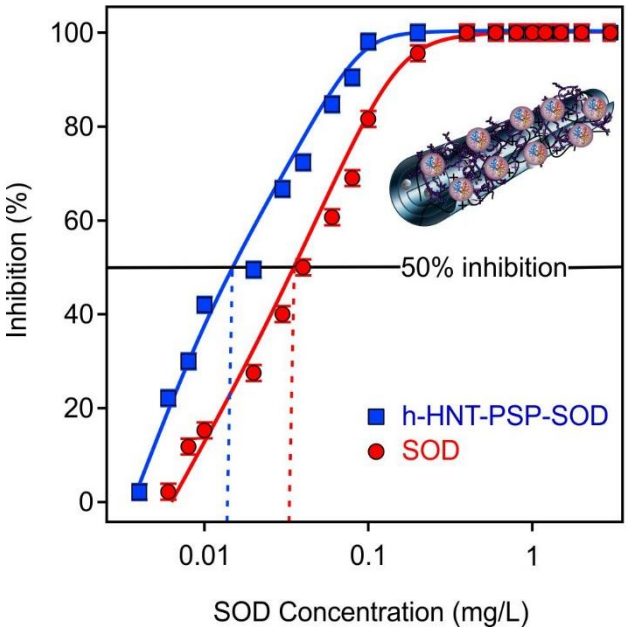

Figure 45. Inhibition of the reaction between NBT and superoxide radicals by SOD (red circles) and h-HNT-PSP-SOD (blue squares). The IC_{50} values are estimated utilizing fits represented by solid lines. The average measurement error of inhibition data is about 5%. Reprinted (adapted) with permission from Ref. 305. Copyright (2022) American Chemical Society.

The developed h-HNT-PSP-SOD hybrid material is a promising antioxidant candidate owing to its excellent scavenging activity. In addition, the developed system exhibits remarkable colloidal (forms stable dispersions) and structural (no enzyme leakage) stability.

5.4.3. Interaction of SOD-mimicking metal complexes with nanotubular carriers

By mixing copper(II) and citrate salt solutions in the proper ratio at pH 7, copper(II)-citrate complexes are formed with metal-to-ligand ratios of 1:1 and 1:2. Owing to the speciation of the solution, the types of metal ions and citric acid can vary in the coordination geometry and compositions.[321] Cu atoms can be bound via 5 oxygen donors, and the oxygen from hydroxyl group from the citrate can bond metal ions to the Cu atoms as a bridge leading to generated dimers.[322] However, in the current study, speciation in solutions was not aimed to be studied, but adsorption of the complex onto nanotubular supports was the goal.

5.4.3.1. Charging features in the complex-particle systems

First, the electrophoretic mobilities for bare h-HNT, h-HNT-PSP, and h-HNT-IP-2 were investigated at various complex concentrations to examine potential interaction between the particles and complexes of 1:1 and 1:2 metal-to-ligand ratios (Figure 46).

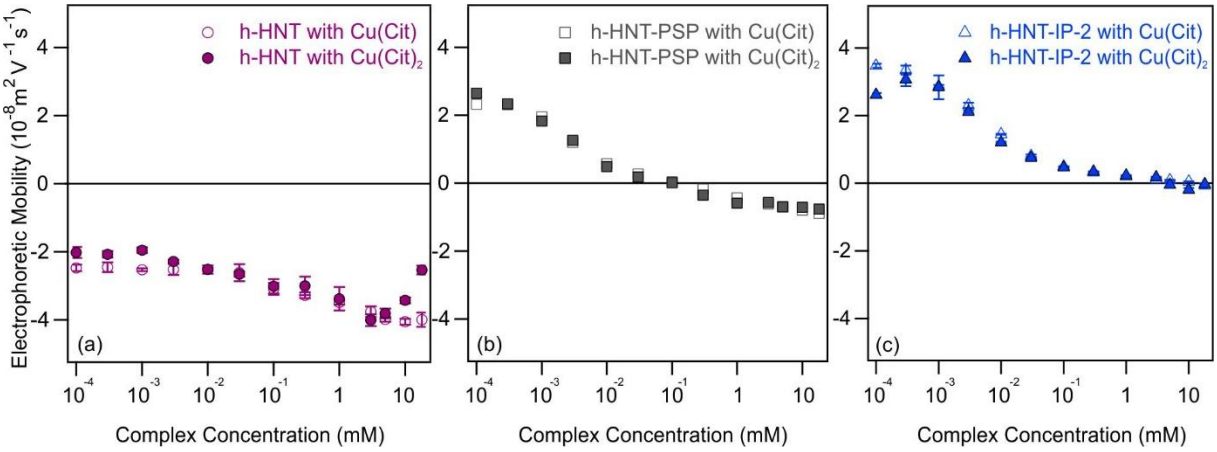

Figure 46. Electrophoretic mobility values of bare h-HNT with Cu(Cit) (empty circles) and $Cu(Cit)_2$ (metal-to-ligand ratio 1:2 was applied, filled circles) (a), for the h-HNT-PSP with Cu(Cit) (empty squares) and $Cu(Cit)_2$ (filled squares) (b), and for the h-HNT-IP-2 with Cu(Cit) (empty triangles) and $Cu(Cit)_2$ (filled triangles). The particle concentration was maintained at 10 mg/L. The PSP and IP-2 doses were kept at 100 mg/g and 200 mg/g in the h-HNT-PSP, and h-HNT-IP-2, respectively. Reprinted from Ref. 323. Copyright (2022), with permission from Elsevier.

The figure shows that no differences in the trend of mobilities were observed for 1:1 or 1:2 stoichiometry ratios. The data reported earlier in the literature were used to identify the structure and composition of the resulting copper(II)-citrate complexes. Namely, for both 1:1 and 1:2 metal-to-ligand stoichiometries, the geometries of the metal complexes are similar. The coordination approaches and corresponding charge of the complexes under these experimental conditions are comparable as previously stated.[321] This may be the consequence of non-bonding interactions or from the distribution of electrons correlating with the preferred orientation for access of electrophiles (metals) and nucleophiles (ligands). It was also found that the 1:1 complex was more stable than the 1:2 complex.[321] The combination of theoretical and experimental research has shown revealed that 1:1 complexes with a structural charge of –1 are the most common species in solutions at neutral pH, even when the ratio of metal-to-ligand is decreased.[324] As a result, in the stock solutions prepared for further research, the copper(II) and citrate ions were combined in equal molar concentrations (expressed as Cu(Cit)).

In the presence of the Cu(Cit) complex in a 1:1 metal-to-ligand ratio (the dominant species ($Cu(Cit)^-$) had a charge of –1), the electrophoretic mobility values measured for the bare

h-HNT, h-HNT-PSP, and h-HNT-IP-2 are shown in Figure 47.

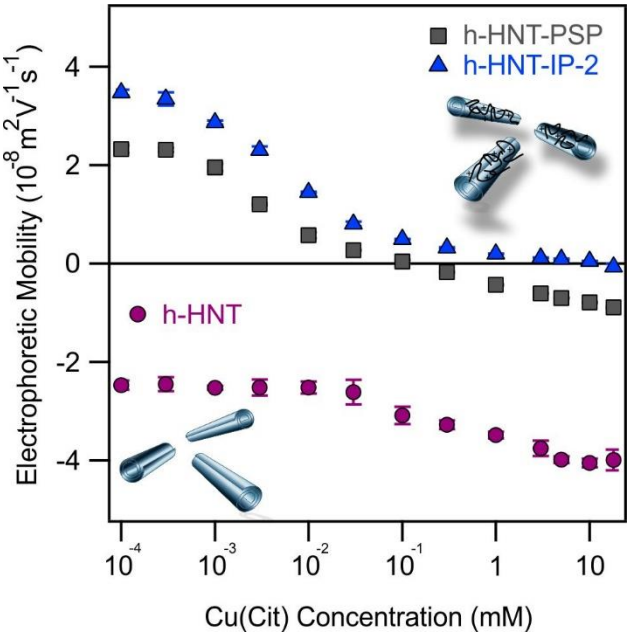

Figure 47. Electrophoretic mobility data of bare h HNT (circles), h-HNT-PSP (squares), and h-HNT-IP-2 (triangles) at different Cu(Cit) concentrations. The particle concentration was kept at 10 mg/L, and the measurements were carried out at pH 7. The PSP and IP-2 doses were maintained at 100 mg/g and 200 mg/g, respectively. Reprinted from Ref. 323. Copyright (2022), with permission from Elsevier.

For the bare h HNT, the electrophoretic mobilities maintained negative values over the whole range of Cu(Cit) concentrations examined. Nevertheless, as the concentration of the complex increased, the mobility decreased, indicating that the complex adsorbs onto the like-charged h-HNT surface. Similar interfacial processes have been described in the past for molecules and surfaces with the same charge sign, although the extent of such adsorption is typically less than for a system with opposite charges.[131,325,326] The complexes may also move in the positively charged inner surface of the h-HNT, but the electrophoretic results are not suitable to determine with certainty how much this internal charge contributes to the overall charge of the material.

Significant complex adsorption was observed with functionalized h-HNTs of positively charged surfaces (h-HNT-PSP and h-HNT-IP-2). The electrophoretic mobilities decreased with the addition of the complex due to its adsorption on the oppositely charged surface. The charge neutralization was recorded in both situations, although it appeared at three orders of magnitude lower complex concentrations on PSP-coated h-HNT than on h-HNT-IP-2 particles. In the h-HNT-PSP system, a slight charge reversal was also observed at high Cu(Cit) concentrations. These results clearly demonstrated that the complex has a greater affinity for the surface of the

h-HNT-PSP. The Cu(Cit) complex and the h-HNT-PSP can interact by non-Coulombic forces since the charge density of the carriers (Table 4, *subchapter 5.3.3.*) indicates the opposite trend, i.e., higher charge was determined for h-HNT-IP-2. Owing to the formation of hydrogen bonds between the Cu(Cit) and the surface functional groups, these interactions result in pronounced adsorption. It has also been shown that different metal complexes and oppositely charged polyelectrolytes interact strongly. In particular, the oppositely charged Cu(II)-histamine complex was successfully immobilized onto poly(vinylpyridine-b-methacrylic acid)-modified LDH particles through dative bonds formed between the donor atoms of the adsorbed copolymer chains and the metal center of the complex.[269] At the appropriate complex concentrations, charge neutralization and reversal occurred due to the strong affinity of the coordination compound to the surface. Additionally, an advanced geometry around metal ion centers was achieved in a hybrid catalytic material composed of LDH particles, two different types of polyelectrolytes PSS and PDADMAC, and metal complexes like Cu(II)-bipyridyl and Fe (III)-citrate.[270]

5.4.3.2. Assessment of size and polydispersity

Hydrodynamic radius measurements were performed to select the proper concentrations of the complexes for further evaluation of the antioxidant activity. In this part of the study, the experimental conditions (e.g., metal complex concentration range), under which potential aggregation processes may occur, were identified in the dispersions. Such aggregates can lead to the formation of unprocessable samples owing to phase separation and a reduction in specific surface area. Figure 48 illustrates the quantified hydrodynamic radii and polydispersity values for all three systems with different Cu(Cit) concentrations.

Data in Figure 48a revealed that the size and PDI values for bare h-HNT did not change over the entire range of complex concentrations examined. A PDI of $23 \pm 2.80\%$ and an average hydrodynamic radius of 153 ± 6 nm were calculated. These values are similar to those found for bare h-HNT in stable dispersions. Since there was no evidence of particle aggregation in the samples, the presence of the Cu(Cit) complex did not affect the colloidal stability of the dispersions. This is in accordance with electrophoretic mobilities measured for bare h-HNTs (Figure 47), which remained negative in the entire regime of the concentration examined, with only a small extent of complex adsorption observed at higher complex concentrations where mobilities decreased.

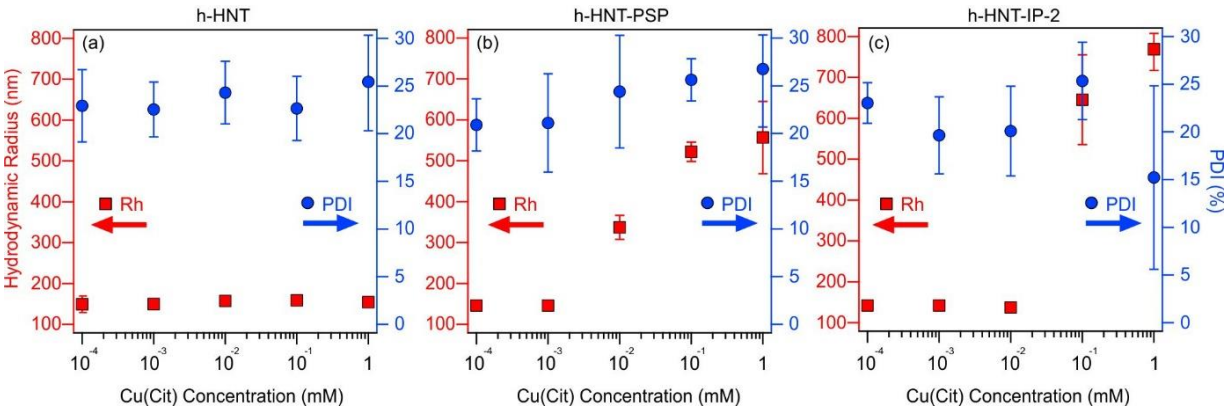

Figure 48. Hydrodynamic radii (red squares, left axes) and PDI (blue circles, right axes) quantified for bare h-HNT (a), h-HNT-PSP (b), and h-HNT-IP-2 (c) as a function of Cu(Cit) concentrations. The particle concentration was kept at 10 mg/L. Reprinted from Ref. 323. Copyright (2022), with permission from Elsevier.

With an increase in the complex concentration, the recorded size data for h-HNT-PSP (Figure 48b) and h-HNT-IP-2 (Figure 48c) increased remarkably, indicating particle aggregation. In line with the mobility data (Figure 47), this process occurred for h-HNT-PSP at a lower complex concentration, since charge neutralization was detected as a result of the Cu(Cit) adsorption on the oppositely charged surface. In this experiment, the attractive dispersion forces prevail because the repulsive interactions between the particles resulting from the overlap of the electrical double layers are eliminated, which causes particle aggregation.[86] Given that charge neutralization occurred in both h-HNT-PSP and h-HNT-IP-2 systems, this situation is associated with an increase in the values of the hydrodynamic radius. However, in the case of h-HNT-PSP, the increase in size was observed at lower complex concentrations which is consistent with charging data which showed that charge neutralization occurs at concentrations almost three orders of magnitude lower than in the case of h-HNT-IP-2, where complex adsorption occurred only as a result of electrostatic attraction.

5.4.3.3. Structural characterization

The coordination geometry of the copper(II)-citrate complexes was investigated by EPR spectroscopy with samples prepared with and without nanoparticles. The EPR spectra of the Cu(Cit) displayed in Figure S9 demonstrate that no appreciable signals from paramagnetic components were found in any system. This illustrates that both the immobilized and non-immobilized complex are in an EPR-inactive dimer form present in all systems. A dimeric structure can be generated by an oxygen from a hydroxyl or carboxylate group which can bridge two Cu(II) ions. A dimeric structure with a 2:2 ($Cu_2(Cit)_2$) composition in the solid phase was also proved by single crystal X-ray diffraction.[322]

Raman spectroscopy measurements were performed to further investigate the adsorption of Cu(Cit) complexes on the surfaces of h-HNT-PSP and h-HNT-IP-2. The Raman spectra of the samples with and without the complex were compared with those of bare h-HNT, h-HNT-PSP, and h-HNT-IP-2 (Figure 49).

The focus was on the samples containing Cu(Cit) complexes, since the characteristic Raman bands of the PSP and IP-2 polyelectrolytes and for h-HNT-PSP and h-HNT-IP-2 particles have already been explained in detail in *subchapter 5.3.4.* For h-HNT-PSP-Cu(Cit) and h-HNT-IP-2-Cu(Cit), new Raman shifts were observed at 1465 and 1326 cm^{-1}, indicated by star symbols (Figure 49).

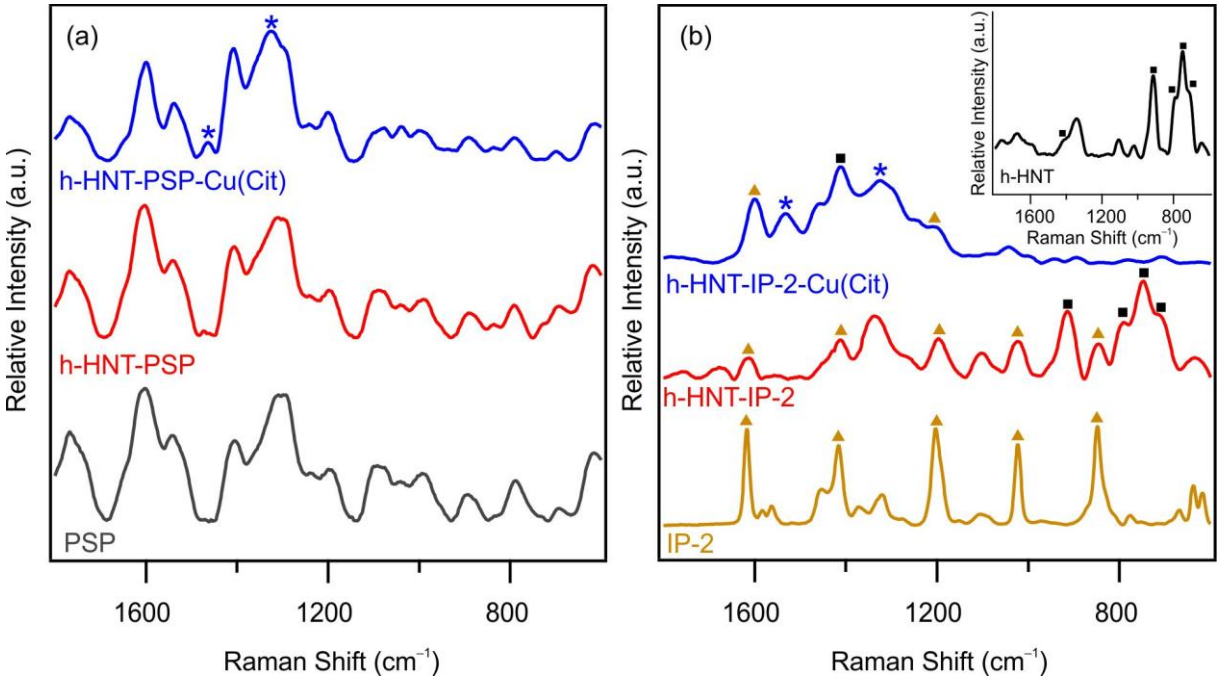

Figure 49. Raman spectra recorded for PSP, h-HNT-PSP, and h-HNT-PSP-Cu(Cit) (a) as well as IP-2, h HNT IP 2, and h-HNT-IP-2-Cu(Cit) systems (b). The spectrum of bare h-HNT is demonstrated in the inset of (b). Characteristic vibrational bands of h-HNT and IP-2 are indicated with squares and triangles, respectively, while Cu(Cit) with star symbols. Reprinted from Ref. 323. Copyright (2022), with permission from Elsevier.

The carboxylate group vibrations of citrate that have been shifted to the lower energy area are responsible for these bands.[327] In general, the carboxylate groups have two characteristic vibrations, an asymmetric (at 1600 cm^{-1}, and symmetric, in the case of citrate salt (at 1390 cm^{-1}).[327] The shift of these peaks confirms the complexation (Cu(Cit)). The existence of these bands suggests both the structural stability of the complex after adsorption and the presence of species in the samples comprising citrate and this is supported by the reduction in carboxylate separation from $\Delta\ (COO^-) = 210\ cm^{-1}$ to $\Delta\ (COO^-) = 139\ cm^{-1}$.[328] The latter value

represents the difference between shifts found at 1465 cm^{-1} and 1326 cm^{-1}, and it is lower than the carboxylate separation when the citrate is in salt form (210 cm^{-1}). This decrease confirms that citrate is found in the complex form as a bidentate ligand. Due to this carboxylate separation, which is characteristic of the complex, it can be concluded that the complex retained its structure upon immobilization.

In the case of the h-HNT-IP-2-Cu(Cit) system (Figure 49b), the carboxylate group vibration of the complexes was detected, but the locations of the bands (at 1533 and 1324 cm^{-1}, respectively) were different from that recorded for PSP systems. This result suggests that when different nanocomposites are used as supports the citrate ligands may adopt various structures or conformations. Although the conformation of the complex was altered, it has been demonstrated that Cu(Cit) complex interacts with both h-HNT-PSP and h-HNT-IP-2 particles.

5.4.4. Superoxide radical scavenging activity

The antioxidant activity of the developed h-HNT-Cu(Cit), h-HNT-PSP-Cu(Cit), and h-HNT-IP-2-Cu(Cit) systems was evaluated. The complex concentrations of 0.1 mmol/g and 10 mmol/g (mmol Cu(Cit) per 1 g of the support corresponding to 1 μM Cu(Cit) and 100 μM Cu(Cit) concentrations, respectively, in Figure 48), were selected to study the antioxidant activity. The same type of assay was conducted as in case of the native enzyme discussed in the previous chapter. The determined inhibition data was plotted as a function of the concentration of Cu(Cit). The IC_{50} values, representing the Cu(Cit) concentration required to capture half of the radicals generated in the test reaction, were utilized to express the activity. Figure 50 shows the inhibition curves, and Table 6 summarizes the IC_{50} values.

It was observed that the results for all systems were quite similar at copper(II)-citrate content of 0.1 mmol/g (Figure 50a) or 10 mmol/g (Figure 50b). The IC_{50} value for the native SOD enzyme was determined to be 0.002 μM, while for the Cu(Cit) complex was 0.400 μM. Although the native enzyme had a lower IC_{50} value, the Cu(Cit) complex still exhibited considerable potential to mimic the function of SOD. Data in Figure 50 shed light on that complete inhibition was achieved in all systems, regardless of Cu(Cit) concentrations or particle aggregation level, which took place at 10 mmol/g Cu(Cit) dose for the particles functionalized with polyelectrolytes. Moreover, immobilization of the complex enhanced its activity, as its IC_{50} was lower for the h-HNT-PSP-Cu(Cit) and h-HNT-IP-2-Cu(Cit) systems than for Cu(Cit) in a homogeneous solution.

Table 6. Activity of the artificial enzymes in dismutation of superoxide radical anions determined in the Fridovich assay.[289]

Carrier	Cu(Cit) content (mmol/g)[a]	IC_{50} (μM)[b]	I_{max} (%)[c]
h-HNT	0.1	0.117±0.003	95.6±0.8
	10	0.211±0.070	96.8±0.6
h-HNT-PSP	0.1	0.109±0.004	97.6±0.3
	10	0.103±0.013	96.1±0.7
h-HNT-IP-2	0.1	0.144±0.005	97.8±0.6
	10	0.126±0.013	98.8±0.7

[a]Cu(Cit) content refers to the complex dose normalized to the mass of particles. [b]IC_{50} values were calculated from the fits on the experimental inhibition data in Figure 50. [c]I_{max} refers to the maximum inhibition reached in the assay.

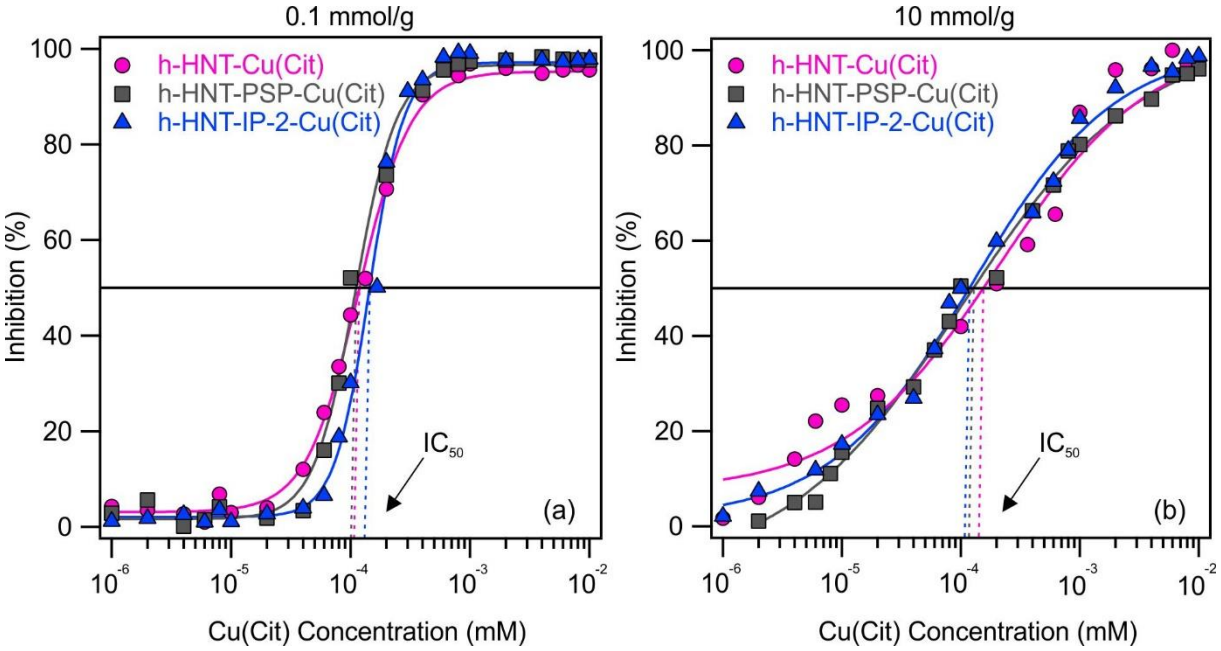

Figure 50. SOD activity for the h-HNT-Cu(Cit) (purple circles), h-HNT-PSP-Cu(Cit) (gray squares), and h-HNT-IP-2-Cu(Cit) (blue triangles) systems at 0.1 mmol/g (a) and 10 mmol/g (b) complex doses (corresponding to 1 μM and 100 μM Cu(Cit) concentrations in Figure 48, respectively). The solid lines present mathematical functions used for the IC_{50} value estimation, while the dashed lines signify the Cu(Cit) concentrations equal to the IC_{50} data. The average error of the measurement is less than 5%. Reprinted from Ref. 323. Copyright (2022), with permission from Elsevier.

When Cu(II) ions are entrapped, electrostatic interactions or hydrogen bonds between ligands and polyelectrolytes adsorbed on the surface appear, and thus can alter the coordination geometry surrounding the Cu(II) ions. This increase in activity could be explained by the

positively charged functional groups in the structures of h-HNT-PSP-Cu(Cit) and h-HNT-IP-2-Cu(Cit). By modifying the surface of the h-HNT particles, the positive charge effect was realized to attract the negatively charged $O_2^{\bullet -}$ to the active copper site. Evidently, the positive charge around the copper active center can increase the reaction rate, facilitating the attraction of the superoxides to the active site. Other particle systems have also shown an improvement in the enzyme-like activities of metal complexes after immobilization.[235] In particular, a nanocomposite with significant antioxidant activity was prepared by successive adsorption of polyelectrolytes such as PSS and PDADMAC and redox active metal complexes (Cu(II)–bipyridyl and Fe(III)–citrate) on the LDH nanoclay that served as support.[270] Another example is when the Cu(II)-diethylenetriamino-μ-imidazolato-Zn(II)-tris-(aminoethyl)amine perchlorate was immobilized on the modified mesoporous silicas and highly SOD active catalytic nanosystem was developed.[329]

These findings revealed that the developed systems exhibit remarkable antioxidant properties and great potential for developing the SOD-mimicking nanoparticle systems that could be less sensitive than native enzymes. To the best of our knowledge, no data were reported on antioxidant composites, in which enzyme-mimicking metal complexes were immobilized in/on h-HNT-based nanocarriers.

In both cases, upon immobilizing SOD (*subchapter 5.4.2.*) and SOD-mimicking Cu(Cit) complex, on the polyelectrolyte-modified h-HNT nanocarriers, an increase in activity was observed. Apparently, the functionalization with positively charged polyelectrolytes had a significant impact. It has been demonstrated that by modifying the surface and providing positively charged surface groups, the catalytic environment of the active center of the immobilized enzyme or enzyme mimic compound can be tuned, and excellent catalytic activity of SOD can be obtained.

6. Conclusions

In the present thesis, the fundamental colloidal properties of h-HNTs particles as well as their potential applicability in antioxidant systems were comprehensively investigated. The interactions of h-HNTs with charged species including polyelectrolytes as well as monovalent and multivalent ions were primarily examined in terms of their effects on the stability and charging characteristics. Finally, hybrid materials with significant antioxidant activity were developed by immobilizing enzymes and enzyme mimics on h-HNT-based carriers.

Based on the surface charge and aggregation characteristics, the direct Hofmeister series of monovalent cations was established for the h-HNT particles in the presence of negatively charged hydrophobic surfaces. Specifically, this is the first time, that such a series is established for h-HNTs. The cause of the interparticle forces was revealed by comparing the CCCs evaluated by the DLVO theory and those determined by the experiments. It was found that the aggregation mechanism is controlled by the interplay between the repulsive EDL and attractive van der Waals forces, in accordance with the DLVO theory. However, significant ion specific effects were observed for monovalent counterions due to the different levels of hydration and the resulting variation in the affinity of the cations to the h-HNT surface. The sequence of quantified CCCs corresponds to the direct Hofmeister series suggested for cations in attendance of negatively charged hydrophobic surfaces. In the case of multivalent inorganic electrolytes, it was observed that increasing the valence of metal ions increases the affinity of the counterions to the surface, thus affecting the surface charge density of the particles. The trend in CCC values is in reasonable agreement with the Schulze–Hardy rule for the metal ions. Colloidal stability studies revealed that the particle aggregation mechanism in the case of mono- and multivalent salts, was governed by DLVO-type forces, while the distinction in CCCs was determined by ion adsorption. Such adsorption altered the surface charge density to some extent, however, the overall interparticle forces were controlled by the sum of the repulsive double layer and attractive van der Waals forces.

The colloidal properties of the h-HNT particles were examined in the presence of water-soluble ILs with various cation structures and alkyl chain lengths, and as a result, the Hofmeister series was extended. The unexpectedly potent adsorption of $BMPY^+$ caused charge neutralization and reversal behavior of the negatively charged h-HNT. Besides, the affinity of the IL cations to the surface increased as the alkyl chain length increased. The diverse hydrophobic characteristics of IL cations, which became more apparent as the alkyl chain on

the imidazolium ring increased, are the reason for the variation of CCCs. As a result, the cation with the longest alkyl chain exhibited the strongest affinity to the particle surface, resulting in charge neutralization and overcharging. Such significant adsorption resulted in a lower CCC value. However, within the IL cations, the lowest CCC was measured for $BMPY^+$, while the highest one was determined in the presence of MIM^+, where the adsorption was the weakest. These findings provided the extension of the established Hofmeister series for the h-HNT with IL cations. From studies conducted on the negatively charged h-HNT particles, the established direct Hofmeister series for inorganic and IL cations is the following:

$$Na^+ > MIM^+ > EMIM^+ > K^+ > BMIM^+ > BMPYR^+ > BMPIP^+ > Cs^+ > HMIM^+ > BMPY^+$$

Moreover, it has been demonstrated that positively charged natural PSP and synthetic IP-2 polyelectrolytes strongly adsorb onto negatively charged h-HNT particles. Both polyelectrolytes exhibited high affinity to the oppositely charged nanotubes, and the surface charge was significantly altered by increasing the polyelectrolyte loading. At the appropriate polyelectrolyte dose, adsorption resulted in charge neutralization and reversal. By adjusting the polyelectrolyte dose, particle aggregation could be regulated, and stable dispersions were observed when the polyelectrolyte concentration was sufficient to cover the entire outer surface of the h-HNTs, i.e., no tendencies toward aggregation were observed at this appropriate dose. These results are qualitatively consistent with the predictions of the DLVO theory. Dispersion characteristics of h-HNT-PSP and h-HNT-IP-2, prepared at polyelectrolyte doses, where the saturated layer is formed, are very similar. However, the IP-2 polymer exhibited unanticipated behavior because of its propensity to mask specific effects of co-ions. On the other hand, the aggregation mechanism was realized within the DLVO theory in all systems studied. The saturated IP-2 layer on the h-HNT particles masked ion specific effects and the colloidal stability of h-HNT-IP-2 depended only on the ionic strength applied in the dispersions.

Besides, a highly active antioxidant material composed of h-HNT, PSP, and SOD enzyme was developed through the self-assembly of the biomacromolecules on the nanoparticulate support. The SOD adsorption on the PSP-modified nanotubes was confirmed by spectroscopy methods, and the results indicated successful immobilization of SOD and a high level of structural stability. As pointed out in enzymatic assays, SOD retained its structural and functional integrity after immobilization since the h-HNT-PSP-SOD material exhibited SOD-like activity that was very similar to the one found for the support-free enzyme. In this way, stable bionanocomposite dispersions of antioxidant activity were developed, which can be applied as superoxide radical scavengers in heterogeneous samples. Finally, the interactions

between the SOD-mimicking metal complex and the three types of nanotubular systems were evaluated. Bare h-HNT and polyelectrolyte-modified (h-HNT-PSP and h-HNT-IP-2) nanoparticles were used as a support for the adsorption of the SOD-mimicking Cu(Cit) complex. The adsorption of the Cu(Cit) complex was the strongest on h-HNT-PSP, which was ascribed to electrostatic and hydrogen bonding interactions between the ligand and the PSP chains on the surface. In the case of bare h-HNTs, on the like-charge surface, a small extent of complex adsorption was observed only at elevated complex concentrations. On the other hand, in the case of functionalized h-HNT particles, the charge neutralization and reversal appeared as a result of the adsorption of the Cu(Cit) complex. The bare h-HNT dispersions were colloidally stable in the presence of Cu(Cit) complex, and the samples showed no signs of particle aggregation within the whole concentration range examined. However, the size data for the h-HNT-PSP and h-HNT-IP-2 considerably increased, as the complex concentration increased, designating the particle aggregation. It was discovered that surface functionalization is essential for the adsorption processes of metal complexes onto particles. The generated nanocomposites were probed in the dismutation of superoxides and exhibited remarkable antioxidant activities. These nanotubular systems are preferred for antioxidant agents in various processes where native or entrapped enzymes are not appropriate choices owing to their marked susceptibility to environmental conditions and consequent loss of enzymatic activity.

7. Summary

Due to numerous applications of particle dispersions in liquid phases, understanding their colloidal behavior is one of the critical issues. Different stabilizing agents can be utilized to tune the colloidal stability of the particle dispersions. Since stable dispersions are required in many applications, aggregation processes and the pertinent colloidal stability must be taken into consideration. Controlling the colloidal stability of particle dispersions is beneficial also when employing them as carriers in different immobilization processes of various compounds such as drug molecules, enzymes, or molecular antioxidants. Natural antioxidant enzymes such as SOD are the most effective tool for combating oxidative stress and minimizing its harmful effects. However, the utilization of native enzymes as catalysts is constrained by their high cost, poor stability, and the inability of reusing. To some extent, these restrictions can be overcome by employing various approaches, such as the immobilization of native enzymes on nanoparticulate carriers or the development of nanocomposites with enzyme-like functions. Whether the immobilized enzyme will find practical utilization depends to a large extent on the carrier used.

HNTs are an attractive group of materials in many respects such as broad-spectrum accessibility, biocompatibility, affordability in price, and non-typical dual charge properties. These benefits have attracted interest in clay nanotubes among scientists in recent years. Despite the significant research on their applicability and solid-state physicochemical properties, there is limited information about the basic colloidal stability of HNT dispersions in liquid media. The present thesis focuses on the fundamental investigations of the interaction of HNTs with differently charged species, starting from simple mono- and multivalent inorganic electrolytes to novel types of solutions such as ILs. Within this part, the tuning of the colloidal stability of HNT material by surface functionalization was also investigated. The DLVO theory, the Hofmeister series, and the Schulze–Hardy rule provided good explanations of the influence of these charged species on the colloidal stability of HNT particles. After an extensive study on the basic colloidal behavior of HNT materials, the research went toward applying this material in the field of antioxidant systems development. Prior to any investigations, commercially obtained HNT material was alkali treated, and the hydroxylated form, called h-HNT, was used.

In the first phase of the study, light scattering techniques were used to investigate the influence of simple monovalent electrolytes (NaCl, KCl, and CsCl) on the surface charge and aggregation of h-HNT particles in dilute aqueous solutions. Measured electrophoretic

mobilities, whose magnitudes decreased with salt concentration and remained negative throughout the investigated range, confirmed the varied extent of adsorption of the cation. The magnitude of the mobilities increased significantly in the following $Cs^+ < K^+ < Na^+$ order, indicating ion specific interactions with the surface of the h-HNT particles. The CCC of the h-HNT dispersions increased in $Cs^+ < K^+ < Na^+$ order due to the influence of the destabilizing force of inorganic cations on the h-HNT surface. This sequence is consistent with the direct Hofmeister series for negatively charged hydrophobic surfaces, as the one determined by electrophoretic mobility measurements. Good agreement was found between the experimental CCCs and those calculated according to the DLVO theory. This information showed that the differentiation of CCC values in the presence of various cations is caused by ion specific adsorption, while the aggregation mechanism is regulated by the interplay between the repulsive electrical double layer and the attractive van der Waals forces. Based on surface charge and aggregation data, the direct Hofmeister series for cations in the presence of negatively charged hydrophobic surfaces was established for the h-HNT particles. The aggregation and charging properties were investigated in the presence of multivalent salts ($MgCl_2$ and $LaCl_3$), and findings were compared with those obtained in the presence of monovalent KCl. The Schulze–Hardy rule was used to explain how multivalent counterions destabilized h-HNT dispersions at lower CCC values than monovalent ones. The fact that the affinity of metal ions to the surface increases with increasing valence was confirmed by significant variations of electrophoretic mobility values with salt concentrations. In the case of La^{3+} in suitable concentration, charge neutralization and subsequent reversal occurred. Determined CCCs were decreased in the following order: $K^+ > Mg^{2+} > La^{3+}$. The varying extent of ion adsorption led to this sequence, which is consistent with the Schulze–Hardy rule. Here, as well, the mechanism of particle aggregation in each system is controlled by the interplay between double layer and van der Waals forces, indicating a homogeneous charge distribution on the h-HNT surface, independent of the specific adsorption of cations. The findings in this chapter emphasize the importance of the colloidal behavior of negatively charged h-HNT particles dispersed in aqueous solutions of inorganic electrolytes and, more importantly, the possibility of establishing a direct Hofmeister series for simple ions in the presence of h-HNT particles, which was performed successfully.

In the second chapter, the colloidal stability of bare h-HNTs was investigated in the presence of aqueous solution of ILs. The charging and aggregation properties of h-HNTs were investigated in the presence of IL constituents with different cation structures, such as BMIMCl,

BMPYCl, BMPYRCl, and BMPIPCl, and in the presence of imidazolium-based ILs with different alkyl chain lengths, such as MIMCl, EMIMCl, BMIMCl, and HMIMCl. The measured electrophoretic mobilities revealed that charge neutralization and reversal occurred in the case of $BMPY^+$, while for the other systems the absolute values decreased with IL concentration and remained negative within the whole concentration range studied. The magnitudes of electrophoretic mobilities (at the same IL concentration) and the obtained CCCs decreased in the following order: $BMIM^+ > BMPYR^+ > BMPIP^+ > BMPY^+$, which clearly indicates that $BMPY^+$ showed the highest affinity to the h-HNT surface. In the presence of imidazolium-based ILs, it was discovered that increasing the length of alkyl chains of imidazolium cations enhanced the affinity of counterions to the surface. As a result, the electrical double layer repulsion weakened in the following order: $MIM^+ > EMIM^+ > BMIM^+ > HMIM^+$, due to this charge compensation. The CCCs also followed the above-mentioned sequence, but the mechanism of particle aggregation was predicted by the DLVO theory. The hydrophobicity of these counterions increased by increasing the alkyl chain on the imidazolium ring, which resulted in such a CCC sequence. The importance of the results presented in this chapter is reflected in the fact that the established direct Hofmeister series for h-HNT particles was also extended with IL cations. Based on all these results, the direct Hofmeister series for cations (simple inorganic and IL cations) in the presence of h-HNT particles was established as follows:

$$Na^+ > MIM^+ > EMIM^+ > K^+ > BMIM^+ > BMPYR^+ > BMPIP^+ > Cs^+ > HMIM^+ > BMPY^+$$

These findings provide fresh information that may be crucial for the interfacial assembly of IL constituents, which is essential to control and predict the colloidal behavior of h-HNT particle dispersions in ILs.

The third chapter describes the functionalization of the h-HNT particles, with two types of polyelectrolytes, such as natural PSP and synthetic IP-2 polyelectrolytes. The polyelectrolytes are positively charged, and the functionalization of the h-HNT was performed through the adsorption process followed by charging and aggregation measurements. At low amounts of the PSP or IP-2, the surface charge of the h-HNT particles was partially compensated by the adsorbed polyelectrolytes, as evidenced by the negative electrophoretic mobility values recorded at low polyelectrolyte doses. The increase in mobility by increasing the concentration of PSP or IP-2, leading to charge neutralization at intermediate doses, is an obvious indication of such an adsorption process. After the charge neutralization point, the adsorption process continued leading to the charge reversal behavior of the h-HNT particles. Higher doses of polyelectrolytes resulted in the saturation of the surface with PSP or IP-2 layer, as indicated by

the plateau in the electrophoretic mobility values. The influence of polyelectrolyte dose on the stability was clearly determined. The measured stability ratio values of the h-HNT particles were extremely high, indicating that they were stable at both low and high polyelectrolyte doses, while at the charge neutralization point the stability ratios revealed the form of a U-shape curve and reached a minimum, suggesting rapid particle aggregation and unstable systems. These results are qualitatively consistent with the prediction of the DLVO theory, as sufficiently charged particles remain stable due to repulsion between the electrical double layers, while attractive van der Waals forces destabilize the samples at charge neutralization. When prepared at polyelectrolyte doses where the saturated layer is formed, h-HNT-PSP and h-HNT-IP-2 particles have similar dispersion properties. Compared to the bare particles, surface modification of h-HNT particles with polyelectrolytes enhances their resistance to salt-induced aggregation. However, once the charging and aggregation properties of h-HNT-IP-2 particles were examined in the presence of salt and IL solutions, a very unexpected behavior was revealed compared to the results obtained for bare h-HNT particles. Namely, the IP-2 polymer showed a strong masking effect for ion specific effects, since the determined CCC values, as well as the surface charge density values, were the same regardless of the type of ions present in the solutions. Therefore, the colloidal stability of the h-HNT-IP-2 particles depended only on the applied ionic strength in the dispersion. The results obtained in this chapter confirm that positively charged PSP and IP-2 polyelectrolytes adsorb strongly and irreversibly onto oppositely charged h-HNT particles. This is important because this type of surface modification can improve the colloidal properties of the particles in terms of stability and the preparation of these particles for future immobilization processes. Additionally, specific, and atypical behavior of the IP-2 polymer was discovered.

In the final stage, highly active antioxidants based on h-HNT, PSP, and SOD were developed by self-assembly of the biomacromolecules on the nanoparticulate carrier. Also, at this stage, the influence of bare and functionalized h-HNT particles on the SOD-like activity of an enzyme-mimicking Cu(Cit) metal complex was assessed. Upon surface functionalization of h-HNT particles with PSP polyelectrolyte, the SOD enzyme was adsorbed onto h-HNT-PSP support via electrostatic and hydrogen bonding interactions, resulting in the formation of the h-HNT-PSP-SOD bionanocomposite. Microscopy, scattering, and spectroscopy techniques revealed the exceptional structural and colloidal stability of the prepared nanocomposite. After successful and proven immobilization of the SOD enzyme, the superoxide scavenging activity was probed using an enzymatic assay. It was revealed that the activity was higher for the

h-HNT-PSP-SOD system than for the native SOD, indicating that the SOD enzyme retained its functional integrity after immobilization, while the total positive charge of the composite generated substrate attraction and higher activity. Within this part, another aim was to investigate how the h-HNT particles may affect the SOD-like activity of an enzyme-mimicking metal complex. Hence, Cu(Cit) complex was adsorbed on bare and functionalized h-HNT with PSP and IP-2 polyelectrolytes. It was confirmed that the functionalization of the surface has a great influence on the adsorption of the complexes on the particles. Namely, the Cu(Cit) complex was found to exhibit the strongest adsorption on h-HNT-PSP, which was attributed to the enhanced electrostatic and hydrogen bonding interactions of the complex and the PSP chains on the surface. In both cases, in solution and after immobilization, Cu(Cit) complex retained a dimeric structure. Aggregation assessment revealed that the colloidal stability of bare h-HNT particles was not affected by Cu(Cit) complex, i.e., the measured hydrodynamic radii and polydispersity did not change with increasing the complex concentration, indicating stable systems. However, in the case of h-HNT-PSP and h-HNT-IP-2, a considerable increase in measured size and polydispersity index data was observed with increasing complex concentration, which indicates particle aggregation. Additionally, in the case of PSP-coated h-HNT, this process was observed even at lower complex concentrations, and this agrees with data recorded in charging measurements. The adsorption of Cu(Cit) on the oppositely charged surface (PSP- and IP-2-modified particles) resulted in charge neutralization. Under these experimental conditions, the repulsive interparticle forces, resulting from the overlap of the electric double layers vanish, then the attractive dispersion forces prevail, leading to the aggregation of the particles. The evaluation of antioxidant activity was performed for each of the three nanotubular systems after the Cu(Cit) adsorption. Due to the structural changes caused by the surface-complex interaction and the advantageous interferences between the radicals and the oppositely charged particles, it was found that higher superoxide scavenging activities were obtained in the presence of polyelectrolyte-coated h-HNT particles than for the non-immobilized Cu(Cit). Based on all these findings, it can be concluded the developed h-HNT-PSP-SOD nanocomposite can be considered as a very effective antioxidant that can be used in heterogeneous samples. In addition, obtained results indicate considerable potential for the development of SOD-like h-HNT-based nanocomposites that may be less sensitive to environmental conditions than native enzymes.

8. Acknowledgment

First of all, I would like to express my sincere and deep gratitude to my PhD supervisor Dr. István Szilágyi for the opportunity to work in his Biocolloids Research Group that I joined in September 2018. I am extremely grateful for his great patience, advice, professionalism, and for his assistance at every stage of my PhD studies. Without his guidance, and efforts, as well as the provision of all the necessary financial resources, I would not have been able to complete my doctoral studies.

I am very grateful to the head of the Department of Physical Chemistry and Materials Science, Prof. Ágota Tóth for the opportunity to conduct my PhD studies at the mentioned department.

I would like to thank Dr. Paul Rouster for his help at the beginning and during my PhD studies. I am grateful for all his advice and fruitful cooperation. His expertise in this field was very helpful to me and I really appreciate it.

I am also thankful to Prof. Alain M. Jonas for allowing me to spend one month at the BSMA, IMCN Institute at the Université Catholique de Louvain. I thank for the opportunity to get acquainted with new insights, as well as for the friendly atmosphere in the laboratory.

I am grateful to Prof. Paul Dyson from the EPF Lausanne for providing the IP-2 polyelectrolyte and for the collaboration.

I would like to thank our secretaries Ildikó Patakiné Sziveri, Karolina Baráthné Takács, and Csilla Barra for their help and efforts in solving many administrative issues.

I am grateful to current (Dóri, Adél, Szilárd, Nizar, Zsófi, Kata, and Gréta) and former (Zoli and Szabi) members of the Biocolloids Research Group for the nice working atmosphere and for making my life and my work in Szeged more convenient. I am thankful for their support and many nice memories.

I would like to thank all my relatives and friends for their immense support, love, and understanding during all these years.

Finally, I owe the greatest gratitude to my loving parents and my brother for their endless love and support during my studies and during the preparation of this dissertation. I am grateful for their encouragement, unwavering support, and belief in me throughout my life.

9. References

1. de Gennes, P. G., Ultradivided matter. *Nature* 2001**,** *412* (6845), 385-385.
2. Bolto, B.; Gregory, J., Organic polyelectrolytes in water treatment. *Water Res.* 2007**,** *41* (11), 2301-2324.
3. Nasser, M. S.; Twaiq, F. A.; Onaizi, S. A., Effect of polyelectrolytes on the degree of flocculation of papermaking suspensions. *Sep. Purif. Technol.* 2013**,** *103*, 43-52.
4. Jadhav, R. S.; Patil, K. J.; Hundiwale, D. G.; Mahulikar, P. P., Synthesis of waterborne nanopolyanilne latexes and application of nanopolyaniline particles in epoxy paint formulation for smart corrosion resistivity of carbon steel. *Polym. Adv. Technol.* 2011**,** *22* (12), 1620-1627.
5. Bao, W. L.; Wang, J. Y.; Wang, Q.; O'Hare, D.; Wan, Y. L., Layered double hydroxide nanotransporter for molecule delivery to intact plant cells. *Sci. Rep.* 2016**,** *6*, 26738.
6. Chiu, C.-W.; Lin, J.-J., Self-assembly behavior of polymer-assisted clays. *Prog. Polym. Sci.* 2012**,** *37* (3), 406-444.
7. Chiu, C. W.; Lee, T. C.; Hong, P. D.; Lin, J. J., Controlled self-assemblies of clay silicate platelets by organic salt modifier. *RSC Adv.* 2012**,** *2* (22), 8410-8415.
8. Russel, W. B.; Saville, D. A.; Schowalter, W. R., *Colloidal dispersions*. Cambridge University Press: Cambridge, 1989.
9. Dickinson, E., Food emulsions and foams: Stabilization by particles. *Curr. Opin. Colloid Interface Sci.* 2010**,** *15* (1-2), 40-49.
10. Dickinson, E., Food colloids research: Historical perspective and outlook. *Adv. Colloid Interface Sci.* 2011**,** *165* (1), 7-13.
11. Dickinson, E., Structuring of colloidal particles at interfaces and the relationship to food emulsion and foam stability. *J. Colloid Interface Sci.* 2015**,** *449*, 38-45.
12. Tiarks, F.; Frechen, T.; Kirsch, S.; Leuninger, J.; Melan, M.; Pfau, A.; Richter, F.; Schuler, B.; Zhao, C. L., Formulation effects on the distribution of pigment particles in paints. *Prog. Org. Coat.* 2003**,** *48* (2-4), 140-152.
13. Xu, Z. P.; Zeng, Q. H.; Lu, G. Q.; Yu, A. B., Inorganic nanoparticles as carriers for efficient cellular delivery. *Chem. Eng. Sci.* 2006**,** *61* (3), 1027-1040.
14. Sharma, V. K.; Filip, J.; Zboril, R.; Varma, R. S., Natural inorganic nanoparticles - formation, fate, and toxicity in the environment. *Chem. Soc. Rev.* 2015**,** *44* (23), 8410-8423.
15. Gallo, J.; Panacek, A.; Prucek, R.; Kriegova, E.; Hradilova, S.; Hobza, M.; Holinka, M., Silver Nanocoating Technology in the Prevention of Prosthetic Joint Infection. *Materials* 2016**,** *9* (5).
16. Sadjadi, S.; Akbari, M.; Heravi, M. M., Palladated nanocomposite of halloysite-nitrogen-doped porous carbon prepared from a novel cyano-/nitrile-free task specific ionic liquid: An efficient catalyst for hydrogenation. *ACS Omega* 2019**,** *4* (21), 19442-19451.
17. Joseph, A.; Mathew, K. P. J.; Vandana, S., Zirconium-doped ceria nanoparticles as anticorrosion pigments in waterborne epoxy-polymer coatings. *ACS Appl. Nano Mater.* 2021**,** *4* (1), 834-849.
18. Bahri-Laleh, N.; Sadjadi, S.; Poater, A., Pd immobilized on dendrimer decorated halloysite clay: Computational and experimental study on the effect of dendrimer generation, Pd valance and incorporation of terminal functionality on the catalytic activity. *J. Colloid Interface Sci.* 2018**,** *531*, 421-432.
19. Eda, G.; Yamaguchi, H.; Voiry, D.; Fujita, T.; Chen, M. W.; Chhowalla, M., Photoluminescence from chemically exfoliated MoS_2. *Nano Lett.* 2011**,** *11* (12), 5111-5116.
20. Das, P.; Zhong, W. H.; Claverie, J. P., Copolymer nanosphere encapsulated CdS quantum dots prepared by RAFT copolymerization: synthesis, characterization and mechanism of formation. *Colloid Polym. Sci.* 2011**,** *289* (14), 1519-1533.
21. McNamara, K.; Tofail, S. A. M., Nanoparticles in biomedical applications. *Adv. Phys.*-

X 2017**,** *2* (1), 54-88.
22. Lin, S. C.; Shih, C. J.; Sresht, V.; Rajan, A. G.; Strano, M. S.; Blankschtein, D., Understanding the colloidal dispersion stability of 1D and 2D materials: Perspectives from molecular simulations and theoretical modeling. *Adv. Colloid Interface Sci.* 2017**,** *244*, 36-53.
23. Singhal, J.; Verma, S.; Kumar, S., The physio-chemical properties and applications of 2D nanomaterials in agricultural and environmental sustainability. *Sci. Total Environ.* 2022**,** *837*, 155669.
24. Li, C. P.; Liu, J. G.; Qu, X. Z.; Yang, Z. Z., A General Synthesis Approach toward Halloysite-Based Composite Nanotube. *J. Appl. Polym. Sci.* 2009**,** *112* (5), 2647-2655.
25. Kasuga, T.; Hiramatsu, M.; Hoson, A.; Sekino, T.; Niihara, K., Titania nanotubes prepared by chemical processing. *Adv. Mater.* 1999**,** *11* (15), 1307-1311.
26. Rao, C. N. R.; Nath, M., Inorganic nanotubes. *Dalton Trans.* 2003**,** (1), 1-24.
27. Subramanian, V. R.; Sarker, S.; Yu, B. W.; Kar, A.; Sun, X. D.; Dey, S. K., TiO_2 nanotubes and its composites: Photocatalytic and other photo-driven applications. *J. Mater. Res.* 2013**,** *28* (3), 280-293.
28. Huang, J. Q.; Zhang, Q.; Zhao, M. Q.; Wei, F., A review of the large-scale production of carbon nanotubes: The practice of nanoscale process engineering. *Chin. Sci. Bull.* 2012**,** *57* (2-3), 157-166.
29. Sun, Y. P.; Fu, K. F.; Lin, Y.; Huang, W. J., Functionalized carbon nanotubes: Properties and applications. *Accounts Chem. Res.* 2002**,** *35* (12), 1096-1104.
30. Damodaran, V. B.; Bhatnagar, D.; Leszczak, V.; Popat, K. C., Titania nanostructures: a biomedical perspective. *RSC Adv.* 2015**,** *5* (47), 37149-37171.
31. Bergaya, F.; Lagaly, G., *Handbook of Clay Science*. Second ed.; Elsevier: Amsterdam, 2013.
32. Annabi-Bergaya, F., Layered clay minerals. Basic research and innovative composite applications. *Microporous Mesoporous Mat.* 2008**,** *107* (1-2), 141-148.
33. Tombacz, E.; Szekeres, M., Surface charge heterogeneity of kaolinite in aqueous suspension in comparison with montmorillonite. *Appl. Clay Sci.* 2006**,** *34* (1-4), 105-124.
34. Lagaly, G.; Ziesmer, S., Colloid chemistry of clay minerals: the coagulation of montmorillonite dispersions. *Adv. Colloid Interface Sci.* 2003**,** *100*, 105-128.
35. Massaro, M.; Noto, R.; Riela, S., Past, present and future perspectives on halloysite clay minerals. *Molecules* 2020**,** *25* (20).
36. Tosheva, L.; Valtchev, V. P., Nanozeolites: Synthesis, crystallization mechanism, and applications. *Chem. Mat.* 2005**,** *17* (10), 2494-2513.
37. Bergaya, F.; Lagaly, G., *Handbook of Clay Science*. Second ed.; Elsevier: Amsterdam, 2013.
38. Hanif, M.; Jabbar, F.; Sharif, S.; Abbas, G.; Farooq, A.; Aziz, M., Halloysite nanotubes as a new drug-delivery system: a review. *Clay Min.* 2016**,** *51* (3), 469-477.
39. Zhang, Y.; Tang, A. D.; Yang, H. M.; Ouyang, J., Applications and interfaces of halloysite nanocomposites. *Appl. Clay Sci.* 2016**,** *119*, 8-17.
40. Pasbakhsh, P.; De Silva, R.; Vahedi, V.; Churchman, G. J., Halloysite nanotubes: prospects and challenges of their use as additives and carriers - A focused review. *Clay Min.* 2016**,** *51* (3), 479-487.
41. Santos, A. C.; Ferreira, C.; Veiga, F.; Ribeiro, A. J.; Panchal, A.; Lvov, Y.; Agarwal, A., Halloysite clay nanotubes for life sciences applications: From drug encapsulation to bioscaffold. *Adv. Colloid Interface Sci.* 2018**,** *257*, 58-70.
42. Ruiz-Hitzky, E.; Aranda, P.; Darder, M.; Rytwo, G., Hybrid materials based on clays for environmental and biomedical applications. *J. Mater. Chem.* 2010**,** *20* (42), 9306-9321.
43. Vaccari, A., Clays and catalysis: a promising future. *Appl. Clay Sci.* 1999**,** *14* (4), 161-198.

44. Vaccari, A., Preparation and catalytic properties of cationic and anionic clays. *Catal. Today* 1998**,** *41* (1-3), 53-71.
45. Abdullayev, E.; Lvov, Y., Halloysite clay nanotubes for controlled release of protective agents. *J. Nanosci. Nanotechnol.* 2011**,** *11* (11), 10007-10026.
46. Yuan, P.; Tan, D. Y.; Annabi-Bergaya, F., Properties and applications of halloysite nanotubes: recent research advances and future prospects. *Appl. Clay Sci.* 2015**,** *112*, 75-93.
47. Lvov, Y.; Wang, W. C.; Zhang, L. Q.; Fakhrullin, R., Halloysite clay nanotubes for loading and sustained release of functional compounds. *Adv. Mater.* 2016**,** *28* (6), 1227-1250.
48. Lvov, Y.; Abdullayev, E., Functional polymer-clay nanotube composites with sustained release of chemical agents. *Prog. Polym. Sci.* 2013**,** *38* (10-11), 1690-1719.
49. Lvov, Y. M.; Shchukin, D. G.; Mohwald, H.; Price, R. R., Halloysite clay nanotubes for controlled release of protective agents. *ACS Nano* 2008**,** *2* (5), 814-820.
50. Lazzara, G.; Cavallaro, G.; Panchal, A.; Fakhrullin, R.; Stavitskaya, A.; Vinokurov, V.; Lvov, Y., An assembly of organic-inorganic composites using halloysite clay nanotubes. *Curr. Opin. Colloid Interface Sci.* 2018**,** *35*, 42-50.
51. Frost, R. L., Fourier-transform Raman-spectroscopy of kaolinite, dickite and halloysite. *Clay Clay Min.* 1995**,** *43* (2), 191-195.
52. Mitra, G. B.; Bhattacherjee, S., Structure of halloysite. *Acta Crystallogr. Sect. B-Struct. Commun.* 1975**,** *31* (DEC15), 2851-2857.
53. Vergaro, V.; Abdullayev, E.; Lvov, Y. M.; Zeitoun, A.; Cingolani, R.; Rinaldi, R.; Leporatti, S., Cytocompatibility and uptake of halloysite clay nanotubes. *Biomacromolecules* 2010**,** *11* (3), 820-826.
54. Dionisi, C.; Hanafy, N.; Nobile, C.; De Giorgi, M. L.; Rinaldi, R.; Casciaro, S.; Lvov, Y. M.; Leporatti, S., Halloysite Clay Nanotubes as Carriers for Curcumin: Characterization and Application. *IEEE Trans. Nanotechnol.* 2016**,** *15* (5), 720-724.
55. Tan, C. Y.; Zheng, J. Q.; Feng, Y.; Liu, M. X., Cell membrane-coated halloysite nanotubes for target-specific nanocarrier for cancer phototherapy. *Molecules* 2021**,** *26* (15), 17.
56. Karewicz, A.; Machowska, A.; Kasprzyk, M.; Ledwojcik, G., Application of halloysite nanotubes in cancer therapy-A review. *Materials* 2021**,** *14* (11), 24.
57. Horky, P.; Skalickova, S.; Baholet, D.; Skladanka, J., Nanoparticles as a solution for eliminating the risk of mycotoxins. *Nanomaterials* 2018**,** *8* (9), 727.
58. Fizir, M.; Dramou, P.; Dahiru, N. S.; Ruya, W.; Huang, T.; He, H., Halloysite nanotubes in analytical sciences and in drug delivery: A review. *Microchim. Acta* 2018**,** *185* (8), 389.
59. Lvov, Y.; Aerov, A.; Fakhrullin, R., Clay nanotube encapsulation for functional biocomposites. *Adv. Colloid Interface Sci.* 2014**,** *207*, 189-198.
60. Massaro, M.; Noto, R.; Riela, S., Halloysite nanotubes: Smart nanomaterials in catalysis. *Catalysts* 2022**,** *12* (2), 27.
61. Lisuzzo, L.; Cavallaro, G.; Milioto, S.; Lazzara, G., Pickering emulsions stabilized by halloysite nanotubes: From general aspects to technological applications. *Adv. Mater. Interfaces* 2022**,** *9* (10), 2102346.
62. Li, Q. Q.; Ren, T.; Perkins, P.; Hu, X. F.; Wang, X. L., Applications of halloysite nanotubes in food packaging for improving film performance and food preservation. *Food Control* 2021**,** *124*, 8.
63. Yang, X. H.; Cai, J. B.; Chen, L. H.; Cao, X.; Liu, H. Z.; Liu, M. X., Green detergent made of halloysite nanotubes. *Chem. Eng. J.* 2021**,** *425*, 10.
64. Hari, J.; Sarkozi, M.; Foldes, E.; Pukanszky, B., Long term stabilization of PE by the controlled release of a natural antioxidant from halloysite nanotubes. *Polym. Degrad. Stabil.* 2018**,** *147*, 229-236.
65. Massaro, M.; Amorati, R.; Cavallaro, G.; Guernelli, S.; Lazzara, G.; Milioto, S.;

Noto, R.; Poma, P.; Riela, S., Direct chemical grafted curcumin on halloysite nanotubes as dual-responsive prodrug for pharmacological applications. *Colloid Surf. B* 2016**,** *140*, 505-513.
66. Vergaro, V.; Lvov, Y. M.; Leporatti, S., Halloysite clay nanotubes for resveratrol delivery to cancer cells. *Macromol. Biosci.* 2012**,** *12* (9), 1265-1271.
67. Zhai, R.; Zhang, B.; Liu, L.; Xie, Y. D.; Zhang, H. Q.; Liu, J. D., Immobilization of enzyme biocatalyst on natural halloysite nanotubes. *Catal. Commun.* 2010**,** *12* (4), 259-263.
68. Shchukin, D. G.; Sukhorukov, G. B.; Price, R. R.; Lvov, Y. M., Halloysite nanotubes as biomimetic nanoreactors. *Small* 2005**,** *1* (5), 510-513.
69. Dedzo, G. K.; Detellier, C., Clay minerals-ionic liquids, nanoarchitectures, and applications. *Adv. Funct. Mater.* 2018**,** *28* (27), 1703845.
70. Infurna, G.; Cavallaro, G.; Lazzara, G.; Milioto, S.; Dintcheva, N. T., Bionanocomposite films containing halloysite nanotubes and natural antioxidants with enhanced performance and durability as promising materials for cultural heritage protection. *Polymers* 2020**,** *12* (9), 16.
71. Cavallaro, G.; Milioto, S.; Lazzara, G., Halloysite nanotubes: Interfacial properties and applications in cultural heritage. *Langmuir* 2020**,** *36* (14), 3677-3689.
72. Lisuzzo, L.; Cavallaro, G.; Parisi, F.; Milioto, S.; Lazzara, G., Colloidal stability of halloysite clay nanotubes. *Ceram. Int.* 2019**,** *45* (2), 2858-2865.
73. Cavallaro, G.; Lazzara, G.; Taormina, V.; Cascio, D., Sedimentation of halloysite nanotubes from different deposits in aqueous media at variable ionic strengths. *Colloid Surf. A-Physicochem. Eng. Asp.* 2019**,** *576*, 22-28.
74. Hari, J.; Gyurki, A.; Sarkozi, M.; Foldes, E.; Pukanszky, B., Competitive interactions and controlled release of a natural antioxidant from halloysite nanotubes. *J. Colloid Interface Sci.* 2016**,** *462*, 123-129.
75. Yang, Y. T.; Chen, Y.; Leng, F.; Huang, L.; Wang, Z. J.; Tian, W. Q., Recent advances on surface modification of halloysite nanotubes for multifunctional applications. *Appl. Sci.-Basel* 2017**,** *7* (12), 1215.
76. Matusik, J.; Hyla, J.; Maziarz, P.; Rybka, K.; Leiviska, T., Performance of halloysite-Mg/Al LDH materials for aqueous As(V) and Cr(VI) removal. *Materials* 2019**,** *12* (21), 3569.
77. Kim, J.; Ryu, J.; Shin, J.; Lee, H.; Kim, I. S.; Sohn, D., Interactions between halloysite nanotubes and poly(styrene sulfonate) in solution. *Bull. Korean Chem. Soc.* 2017**,** *38* (1), 107-111.
78. Joo, Y.; Sim, J. H.; Jeon, Y.; Lee, S. U.; Sohn, D., Opening and blocking the inner-pores of halloysite. *Chem. Commun.* 2013**,** *49* (40), 4519-4521.
79. Rouster, P.; Dondelinger, M.; Galleni, M.; Nysten, B.; Jonas, A. M.; Glinel, K., Layer-by-layer assembly of enzyme-loaded halloysite nanotubes for the fabrication of highly active coatings. *Colloid Surf. B* 2019**,** *178*, 508-514.
80. Derjaguin, B.; Landau, L. D., Theory of the stability of strongly charged lyophobic sols and of the adhesion of strongly charged particles in solutions of electrolytes. *Acta Phys. Chim.* 1941**,** *14* (6), 633-662.
81. Verwey, E. J. W.; Overbeek, J. T. G., *Theory of stability of lyophobic colloids*. Elsevier: Amsterdam, 1948.
82. Delgado, A. V.; Gonzalez-Caballero, F.; Hunter, R. J.; Koopal, L. K.; Lyklema, J., Measurement and interpretation of electrokinetic phenomena. *J. Colloid Interface Sci.* 2007**,** *309* (2), 194-224.
83. Evans, D. F.; Wennerstrom, H., *The colloidal domain*. John Wiley: New York, 1999.
84. Harding, I. H.; Healy, T. W., Electrical double-layer properties of amphoteric polymer latex colloids. *J. Colloid Interface Sci.* 1985**,** *107* (2), 382-397.
85. Greathouse, J. A.; Feller, S. E.; McQuarrie, D. A., The modified Gouy-Chapman theory - Comparisons between electrical double-layer models of clay swelling. *Langmuir* 1994**,** *10* (7),

2125-2130.
86. Elimelech, M.; Gregory, J.; Jia, X.; Williams, R. A., *Particle deposition and aggregation: Measurement, modeling, and simulation*. Butterworth-Heinemann Ltd.: Oxford, 1995.
87. Ruiz-Cabello, F. J. M.; Trefalt, G.; Oncsik, T.; Szilagyi, I.; Maroni, P.; Borkovec, M., Interaction forces and aggregation rates of colloidal latex particles in the presence of monovalent counterions. *J. Phys. Chem. B* 2015**,** *119* (25), 8184-8193.
88. Gudarzi, M. M.; Trefalt, G.; Szilagyi, I.; Maroni, P.; Borkovec, M., Forces between negatively charged interfaces in the presence of cationic multivalent oligoamines measured with the atomic force microscope. *J. Phys. Chem. C* 2015**,** *119* (27), 15482-15490.
89. Zaccone, A.; Wu, H.; Lattuada, M.; Morbidelli, M., Correlation between colloidal stability and surfactant adsorption/association phenomena studied by light scattering. *J. Phys. Chem. B* 2008**,** *112* (7), 1976-1986.
90. Fritz, G.; Schadler, V.; Willenbacher, N.; Wagner, N. J., Electrosteric stabilization of colloidal dispersions. *Langmuir* 2002**,** *18* (16), 6381-6390.
91. Israelachvili, J., *Intermolecular and surface forces*. 3 ed.; Academic Press: London, 2011.
92. Lopez-Leon, T.; Ortega-Vinuesa, J. L.; Bastos-Gonzalez, D., Ion-specific aggregation of hydrophobic particles. *ChemPhysChem* 2012**,** *13* (9), 2382-2391.
93. Lopez-Leon, T.; Jodar-Reyes, A. B.; Bastos-Gonzalez, D.; Ortega-Vinuesa, J. L., Hofmeister effects in the stability and electrophoretic mobility of polystyrene latex particles. *J. Phys. Chem. B* 2003**,** *107* (24), 5696-5708.
94. Lopez-Leon, T.; Jodar-Reyes, A. B.; Ortega-Vinuesa, J. L.; Bastos-Gonzalez, D., Hofmeister effects on the colloidal stability of an IgG-coated polystyrene latex. *J. Colloid Interface Sci.* 2005**,** *284*, 139-148.
95. Lopez-Leon, T.; Santander-Ortega, M. J.; Ortega-Vinuesa, J. L.; Bastos-Gonzalez, D., Hofmeister effects in colloidal systems: Influence of the surface nature. *J. Phys. Chem. C* 2008**,** *112* (41), 16060-16069.
96. Dumont, F.; Warlus, J.; Watillon, A., Influence of the point of zero charge of titanium-dioxide hydrosols on the ionic adsorption sequences. *J. Colloid Interface Sci.* 1990**,** *138* (2), 543-554.
97. Dumont, F.; Watillon, A., Stability of ferric oxide hydrosols. *Discuss. Farad. Soc.* 1971**,** *52*, 352-380.
98. Peula-Garcia, J. M.; Ortega-Vinuesa, J. L.; Bastos-Gonzalez, D., Inversion of Hofmeister series by changing the surface of colloidal particles from hydrophobic to hydrophilic. *J. Phys. Chem. C* 2010**,** *114* (25), 11133-11139.
99. Tezak, B.; Matijevic, E.; Schulz, K. F., Coagulation of hydrophobic sols in statu nascendi 3. The influence of the ionic size and valency of the counterion. *J. Phys. Chem.* 1955**,** *59* (8), 769-773.
100. Sprycha, R., Electrical double-layer at alumina electrolyte interface 1. Surface-charge and zeta potential. *J. Colloid Interface Sci.* 1989**,** *127* (1), 1-11.
101. Tadros, T. F.; Lyklema, J., Adsorption of potential determining ions at silica-aqueous electrolyte interface and role of some cations. *J. Electroanal. Chem.* 1968**,** *17* (3-4), 267-275.
102. Morag, J.; Dishon, M.; Sivan, U., The governing role of surface hydration in ion specific adsorption to silica: An AFM-based account of the Hofmeister universality and its reversal. *Langmuir* 2013**,** *29* (21), 6317-6322.
103. Parsons, D. F.; Salis, A., Hofmeister effects at low salt concentration due to surface charge transfer. *Curr. Opin. Colloid Interface Sci.* 2016**,** *23*, 41-49.
104. Jungwirth, P.; Cremer, P. S., Beyond Hofmeister. *Nat. Chem.* 2014**,** *6* (4), 261-263.
105. Lo Nostro, P.; Ninham, B. W., Hofmeister phenomena: An update on ion specificity in

biology. *Chem. Rev.* 2012**,** *112* (4), 2286-2322.
106. Kunz, W.; Henle, J.; Ninham, B. W., 'Zur lehre von der wirkung der salze' (about the science of the effect of salts): Franz Hofmeister's historical papers. *Curr. Opin. Colloid Interface Sci.* 2004**,** *9* (1-2), 19-37.
107. Overbeek, J. T. G., The rule of Schulze and Hardy. *Pure Appl. Chem.* 1980**,** *52* (5), 1151-1161.
108. Lyklema, J., Coagulation by multivalent counterions and the Schulze-Hardy rule. *J. Colloid Interface Sci.* 2013**,** *392*, 102-104.
109. Schwierz, N.; Horinek, D.; Netz, R. R., Reversed anionic Hofmeister series: The interplay of surface charge and surface polarity. *Langmuir* 2010**,** *26* (10), 7370-7379.
110. Abendroth, R. P., Behavior of a pyrogenic silica in simple electrolytes. *J. Colloid Interface Sci.* 1970**,** *34* (4), 591-596.
111. Breeuwsma, A.; Lyklema, J., Interfacial electrochemistry of hematite (α-Fe_2O_3). *Discuss. Faraday Soc.* 1971**,** *52*, 324-333.
112. Hall, S. B.; Duffield, J. R.; Williams, D. R., A reassessment of the applicability of the DLVO theory as an explanation for the Schulze-Hardy rule for colloid aggregation. *J. Colloid Interface Sci.* 1991**,** *143* (2), 411-415.
113. Schulze, H., Schwefelarsen in wassriger Losung. *J. Prakt. Chem.* 1882**,** *25* (1), 431-452.
114. Hardy, W. B., A preliminary investigation of the conditions which determine the stability of irreversible hydrosols. *J. Phys. Chem.* 1900**,** *4* (4), 235-253.
115. Rouster, P.; Pavlovic, M.; Szilagyi, I., Destabilization of titania nanosheet suspensions by inorganic salts: Hofmeister series and Schulze-Hardy rule. *J. Phys. Chem. B* 2017**,** *121* (27), 6749-6758.
116. Pavlovic, M.; Huber, R.; Adok-Sipiczki, M.; Nardin, C.; Szilagyi, I., Ion specific effects on the stability of layered double hydroxide colloids. *Soft Matter* 2016**,** *12*, 4024-4033.
117. Higashitani, K.; Nakamura, K.; Fukasawa, T.; Tsuchiya, K.; Mori, Y., Ionic specificity in rapid coagulation of silica nanoparticles. *Langmuir* 2018**,** *34* (7), 2505-2510.
118. Budarz, J. F.; Turolla, A.; Piasecki, A. F.; Bottero, J. Y.; Antonelli, M.; Wiesner, M. R., Influence of aqueous inorganic anions on the reactivity of nanoparticles in TiO2 photocatalysis. *Langmuir* 2017**,** *33* (11), 2770-2779.
119. Yu, W. Y.; Du, N.; Gu, Y. T.; Yan, J. G.; Hou, W. G., Specific ion effects on the colloidal stability of layered double hydroxide single-layer nanosheets. *Langmuir* 2020**,** *36* (23), 6557-6568.
120. Hegedus, T.; Takács, D.; Vasarhelyi, L.; Szilagyi, I.; Konya, Z., Specific ion effects on aggregation and charging properties of boron nitride nanospheres. *Langmuir* 2021**,** *37* (7), 2466-2475.
121. Cao, T.; Szilagyi, I.; Oncsik, T.; Borkovec, M.; Trefalt, G., Aggregation of colloidal particles in the presence of multivalent coions: The inverse Schulze-Hardy rule. *Langmuir* 2015**,** *31* (24), 6610-6614.
122. Trefalt, G.; Szilagyi, I.; Borkovec, M., Poisson-Boltzmann description of interaction forces and aggregation rates involving charged colloidal particles in asymmetric electrolytes. *J. Colloid Interface Sci.* 2013**,** *406*, 111-120.
123. Trefalt, G.; Szilagyi, I.; Borkovec, M., Schulze-Hardy rule revisited. *Colloid Polym. Sci.* 2020**,** *298* (8), 961-967.
124. Trefalt, G.; Szilagyi, I.; Tellez, G.; Borkovec, M., Colloidal stability in asymmetric electrolytes: Modifications of the Schulze-Hardy rule. *Langmuir* 2017**,** *33* (7), 1695-1704.
125. Trefalt, G., Derivation of the inverse Schulze-Hardy rule. *Phys. Rev. E* 2016**,** *93* (3), 032612.
126. Sano, M.; Okamura, J.; Shinkai, S., Colloidal nature of single-walled carbon nanotubes in electrolyte solution: The Schulze-Hardy rule. *Langmuir* 2001**,** *17* (22), 7172-7173.

127. Chen, K. L.; Elimelech, M., Aggregation and deposition kinetics of fullerene (C_{60}) nanoparticles. *Langmuir* 2006**,** *22* (26), 10994-11001.
128. Koetz, J.; Kosmella, S., *Polyelectrolytes and nanoparticles*. Springer: Berlin, 2007.
129. Hyde, E. D. E.; Moreno-Atanasio, R.; Millner, P. A.; Neville, F., Surface charge control through the reversible adsorption of a biomimetic polymer on silica particles. *J. Phys. Chem. B* 2015**,** *119* (4), 1726-1735.
130. Szilagyi, I.; Trefalt, G.; Tiraferri, A.; Maroni, P.; Borkovec, M., Polyelectrolyte adsorption, interparticle forces, and colloidal aggregation. *Soft Matter* 2014**,** *10* (15), 2479-2502.
131. Tiraferri, A.; Maroni, P.; Borkovec, M., Adsorption of polyelectrolytes to like-charged substrates induced by multivalent counterions as exemplified by poly(styrene sulfonate) and silica. *Phys. Chem. Chem. Phys.* 2015**,** *17*, 10348-10352.
132. Eskandarloo, H.; Arshadi, M.; Enayati, M.; Abbaspourrad, A., Highly efficient recovery of heparin using a green and low-cost quaternary ammonium functionalized halloysite nanotube. *ACS Sustain. Chem. Eng.* 2018**,** *6* (11), 15349-15360.
133. Li, H.; Zhu, X. H.; Xu, J. F.; Peng, W.; Zhong, S. A.; Wang, Y., The combination of adsorption by functionalized halloysite nanotubes and encapsulation by polyelectrolyte coatings for sustained drug delivery. *RSC Adv.* 2016**,** *6* (59), 54463-54470.
134. Lisuzzo, L.; Cavallaro, G.; Milioto, S.; Lazzara, G., Halloysite nanotubes coated by chitosan for the controlled release of khellin. *Polymers* 2020**,** *12* (8), 15.
135. Rouster, P.; Pavlovic, M.; Horvath, E.; Forro, L.; Dey, S. K.; Szilagyi, I., Influence of protamine functionalization on the colloidal stability of 1D and 2D titanium oxide nanostructures. *Langmuir* 2017**,** *33* (38), 9750-9758.
136. Rouster, P.; Pavlovic, M.; Szilagyi, I., Improving the stability of titania nanosheets by functionalization with polyelectrolytes. *RSC Adv.* 2016**,** *6* (99), 97322-97330.
137. Rogers, R. D.; Seddon, K. R., Ionic liquids - Solvents of the future? *Science* 2003**,** *302* (5646), 792-793.
138. Earle, M. J.; Esperanca, J.; Gilea, M. A.; Lopes, J. N. C.; Rebelo, L. P. N.; Magee, J. W.; Seddon, K. R.; Widegren, J. A., The distillation and volatility of ionic liquids. *Nature* 2006**,** *439* (7078), 831-834.
139. Wasserscheid, P., Chemistry - Volatile times for ionic liquids. *Nature* 2006**,** *439* (7078), 797-797.
140. Zheng, Z. P.; Fan, W. H.; Roy, S.; Mazur, K.; Nazet, A.; Buchner, R.; Bonn, M.; Hunger, J., Ionic liquids: Not only structurally but also dynamically heterogeneous. *Angew. Chem.-Int. Edit.* 2015**,** *54* (2), 687-690.
141. Dozic, S.; Zec, N.; Tot, A.; Papovic, S.; Pavlovic, K.; Gadzuric, S.; Vranes, M., Does the variation of the alkyl chain length on N1 and N3 of imidazole ring affect physicochemical features of ionic liquids in the same way? *J. Chem. Thermodyn.* 2016**,** *93*, 52-59.
142. Wilkes, J. S., A short history of ionic liquids - from molten salts to neoteric solvents. *Green Chem.* 2002**,** *4* (2), 73-80.
143. Endres, F., Ionic liquids: Solvents for the electrodeposition of metals and semiconductors. *ChemPhysChem* 2002**,** *3* (2), 144-154.
144. Armand, M.; Endres, F.; MacFarlane, D. R.; Ohno, H.; Scrosati, B., Ionic-liquid materials for the electrochemical challenges of the future. *Nat. Mater.* 2009**,** *8* (8), 621-629.
145. Dzyuba, S. V.; Bartsch, R. A., Influence of structural variations in 1-alkyl(aralkyl)-3-methylimidazolium hexafluorophosphates and bis(trifluorormethyl-sulfonyl)imides on physical properties of the ionic liquids. *ChemPhysChem* 2002**,** *3* (2), 161-166.
146. Kaur, G.; Kumar, H.; Singla, M., Diverse applications of ionic liquids: A comprehensive review. *J. Mol. Liq.* 2022**,** *351*, 19.
147. Pei, Y. C.; Zhang, Y. X.; Ma, J.; Fan, M. H.; Zhang, S. J.; Wang, J. J., Ionic liquids

for advanced materials. *Mater. Today Nano* 2022**,** *17*, 23.
148. Hayes, R.; Warr, G. G.; Atkin, R., Structure and nanostructure in ionic liquids. *Chem. Rev.* 2015**,** *115* (13), 6357-6426.
149. Tunckol, M.; Durand, J.; Serp, P., Carbon nanomaterial-ionic liquid hybrids. *Carbon* 2012**,** *50* (12), 4303-4334.
150. Minea, M. A.; Murshed, S. M. S., Ionic liquids-based nanocolloids-A review of progress and prospects in convective heat transfer applications. *Nanomaterials* 2021**,** *11* (4), 1039.
151. Ji, Q. M.; Acharya, S.; Richards, G. J.; Zhang, S. L.; Vieaud, J.; Hill, J. P.; Ariga, K., Alkyl Imidazolium Ionic-Liquid-Mediated Formation of Gold Particle Superstructures. *Langmuir* 2013**,** *29* (24), 7186-7194.
152. Guibert, C.; Dupuis, V.; Fresnais, J.; Peyre, V., Controlling nanoparticles dispersion in ionic liquids by tuning the pH. *J. Colloid Interface Sci.* 2015**,** *454*, 105-111.
153. Smith, J. A.; Werzer, O.; Webber, G. B.; Warr, G. G.; Atkin, R., Surprising particle stability and rapid sedimentation rates in an ionic liquid. *J. Phys. Chem. Lett.* 2010**,** *1* (1), 64-68.
154. Szilagyi, I.; Szabo, T.; Desert, A.; Trefalt, G.; Oncsik, T.; Borkovec, M., Particle aggregation mechanisms in ionic liquids. *Phys. Chem. Chem. Phys.* 2014**,** *16* (20), 9515-9524.
155. Ueno, K.; Inaba, A.; Kondoh, M.; Watanabe, M., Colloidal stability of bare and polymer-grafted silica nanoparticles in ionic liquids. *Langmuir* 2008**,** *24* (10), 5253-5259.
156. Nordstrom, J.; Aguilera, L.; Matic, A., Effect of lithium salt on the stability of dispersions of fumed silica in the ionic liquid $BMImBF_4$. *Langmuir* 2012**,** *28* (9), 4080-4085.
157. Mamusa, M.; Siriex-Plenet, J.; Cousin, F.; Dubois, E.; Peyrea, V., Tuning the colloidal stability in ionic liquids by controlling the nanoparticles/liquid interface. *Soft Matter* 2014**,** *10*, 1097-1101.
158. Vanecht, E.; Binnemans, K.; Patskovsky, S.; Meunier, M.; Seo, J. W.; Stappers, L.; Fransaer, J., Stability of sputter-deposited gold nanoparticles in imidazolium ionic liquids. *Phys. Chem. Chem. Phys.* 2012**,** *14* (16), 5662-5671.
159. He, Z. Q.; Alexandridis, P., Nanoparticles in ionic liquids: interactions and organization. *Phys. Chem. Chem. Phys.* 2015**,** *17* (28), 18238-18261.
160. Luczak, J.; Paszkiewicz, M.; Krukowska, A.; Malankowska, A.; Zaleska-Medynska, A., Ionic liquids for nano- and microstructures preparation. Part 1: Properties and multifunctional role. *Adv. Colloid Interface Sci.* 2016**,** *230*, 13-28.
161. Ueno, K.; Watanabe, M., From colloidal stability in ionic liquids to advanced soft materials using unique media. *Langmuir* 2011**,** *27* (15), 9105-9115.
162. Vollmer, C.; Janiak, C., Naked metal nanoparticles from metal carbonyls in ionic liquids: Easy synthesis and stabilization. *Coord. Chem. Rev.* 2011**,** *255* (17-18), 2039-2057.
163. Arquilliere, P. P.; Helgadottir, I. S.; Santini, C. C.; Haumesser, P. H.; Aouine, M.; Massin, L.; Rousset, J. L., Bimetallic Ru-Cu nanoparticles synthesized in ionic liquids: Kinetically controlled size and structure. *Top. Catal.* 2013**,** *56* (13-14), 1192-1198.
164. Zhang, H.; Dasbiswas, K.; Ludwig, N. B.; Han, G.; Lee, B.; Vaikuntanathan, S.; Talapin, D. V., Stable colloids in molten inorganic salts. *Nature* 2017**,** *542* (7641), 328-331.
165. Yang, X.; Fei, Z. F.; Zhao, D. B.; Ang, W. H.; Li, Y. D.; Dyson, P. J., Palladium nanoparticles stabilized by an ionic polymer and ionic liquid: A versatile system for C-C cross-coupling reactions. *Inorg. Chem.* 2008**,** *47* (8), 3292-3297.
166. Gopakumar, A.; Fei, Z. F.; Paunescu, E.; Auzelyte, V.; Brugger, J.; Dyson, P. J., UV-imprint resists generated from polymerizable ionic liquids and titania nanoparticles. *J. Phys. Chem. C* 2014**,** *118* (30), 16743-16748.
167. Zhou, Y.; Antonietti, M., Synthesis of very small TiO_2 nanocrystals in a room-temperature ionic liquid and their self-assembly toward mesoporous spherical aggregates. *J. Am. Chem. Soc.* 2003**,** *125* (49), 14960-14961.

168. Kanzaki, R.; Guibert, C.; Fresnais, J.; Peyre, V., Dispersion mechanism of polyacrylic acid-coated nanoparticle in protic ionic liquid, N,N-diethylethanolammonium trifluoromethanesulfonate. *J. Colloid Interface Sci.* 2018**,** *516*, 248-253.
169. Podgorsek, A.; Pensado, A. S.; Santini, C. C.; Gomes, M. F. C.; Padua, A. A. H., Interaction energies of ionic liquids with metallic nanoparticles: Solvation and stabilization effects. *J. Phys. Chem. C* 2013**,** *117* (7), 3537-3547.
170. Smith, J.; Webber, G. B.; Warr, G. G.; Atkin, R., Silica particle stability and settling in protic ionic liquids. *Langmuir* 2014**,** *40* (6), 1506-1513.
171. Wittmar, A.; Ruiz-Abad, D.; Ulbricht, M., Dispersions of silica nanoparticles in ionic liquids investigated with advanced rheology. *J. Nanopart. Res.* 2012**,** *14* (2), 65101-65110.
172. Gao, J. S.; Ndong, R. S.; Shiflett, M. B.; Wagner, N. J., Creating nanoparticle stability in ionic liquid [C_4mim][BF_4] by inducing solvation layering. *ACS Nano* 2015**,** *9* (3), 3243-3253.
173. Mezger, M.; Schroder, H.; Reichert, H.; Schramm, S.; Okasinski, J. S.; Schoder, S.; Honkimaki, V.; Deutsch, M.; Ocko, B. M.; Ralston, J.; Rohwerder, M.; Stratmann, M.; Dosch, H., Molecular layering of fluorinated ionic liquids at a charged sapphire (0001) surface. *Science* 2008**,** *322* (5900), 424-428.
174. Sheehan, A.; Jurado, L. A.; Ramakrishna, S. N.; Arcifa, A.; Rossi, A.; Spencer, N. D.; Espinosa-Marzal, R. M., Layering of ionic liquids on rough surfaces. *Nanoscale* 2016**,** *8* (7), 4094-4106.
175. Gebbie, M. A.; Valtiner, M.; Banquy, X.; Fox, E. T.; Henderson, W. A.; Israelachvili, J. N., Ionic liquids behave as dilute electrolyte solutions. *Proc. Natl. Acad. Sci. U. S. A.* 2013**,** *110* (24), 9674-9679.
176. Derjaguin, B.; Landau, L., Theory of the stability of strongly charged lyophobic sols and of the adhesion of strongly charged particles in solutions of electrolytes. *Prog. Surf. Sci.* 1993**,** *43* (1-4), 30-59.
177. Derjaguin, B., On the repulsive forces between charged colloid particles and on the theory of slow coagulation and stability of lyophobe sols. *Trans. Faraday Soc.* 1940**,** *35* (3), 0203-0214.
178. Gebbie, M. A.; Smith, A. M.; Dobbs, H. A.; Lee, A. A.; Warr, G. G.; Banquy, X.; Valtiner, M.; Rutland, M. W.; Israelachvili, J. N.; Perkin, S.; Atkin, R., Long range electrostatic forces in ionic liquids. *Chem. Commun.* 2017**,** *53* (7), 1214-1224.
179. Oncsik, T.; Desert, A.; Trefalt, G.; Borkovec, M.; Szilagyi, I., Charging and aggregation of latex particles in aqueous solutions of ionic liquids: Towards an extended Hofmeister series. *Phys. Chem. Chem. Phys.* 2016**,** *18* (10), 7511-7520.
180. Elmahdy, M. M.; Gutsche, C.; Kremer, F., Forces within single pairs of charged colloids in aqueous solutions of ionic liquids as studied by optical tweezers. *J. Phys. Chem. C* 2010**,** *114* (45), 19452-19458.
181. Valmacco, V.; Trefalt, G.; Maroni, P.; Borkovec, M., Direct force measurements between silica particles in aqueous solutions of ionic liquids containing 1-butyl-3-methylimidazolium (BMIM). *Phys. Chem. Chem. Phys.* 2015**,** *17*, 16553-16559.
182. Tietze, A. A.; Bordusa, F.; Giernoth, R.; Imhof, D.; Lenzer, T.; Maass, A.; Mrestani-Klaus, C.; Neundorf, I.; Oum, K.; Reith, D.; Stark, A., On the nature of interactions between ionic liquids and small amino-acid-based biomolecules. *ChemPhysChem* 2013**,** *14* (18), 4044-4064.
183. Yang, Z., Hofmeister effects: an explanation for the impact of ionic liquids on biocatalysis. *J. Biotechnol.* 2009**,** *144* (1), 12-22.
184. Yang, Y. J.; Yaakob, S. M.; Rabat, N. E.; Shamsuddin, M. R.; Man, Z., Release kinetics study and anti-corrosion behaviour of a pH-responsive ionic liquid-loaded halloysite nanotube-doped epoxy coating. *RSC Adv.* 2020**,** *10* (22), 13174-13184.
185. Li, H.; Feng, Z. Q.; Zhao, K.; Wang, Z. H.; Liu, J. H.; Liu, J.; Song, H. Z., Chemically

crosslinked liquid crystalline poly(ionic liquid)s/halloysite nanotubes nanocomposite ionogels with superior ionic conductivity, high anisotropic conductivity and a high modulus. *Nanoscale* 2019**,** *11* (8), 3689-3700.
186. Brondani, D.; Scheeren, C. W.; Dupont, J.; Vieira, I. C., Halloysite clay nanotubes and platinum nanoparticles dispersed in ionic liquid applied in the development of a catecholamine biosensor. *Analyst* 2012**,** *137* (16), 3732-3739.
187. Guo, S. F.; Zhao, K.; Feng, Z. Q.; Hou, Y. D.; Li, H.; Zhao, J.; Tian, Y. L.; Song, H. Z., High performance liquid crystalline bionanocomposite ionogels prepared by in situ crosslinking of cellulose/halloysite nanotubes/ionic liquid dispersions and its application in supercapacitors. *Appl. Surf. Sci.* 2018**,** *455*, 599-607.
188. Nimse, S. B.; Pal, D., Free radicals, natural antioxidants, and their reaction mechanisms. *RSC Adv.* 2015**,** *5* (35), 27986-28006.
189. Valko, M.; Rhodes, C. J.; Moncol, J.; Izakovic, M.; Mazur, M., Free radicals, metals and antioxidants in oxidative stress-induced cancer. *Chem.-Biol. Interact.* 2006**,** *160* (1), 1-40.
190. Sies, H., Oxidative stress: Oxidants and antioxidants. *Exp. Physiol.* 1997**,** *82* (2), 291-295.
191. Birben, E.; Sahiner, U. M.; Sackesen, C.; Erzurum, S.; Kalayci, O., Oxidative stress and antioxidant defense. *WAO J.* 2012**,** *5* (1), 9-19.
192. Sharma, V.; Collins, L. B.; Chen, T. H.; Herr, N.; Takeda, S.; Sun, W.; Swenberg, J. A.; Nakamura, J., Oxidative stress at low levels can induce clustered DNA lesions leading to NHEJ mediated mutations. *Oncotarget* 2016**,** *7* (18), 25377-25390.
193. Jenner, P., Oxidative stress in Parkinson's disease. *Ann. Neurol.* 2003**,** *53*, S26-S36.
194. Brieger, K.; Schiavone, S.; Miller, F. J.; Krause, K. H., Reactive oxygen species: from health to disease. *Swiss Med. Wkly.* 2012**,** *142*, 13659.
195. McCord, J. M.; Fridovic, I., Superoxide dismutase - An enzymic function for erythrocuprein (hemocuprein). *J. Biol. Chem.* 1969**,** *244* (22), 6049-6055.
196. Storz, G.; Tartaglia, L. A.; Ames, B. N., Transcriptional regulator of oxidative stress-inducible genes - Direct activation by oxidation. *Science* 1990**,** *248* (4952), 189-194.
197. Wang, L. Y.; Zhu, B. H.; Deng, Y. T.; Li, T. T.; Tian, Q. Y.; Yuan, Z. G.; Ma, L.; Cheng, C.; Guo, Q. Y.; Qiu, L., Biocatalytic and antioxidant nanostructures for ROS scavenging and biotherapeutics. *Adv. Funct. Mater.* 2021**,** *31* (31), 2101804.
198. Alfadda, A. A.; Sallam, R. M., Reactive oxygen species in health and disease. *J. Biomed. Biotechnol.* 2012**,** *2012*, 936486.
199. Winterbourn, C. C., Reconciling the chemistry and biology of reactive oxygen species. *Nat. Chem. Biol.* 2008**,** *4* (5), 278-286.
200. Bugg, T., *Introduction to enzyme and coenzyme chemistry*. Blackwell Publishing Ltd: Oxford, 2004.
201. Meghwanshi, G. K.; Kaur, N.; Verma, S.; Dabi, N. K.; Vashishtha, A.; Charan, P. D.; Purohit, P.; Bhandari, H. S.; Bhojak, N.; Kumar, R., Enzymes for pharmaceutical and therapeutic applications. *Biotechnol. Appl. Biochem.* 2020**,** *67* (4), 586-601.
202. Galante, Y. A.; Formantici, C., Enzyme applications in detergency and in manufacturing industries. *Curr. Org. Chem.* 2003**,** *7* (13), 1399-1422.
203. Bajpai, P., Application of enzymes in the pulp and paper industry. *Biotechnol. Prog.* 1999**,** *15* (2), 147-157.
204. Daniel, R. M.; Dines, M.; Petach, H. H., The denaturation and degradation of stable enzymes at high temperatures. *Biochem. J.* 1996**,** *317*, 1-11.
205. Datta, S.; Christena, L. R.; Rajaram, Y. R. S., Enzyme immobilization: an overview on techniques and support materials. *3 Biotech* 2013**,** *3* (1), 1-9.
206. Tsekhmistrenko, S. I.; Bityutskyy, V. S.; Tsekhmistrenko, O. S.; Polishchuk, V. M.; Polishchuk, S. A.; Ponomarenko, N. V.; Melnychenko, Y. O.; Spivak, M. Y., Enzyme-like

activity of nanomaterials. *Regul. Mech. Biosyst.* 2018**,** *9* (3), 469-476.
207. Wei, H.; Wang, E. K., Nanomaterials with enzyme-like characteristics (nanozymes): next-generation artificial enzymes. *Chem. Soc. Rev.* 2013**,** *42* (14), 6060-6093.
208. Ighodaro, O. M.; Akinloye, O. A., First line defence antioxidants-superoxide dismutase (SOD), catalase (CAT) and glutathione peroxidase (GPX): Their fundamental role in the entire antioxidant defence grid. *Alex. J. Med.* 2018**,** *54* (4), 287-293.
209. El-Missiry, M. A., *Antioxidant enzyme*. InTech: Rijeka, 2012.
210. Bouayed, J.; Bohn, T., Exogenous antioxidants-Double-edged swords in cellular redox state. *Oxidative Med. Cell. Longev.* 2010**,** *3* (4), 228-237.
211. Maehly, A. C.; Chance, B., The assay of catalases and peroxidases. *Methods Biochem. Anal.* 1954**,** *1*, 357-424.
212. Tainer, J. A.; Getzoff, E. D.; Richardson, J. S.; Richardson, D. C., Structure and mechanism of copper, zinc superoxide-dismutase. *Nature* 1983**,** *306* (5940), 284-287.
213. Bafana, A.; Dutt, S.; Kumar, S.; Ahuja, P. S., Superoxide dismutase: an industrial perspective. *Crit. Rev. Biotechnol.* 2011**,** *31* (1), 65-76.
214. Zelko, I. N.; Mariani, T. J.; Folz, R. J., Superoxide dismutase multigene family: A comparison of the CuZn-SOD (SOD1), Mn-SOD (SOD2), and EC-SOD (SOD3) gene structures, evolution, and expression. *Free Radic. Biol. Med.* 2002**,** *33* (3), 337-349.
215. Kubota, R.; Asayama, S.; Kawakami, H., Catalytic antioxidants for therapeutic medicine. *J. Mat. Chem. B* 2019**,** *7* (20), 3165-3191.
216. Yan, F.; Mu, Y.; Yan, G. L.; Liu, J. Q.; Shen, J. C.; Luo, G. M., Antioxidant enzyme mimics with synergism. *Mini-Rev. Med. Chem.* 2010**,** *10* (4), 342-356.
217. Kuah, E.; Toh, S.; Yee, J.; Ma, Q.; Gao, Z. Q., Enzyme mimics: Advances and applications. *Chem.-Eur. J.* 2016**,** *22* (25), 8404-8430.
218. Alsharif, N. B.; Samu, G. F.; Sáringer, S.; Muráth, S.; Szilagyi, I., A colloid approach to decorate latex particles with Prussian blue nanozymes. *J. Mol. Liq.* 2020**,** *309*, 113066.
219. Chen, T. M.; Zou, H.; Wu, X. J.; Liu, C. C.; Situ, B.; Zheng, L.; Yang, G. W., Nanozymatic antioxidant system based on MoS_2 nanosheets. *ACS Appl. Mater. Interfaces* 2018**,** *10* (15), 12453-12462.
220. Valgimigli, L.; Baschieri, A.; Amorati, R., Antioxidant activity of nanomaterials. *J. Mat. Chem. B* 2018**,** *6* (14), 2036-2051.
221. Gao, N.; Dong, K.; Zhao, A. D.; Sun, H. J.; Wang, Y.; Ren, J. S.; Qu, X. G., Polyoxometalate-based nanozyme: Design of a multifunctional enzyme for multi-faceted treatment of Alzheimer's disease. *Nano Res.* 2016**,** *9* (4), 1079-1090.
222. Singh, N.; Savanur, M. A.; Srivastava, S.; D'Silva, P.; Mugesh, G., A redox modulatory Mn_3O_4 nanozyme with multi-enzyme activity provides efficient cytoprotection to human cells in a Parkinson's disease model. *Angew. Chem.-Int. Edit.* 2017**,** *56* (45), 14267-14271.
223. Henke, S. L., Superoxide dismutase mimics as future therapeutics. *Expert Opin. Ther. Patents* 1999**,** *9* (2), 169-180.
224. Alsharif, N. B.; Bere, K.; Sáringer, S.; Samu, G. F.; Takács, D.; Hornok, V.; Szilagyi, I., Design of hybrid biocatalysts by controlled heteroaggregation of manganese oxide and sulfate latex particles to combat reactive oxygen species. *J. Mat. Chem. B* 2021**,** *9* (24), 4929-4940.
225. Othman, A.; Norton, L.; Finny, A. S.; Andreescu, S., Easy-to-use and inexpensive sensors for assessing the quality and traceability of cosmetic antioxidants. *Talanta* 2020**,** *208*, 120473.
226. Lin, Y. H.; Ren, J. S.; Qu, X. G., Catalytically active nanomaterials: A promising candidate for artificial enzymes. *Accounts Chem. Res.* 2014**,** *47* (4), 1097-1105.
227. Moglianetti, M.; De Luca, E.; Deborah, P. A.; Marotta, R.; Catelani, T.; Sartori, B.; Amenitsch, H.; Retta, S. F.; Pompa, P. P., Platinum nanozymes recover cellular ROS

homeostasis in an oxidative stress-mediated disease model. *Nanoscale* 2016**,** *8* (6), 3739-3752.
228. Zhang, W.; Hu, S. L.; Yin, J. J.; He, W. W.; Lu, W.; Ma, M.; Gu, N.; Zhang, Y., Prussian Blue nanoparticles as multienzyme mimetics and reactive oxygen species scavengers. *J. Am. Chem. Soc.* 2016**,** *138* (18), 5860-5865.
229. Dong, J. L.; Song, L. N.; Yin, J. J.; He, W. W.; Wu, Y. H.; Gu, N.; Zhang, Y., Co_3O_4 nanoparticles with multi-enzyme activities and their application in immunohistochemical assay. *ACS Appl. Mater. Interfaces* 2014**,** *6* (3), 1959-1970.
230. Tonga, G. Y.; Jeong, Y. D.; Duncan, B.; Mizuhara, T.; Mout, R.; Das, R.; Kim, S. T.; Yeh, Y. C.; Yan, B.; Hou, S.; Rotello, V. M., Supramolecular regulation of bioorthogonal catalysis in cells using nanoparticle-embedded transition metal catalysts. *Nat. Chem.* 2015**,** *7* (7), 597-603.
231. Kirkorian, K.; Ellis, A.; Twyman, L. J., Catalytic hyperbranched polymers as enzyme mimics; exploiting the principles of encapsulation and supramolecular chemistry. *Chem. Soc. Rev.* 2012**,** *41* (18), 6138-6159.
232. Siqueira, J. D.; de Pellegrin, S. F.; dos Santos, S. S.; Iglesias, B. A.; Piquini, P. C.; Arantes, L. P.; Soares, F. A.; Chaves, O. A.; Neves, A.; Back, D. F., SOD activity of new copper II complexes with ligands derived from pyridoxal and toxicity in Caenorhabditis elegans. *J. Inorg. Biochem.* 2020**,** *204*, 15.
233. Labádi, I.; Benko, M.; Kata, M.; Szilagyi, I., Mimicking a Superoxide Dismutase (SOD) Enzyme by copper(II) and zinc(II)-complexes. *React. Kinet. Catal. Lett.* 2009**,** *96* (2), 327-333.
234. Holm, R. H.; Kennepohl, P.; Solomon, E. I., Structural and functional aspects of metal sites in biology. *Chem. Rev.* 1996**,** *96* (7), 2239-2314.
235. Szilagyi, I.; Labadi, I.; Hernadi, K.; Palinko, I.; Fekete, I.; Korecz, L.; Rockenbauer, A.; Kiss, T., Superoxide dismutase activity of a Cu-Zn complex - bare and immobilised. *New J. Chem.* 2005**,** *29* (5), 740-745.
236. Labadi, I.; Szilagyi, I.; Jakab, N. I.; Hernadi, K.; Palinko, I., Metal complexes immobilised in/on porous matrices - possible enzyme mimics. *Mater. Sci.* 2003**,** *21* (2), 235-244.
237. Szilagyi, I.; Labadi, I.; Hernadi, K.; Kiss, T.; Palinko, I., Montmorillonite intercalated Cu(II)-histidine complex - synthesis, characterisation and superoxide dismutase activity. In *Molecular Sieves: From Basic Research to Industrial Applications, Pts a and B*, Cejka, J.; Zilkova, N.; Nachtigall, P., Eds. 2005; Vol. 158, pp 1011-1018.
238. Szilagyi, I.; Nagy, G.; Hernadi, K.; Labadi, I.; Palinko, I., Modeling copper-containing enzyme mimics. *J. Mol. Struct. THEOCHEM* 2003**,** *666-667*.
239. Vazquez-Gonzalez, M.; Liao, W. C.; Gazelles, R.; Wang, S.; Yu, X.; Gutkin, V.; Willner, I., Mimicking horseradish peroxidase functions using Cu^{2+}-modified carbon nitride nanoparticles or Cu^{2+}-modified carbon dots as heterogeneous catalysts. *ACS Nano* 2017**,** *11* (3), 3247-3253.
240. Pratsinis, A.; Kelesidis, G. A.; Zuercher, S.; Krumeich, F.; Bolisetty, S.; Mezzenga, R.; Leroux, J. C.; Sotiriou, G. A., Enzyme-mimetic antioxidant luminescent nanoparticles for highly sensitive hydrogen peroxide biosensing. *ACS Nano* 2017**,** *11* (12), 12210-12218.
241. Breslow, R., Biomimetic selectivity. *Chem. Rec.* 2001**,** *1* (1), 3-11.
242. Belle, C.; Pierre, J. L., Asymmetry in bridged binuclear metalloenzymes: Lessons for the chemist. *Eur. J. Inorg. Chem.* 2003**,** *2003* (23), 4137-4146.
243. Wu, A. J.; Penner-Hahn, J. E.; Pecoraro, V. L., Structural, spectroscopic, and reactivity models for the manganese catalases. *Chem. Rev.* 2004**,** *104* (2), 903-938.
244. DiCosimo, R.; McAuliffe, J.; Poulose, A. J.; Bohlmann, G., Industrial use of immobilized enzymes. *Chem. Soc. Rev.* 2013**,** *42* (15), 6437-6474.
245. Cipolatti, E. P.; Valerio, A.; Henriques, R. O.; Moritz, D. E.; Ninow, J. L.; Freire, D.

M. G.; Manoel, E. A.; Fernandez-Lafuente, R.; de Oliveira, D., Nanomaterials for biocatalyst immobilization - state of the art and future trends. *RSC Adv.* 2016**,** *6* (106), 104675-104692.
246. Tikhonov, B. B.; Sulman, E. M.; Stadol'nikova, P. Y.; Sulman, A. M.; Golikova, E. P.; Sidorov, A. I.; Matveeva, V. G., Immobilized enzymes from the class of oxidoreductases in technological processes: A review. *Catal. Ind.* 2019**,** *11* (3), 251-263.
247. Jesionowski, T.; Zdarta, J.; Krajewska, B., Enzyme immobilization by adsorption: a review. *Adsorpt.-J. Int. Adsorpt. Soc.* 2014**,** *20* (5-6), 801-821.
248. Bilal, M.; Asgher, M.; Cheng, H. R.; Yan, Y. J.; Iqbal, H. M. N., Multi-point enzyme immobilization, surface chemistry, and novel platforms: a paradigm shift in biocatalyst design. *Crit. Rev. Biotechnol.* 2019**,** *39* (2), 202-219.
249. Price, R. R.; Gaber, B. P.; Lvov, Y., In-vitro release characteristics of tetracycline HCl, khellin and nicotinamide adenine dineculeotide from halloysite; a cylindrical mineral. *J. Microencapsul.* 2001**,** *18* (6), 713-722.
250. Copeland, R. A., *Enzymes - A practical introduction to structure, mechanism, and data analysis*. Wiley-VCH Inc: New York, 2000.
251. Fan, X. T.; Hu, M. C.; Li, S. N.; Zhai, Q. G.; Wang, F.; Jiang, Y. C., Charge controlled immobilization of chloroperoxidase on both inner/outer wall of NHT: Improved stability and catalytic performance in the degradation of pesticide. *Appl. Clay Sci.* 2018**,** *163*, 92-99.
252. Chao, C.; Liu, J. D.; Wang, J. T.; Zhang, Y. W.; Zhang, B.; Zhang, Y. T.; Xiang, X.; Chen, R. F., Surface modification of halloysite nanotubes with dopamine for enzyme immobilization. *ACS Appl. Mater. Interfaces* 2013**,** *5* (21), 10559-10564.
253. Tully, J.; Yendluri, R.; Lvov, Y., Halloysite clay nanotubes for enzyme immobilization. *Biomacromolecules* 2016**,** *17* (2), 615-621.
254. Kumar-Krishnan, S.; Hernandez-Rangel, A.; Pal, U.; Ceballos-Sanchez, O.; Flores-Ruiz, F. J.; Prokhorov, E.; de Fuentes, O. A.; Esparza, R.; Meyyappan, M., Surface functionalized halloysite nanotubes decorated with silver nanoparticles for enzyme immobilization and biosensing. *J. Mat. Chem. B* 2016**,** *4* (15), 2553-2560.
255. Li, Y.; Yuan, X. Z.; Jiang, L. B.; Dai, H.; Zhao, Y. L.; Guan, X.; Bai, J.; Wang, H., Manipulation of the halloysite clay nanotube lumen for environmental remediation: a review. *Environ. Sci.-Nano* 2022**,** *9* (3), 841-866.
256. Cavallaro, G.; Milioto, S.; Svetlana, K.; Fakhrullina, G.; Akhatova, F.; Lazzara, G.; Fakhrullin, R.; Lvov, Y., Halloysite/keratin nanocomposite for human hair photoprotection coating. *ACS Appl. Mater. Interfaces* 2020**,** *12* (21), 24348-24362.
257. Alsafadi, D.; Paradisi, F., Covalent immobilization of alcohol dehydrogenase (ADH2) from haloferax volcanii: How to maximize activity and optimize performance of halophilic enzymes. *Mol. Biotechnol.* 2014**,** *56* (3), 240-247.
258. Ren, H.; Zhang, Y. H.; Su, J. R.; Lin, P.; Wang, B.; Fang, B. S.; Wang, S. Z., Encapsulation of amine dehydrogenase in hybrid titania nanoparticles by polyethylenimine coating and templated biomineralization. *J. Biotechnol.* 2017**,** *241*, 33-41.
259. Zhu, X.; Niu, X. H.; Zhao, H. L.; Tang, J.; Lan, M. B., Immobilization of superoxide dismutase on Pt-Pd/MWCNTs hybrid modified electrode surface for superoxide anion detection. *Biosens. Bioelectron.* 2015**,** *67*, 79-85.
260. Pavlovic, M.; Rouster, P.; Szilagyi, I., Synthesis and formulation of functional bionanomaterials with superoxide dismutase activity. *Nanoscale* 2017**,** *9* (1), 369-379.
261. Rouster, P.; Pavlovic, M.; Szilagyi, I., Immobilization of Superoxide Dismutase on polyelectrolyte functionalized titania nanosheets. *ChemBiochem* 2018**,** *19* (4), 404-410.
262. Li, Z.; Wang, F.; Roy, S.; Sen, C. K.; Guan, J. J., Injectable, highly flexible, and thermosensitive hydrogels capable of delivering superoxide dismutase. *Biomacromolecules* 2009**,** *10* (12), 3306-3316.
263. Chen, Y. P.; Chen, C. T.; Hung, Y.; Chou, C. M.; Liu, T. P.; Liang, M. R.; Mou, C.

Y., A new strategy for intracellular delivery of enzyme using mesoporous silica nanoparticles: Superoxide Dismutase. *J. Am. Chem. Soc.* 2013**,** *135* (4), 1516-1523.
264. Bobone, S.; Miele, E.; Cerroni, B.; Roversi, D.; Bocedi, A.; Nicolai, E.; Di Venere, A.; Placidi, E.; Ricci, G.; Rosato, N.; Stella, L., Liposome-templated hydrogel nanoparticles as vehicles for enzyme-based therapies. *Langmuir* 2015**,** *31* (27), 7572-7580.
265. Singh, S.; Dubey, V. K., Multiwalled carbon nanotube-superoxide dismutase conjugate towards alleviating induced oxidative stress. *Int. J. Pept. Res. Ther.* 2016**,** *22* (2), 171-177.
266. Fang, Y. C.; Chen, Y. P.; Chen, C. T.; Lin, T. S.; Mou, C. Y., Protection of HeLa cells against ROS stress by CuZnSOD mimic system. *J. Mat. Chem. B* 2013**,** *1* (44), 6042-6052.
267. Yang, M.; Jiang, W.; Pan, Z. Q.; Zhou, H., Synthesis, characterization and SOD-like activity of histidine immobilized silica nanoparticles. *J. Inorg. Organomet. Polym. Mater.* 2015**,** *25* (5), 1289-1297.
268. Szilagyi, I.; Berkesi, O.; Sipiczki, M.; Korecz, L.; Rockenbauer, A.; Palinko, I., Preparation, characterization and catalytic activities of immobilized enzyme mimics. *Catal. Lett.* 2009**,** *127* (3-4), 239-247.
269. Pavlovic, M.; Nafradi, M.; Rouster, P.; Murath, S.; Szilagyi, I., Highly stable enzyme-mimicking nanocomposite of antioxidant activity. *J. Colloid Interface Sci.* 2019**,** *543*, 174-182.
270. Somosi, Z.; May, N. V.; Sebok, D.; Palinko, I.; Szilagyi, I., Catalytic antioxidant nanocomposites based on sequential adsorption of redox active metal complexes and polyelectrolytes on nanoclay particles. *Dalton Trans.* 2021**,** *50* (7), 2426-2435.
271. Zhong, W.; Bobbink, F. D.; Fei, Z. F.; Dyson, P. J., Polyimidazolium salts: Robust catalysts for the cycloaddition of carbon dioxide into carbonates in solvent-free conditions. *ChemSusChem* 2017**,** *10* (13), 2728-2735.
272. O'Brien, R. W.; White, L. R., Electrophoretic mobility of a spherical colloidal particle. *J. Chem. Soc.-Faraday Trans.* 1978**,** *74*, 1607-1626.
273. Deshiikan, S. R.; Papadopoulos, K. D., Modified Booth equation for the calculation of zeta potential. *Colloid Polym. Sci.* 1998**,** *276* (2), 117-124.
274. Horvath, E.; Grebikova, L.; Maroni, P.; Szabo, T.; Magrez, A.; Forro, L.; Szilagyi, I., Dispersion characteristics and aggregation in titanate nanowire colloids. *ChemPlusChem* 2014**,** *79* (4), 592-600.
275. Hassan, P. A.; Rana, S.; Verma, G., Making sense of Brownian motion: Colloid characterization by dynamic light scattering. *Langmuir* 2015**,** *31* (1), 3-12.
276. Pusey, P. N., Dynamic light scattering. In *Neutrons, X-Rays and Light*, Lindner, P.; Zemb, T., Eds. Elsevier Science B.V.: Amsterdam, 2002; pp 203-220.
277. Berne, B. J.; Pecora, R., *Dynamic light scattering*. Robert E. Krieger Publishing: Malabar, 1990.
278. Holmberg, K., *Handbook of Applied Surface and Colloid Chemistry, Vol. 2*. John Wiley: New York, 2002.
279. Holthoff, H.; Egelhaaf, S. U.; Borkovec, M.; Schurtenberger, P.; Sticher, H., Coagulation rate measurements of colloidal particles by simultaneous static and dynamic light scattering. *Langmuir* 1996**,** *12* (23), 5541-5549.
280. Berka, M.; Rice, J. A., Absolute aggregation rate constants in aggregation of kaolinite measured by simultaneous static and dynamic light scattering. *Langmuir* 2004**,** *20* (15), 6152-6157.
281. Schneider, C.; Hanisch, M.; Wedel, B.; Jusufi, A.; Ballauff, M., Experimental study of electrostatically stabilized colloidal particles: Colloidal stability and charge reversal. *J. Colloid Interface Sci.* 2011**,** *358* (1), 62-67.
282. Pusey, P. N., Introduction to Scattering Experiments. In *Neutrons, X-Rays and Light*, Lindner, P.; Zemb, T., Eds. Elsevier Science B.V.: Amsterdam, 2002; pp 3-21.
283. Meng, Z. Y.; Hashmi, S. M.; Elimelech, M., Aggregation rate and fractal dimension of

fullerene nanoparticles via simultaneous multiangle static and dynamic light scattering measurement. *J. Colloid Interface Sci.* 2013**,** *392*, 27-33.
284. Owczarz, M.; Motta, A. C.; Morbidelli, M.; Arosio, P., A Colloidal Description of Intermolecular Interactions Driving Fibril-Fibril Aggregation of a Model Amphiphilic Peptide. *Langmuir* 2015**,** *31* (27), 7590-7600.
285. Grolimund, D.; Elimelech, M.; Borkovec, M., Aggregation and deposition kinetics of mobile colloidal particles in natural porous media. *Colloid Surf. A* 2001**,** *191* (2), 179-188.
286. Joye, D. D., Shear rate and viscosity corrections for a Casson fluid in cylindrical (Couette) geometries. *J. Colloid Interface Sci.* 2003**,** *267* (1), 204-210.
287. Jenkins, H. D. B.; Marcus, Y., Viscosity B-coefficients of ions in solution. *Chem. Rev.* 1995**,** *95* (8), 2695-2724.
288. Bradford, M. M., Rapid and sensitive method for quantitation of microgram quantities of protein utilizing principle of protein-dye binding. *Anal. Biochem.* 1976**,** *72* (1-2), 248-254.
289. Beaucham, C.; Fridovich, I., Superoxide dismutase - improved assays and an assay applicable to acrylamide gels. *Anal. Biochem.* 1971**,** *44* (1), 276-287.
290. Khristenko, I. V.; Panteleimonov, A. V.; Iliashenko, R. Y.; Doroshenko, A. O.; Ivanov, V. V.; Tkachenko, O. S.; Benvenutti, E. V.; Kholin, Y. V., Heterogeneous polarity and surface acidity of silica-organic materials with fixed 1-n-propyl-3-methylimidazolium chloride as probed by solvatochromic and fluorescent dyes. *Colloid Surf. A-Physicochem. Eng. Asp.* 2018**,** *538*, 280-286.
291. Pfeiffer-Laplaud, M.; Costa, D.; Tielens, F.; Gaigeot, M. P.; Sulpizi, M., Bimodal acidity at the amorphous silica/water interface. *J. Phys. Chem. C* 2015**,** *119* (49), 27354-27362.
292. Katana, B.; Takács, D.; Csapo, E.; Szabo, T.; Jamnik, A.; Szilagyi, I., Ion specific effects on the stability of halloysite nanotube colloids-inorganic salts versus ionic liquids. *J. Phys. Chem. B* 2020**,** *124* (43), 9757-9765.
293. Oncsik, T.; Trefalt, G.; Borkovec, M.; Szilagyi, I., Specific ion effects on particle aggregation induced by monovalent salts within the Hofmeister series. *Langmuir* 2015**,** *31* (13), 3799-3807.
294. Tian, R.; Yang, G.; Li, H.; Gao, X. D.; Liu, X. M.; Zhu, H. L.; Tang, Y., Activation energies of colloidal particle aggregation: Towards a quantitative characterization of specific ion effects. *Phys. Chem. Chem. Phys.* 2014**,** *16* (19), 8828-8836.
295. Galli, M.; Saringer, S.; Szilagyi, I.; Trefalt, G., A simple method to determine critical coagulation concentration from electrophoretic mobility. *Colloid Interfac.* 2020**,** *4* (2), 20.
296. Katana, B.; Takács, D.; Szerlauth, A.; Sáringer, S.; Varga, G.; Jamnik, A.; Bobbink, F. D.; Dyson, P. J.; Szilagyi, I., Aggregation of halloysite nanotubes in the presence of multivalent ions and ionic liquids. *Langmuir* 2021**,** *37* (40), 11869-11879.
297. Borkovec, M.; Behrens, S. H.; Semmler, M., Observation of the mobility maximum predicted by the standard electrokinetic model for highly charged amidine latex particles. *Langmuir* 2000**,** *16* (11), 5209-5212.
298. Oncsik, T.; Trefalt, G.; Csendes, Z.; Szilagyi, I.; Borkovec, M., Aggregation of negatively charged colloidal particles in the presence of multivalent cations. *Langmuir* 2014**,** *30* (3), 733-741.
299. Szilagyi, I.; Polomska, A.; Citherlet, D.; Sadeghpour, A.; Borkovec, M., Charging and aggregation of negatively charged colloidal latex particles in the presence of multivalent oligoamine cations. *J. Colloid Interface Sci.* 2013**,** *392*, 34-41.
300. Sajjadi, H.; Modaressi, A.; Magri, P.; Domanska, U.; Sindt, M.; Mieloszynski, J. L.; Mutelet, F.; Rogalski, M., Aggregation of nanoparticles in aqueous solutions of ionic liquids. *J. Mol. Liq.* 2013**,** *186*, 1-6.
301. Rouster, P.; Pavlovic, M.; Cao, T.; Katana, B.; Szilagyi, I., Stability of titania nanomaterials dispersed in aqueous solutions of ionic liquids of different alkyl chain lengths. *J.*

Phys. Chem. C 2019**,** *123* (20), 12966-12974.
302. Fuerstenau, D. W.; Colic, M., Self-association and reverse hemimicelle formation at solid-water interfaces in dilute surfactant solutions. *Colloid Surf. A* 1999**,** *146* (1-3), 33-47.
303. Bastos-Gonzalez, D.; Perez-Fuentes, L.; Drummond, C.; Faraudo, J., Ions at interfaces: the central role of hydration and hydrophobicity. *Curr. Opin. Colloid Interface Sci.* 2016**,** *23*, 19-28.
304. Byun, Y.; Chang, L. C.; Lee, L. M.; Han, I. S.; Singh, V. K.; Yang, V. C., Low molecular weight protamine: A potent but nontoxic antagonist to heparin/low molecular weight protamine. *Asaio J.* 2000**,** *46* (4), 435-439.
305. Katana, B.; Rouster, P.; Varga, G.; Muráth, S.; Glinel, K.; Jonas, A. M.; Szilagyi, I., Self-assembly of protamine biomacromolecule on halloysite nanotubes for immobilization of superoxide dismutase enzyme. *ACS Appl. Bio Mater.* 2020**,** *3* (1), 522-530.
306. Bueno, J.; Long, D.; Kauffman, J. F.; Arzhantsev, S., Deep-ultraviolet resonance Raman (DUVRR) spectroscopy of therapeutic monoclonal antibodies subjected to thermal stress. *Anal. Chem.* 2015**,** *87* (15), 7880-7886.
307. Moumene, T.; Belarbi, E. H.; Haddad, B.; Villemin, D.; Abbas, O.; Khelifa, B.; Bresson, S., Study of imidazolium dicationic ionic liquids by Raman and FTIR spectroscopies: The effect of the nature of the anion. *J. Mol. Struct.* 2015**,** *1083*, 179-186.
308. Caspers, P. J.; Lucassen, G. W.; Wolthuis, R.; Bruining, H. A.; Puppels, G. J., In vitro and in vivo Raman spectroscopy of human skin. *Biospectroscopy* 1998**,** *4* (5), S31-S39.
309. Kloprogge, J. T.; Frost, R. L., Raman microprobe spectroscopy of hydrated halloysite from a neogene cryptokarst from southern Belgium. *J. Raman Spectrosc.* 1999**,** *30* (12), 1079-1085.
310. Maksym, P.; Tarnacka, M.; Dzienia, A.; Erfurt, K.; Chrobok, A.; Zieba, A.; Wolnica, K.; Kaminski, K.; Paluch, M., A facile route to well-defined imidazolium-based poly(ionic liquid)s of enhanced conductivity via RAFT. *Polym. Chem.* 2017**,** *8* (35), 5433-5443.
311. Gonchar, K. A.; Kondakova, A. V.; Jana, S.; Timoshenko, V. Y.; Vasiliev, A. N., Investigation of halloysite nanotubes with deposited silver nanoparticles by methods of optical spectroscopy. *Phys. Solid State* 2016**,** *58* (3), 601-605.
312. Cao, T. C.; Sugimoto, T.; Szilagyi, I.; Trefalt, G.; Borkovec, M., Heteroaggregation of oppositely charged particles in the presence of multivalent ions. *Phys. Chem. Chem. Phys.* 2017**,** *19* (23), 15160-15171.
313. Katana, B.; Takács, D.; Bobbink, F. D.; Dyson, P. J.; Alsharif, N. B.; Tomšič, M.; Szilagyi, I., Masking specific effects of ionic liquid constituents at the solid–liquid interface by surface functionalization. *Phys. Chem. Chem. Phys.* 2020**,** *22* (42), 24764-24770.
314. Bannister, J.; Bannister, W.; Wood, E., Bovine erythrocyte cupro-zinc protein 1. Isolation and general characterization. *Eur. J. Biochem.* 1971**,** *18* (2), 178-186.
315. Farmer, V. C.; Russel, J. D., The infra-red spectra of layer silicates. *Spectroc. Acta* 1964**,** *20* (7), 1149-1173.
316. Mei, D. D.; Zhang, B.; Liu, R. C.; Zhang, Y. T.; Liu, J. D., Preparation of capric acid/halloysite nanotube composite as form-stable phase change material for thermal energy storage. *Sol. Energy Mater. Sol. Cells* 2011**,** *95* (10), 2772-2777.
317. Wang, Y. Y.; Qiu, W. Y.; Wang, Z. B.; Ma, H. L.; Yan, J. K., Extraction and characterization of anti-oxidative polysaccharide-protein complexes from Corbicula fluminea through three-phase partitioning. *RSC Adv.* 2017**,** *7* (18), 11067-11075.
318. Fakhrullina, G.; Khakimova, E.; Akhatova, F.; Lazzara, G.; Parisi, F.; Fakhrullin, R., Selective antimicrobial effects of curcumin@halloysite nanoformulation: A caenorhabditis elegans study. *ACS Appl. Mater. Interfaces* 2019**,** *11* (26), 23050-23064.
319. Zhang, Y. M.; Li, Y. Q.; Zhang, Y. F.; Ding, D. Q.; Wang, L.; Liu, M.; Zhang, F. C., Thermal behavior and kinetic analysis of halloysite-stearic acid complex. *J. Therm. Anal.*

Calorim. 2019**,** *135* (4), 2429-2436.
320. Sheldon, R. A.; van Pelt, S., Enzyme immobilisation in biocatalysis: why, what and how. *Chem. Soc. Rev.* 2013**,** *42* (15), 6223-6235.
321. Bertoli, A. C.; Carvalho, R.; Freitas, M. P.; Ramalho, T. C.; Mancini, D. T.; Oliveira, M. C.; de Varennes, A.; Dias, A., Structural determination of Cu and Fe-Citrate complexes: theoretical investigation and analysis by ESI-MS. *J. Inorg. Biochem.* 2015**,** *144*, 31-37.
322. Ghosh, R.; Asha, K. S.; Pratik, S. M.; Datta, A.; Nath, R.; Mandal, S., Synthesis, structure, photocatalytic and magnetic properties of an oxo-bridged copper dimer. *RSC Adv.* 2014**,** *4* (41), 21195-21200.
323. Katana, B.; Nagy, N. V.; Varga, G.; Szilagyi, I., Superoxide dismutase mimicking nanocomposites based on immobilization of metal complexes on nanotubular carriers. *J. Mol. Struct.* 2022**,** *1256*, 132492.
324. Lu, P. J.; Hu, W. W.; Chen, T. S.; Chern, J. M., Adsorption of copper-citrate complexes on chitosan: Equilibrium modeling. *Bioresour. Technol.* 2010**,** *101* (4), 1127-1134.
325. Muráth, S.; Sáringer, S.; Somosi, Z.; Szilagyi, I., Effect of ionic compounds of different valences on the stability of titanium oxide colloids. *Colloid Interfac.* 2018**,** *2* (3), 32.
326. Saringer, S.; Rouster, P.; Szilagyi, I., Regulation of the stability of titania nanosheet dispersions with oppositely and like-charged polyelectrolytes. *Langmuir* 2019**,** *35* (14), 4986-4994.
327. Pattanayak, S.; Swarnkar, A.; Priyam, A.; Bhalerao, G. M., Citrate-hydrazine hydrogen-bonding driven single-step synthesis of tunable near-IR plasmonic, anisotropic silver nanocrystals: implications for SERS spectroscopy of inorganic oxoanions. *Dalton Trans.* 2014**,** *43* (31), 11826-11833.
328. Siiman, O.; Ledis, S., Surface-enhanced Raman scattering (SERS) of random silver or gold particle arrays on aminodextran-coated polystyrene beads. *J. Raman Spectrosc.* 2005**,** *36* (12), 1125-1133.
329. Fang, Y. C.; Lin, H. C.; Hsu, I. J.; Lin, T. S.; Mou, C. Y., Bioinspired design of a Cu-Zn-imidazolate mesoporous silica catalyst system for superoxide dismutation. *J. Phys. Chem. C* 2011**,** *115* (42), 20639-20652.

10. Supplementary Information

Table S1. Fitting parameters applied to interpolate the refractive index and viscosity values of the IL solutions.

IL	Refractive Index[a]		Viscosity[b]		
	a (M^{-1})	b	A ($M^{-1/2}$)	B (M^{-1})	D (M^{-2})
BMIMCl	3.10×10^{-2}	1.3310	0.3774	2.87×10^{-4}	0.3894
BMPYCl	3.94×10^{-2}	1.3308	0.7738	3.47×10^{-2}	0.6350
BMPIPCl	3.74×10^{-2}	1.3294	0.1724	-7.70×10^{-1}	1.4782
BMPYRCl	3.12×10^{-2}	1.3311	0.7915	-5.95×10^{-1}	0.7591

[a]Fitting parameters of equation (31). [b]Fitting parameters of equation (32).

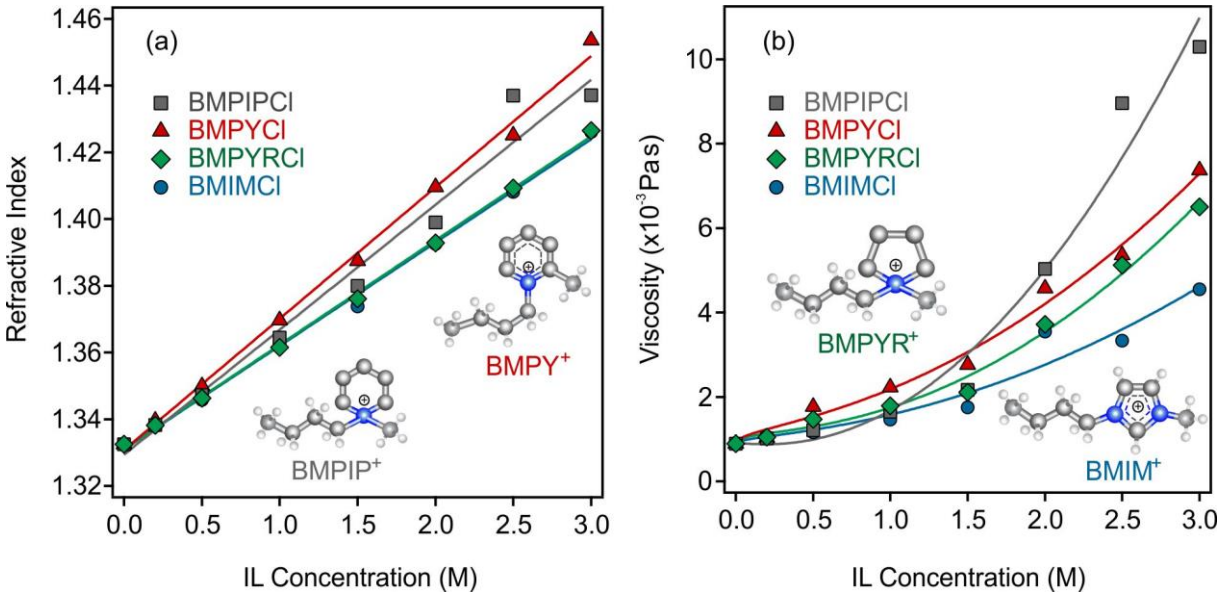

Figure S1. Refractive index (a) and viscosity (b) data of aqueous IL (BMIMCl, BMPYCl, BMPYRCl, and BMPIPCl) solutions at various concentrations. The solid lines represent fits obtained using equation (31) (a) and equation (32) (b) used for the interpolation of the data. Reprinted (adapted) with permission from Ref. 292. Copyright (2022) American Chemical Society.

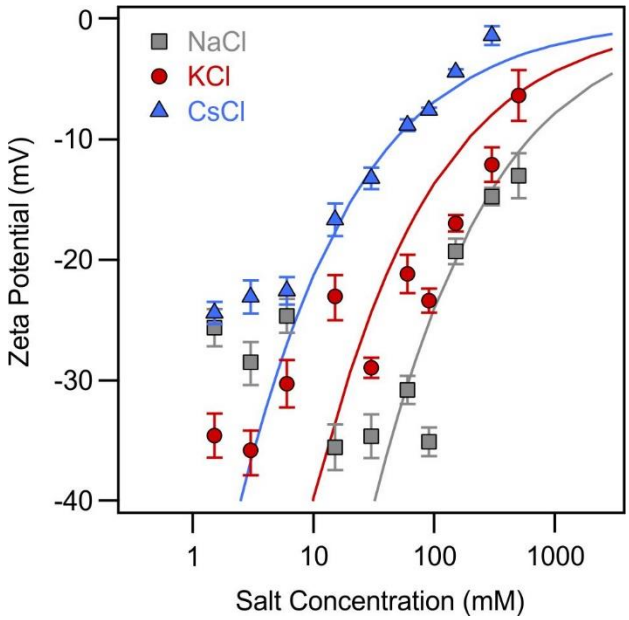

Figure S2. Zeta potential values of h-HNTs at various concentrations of monovalent salts. The lines represent the results of calculations utilizing equation (17). Reprinted (adapted) with permission from Ref. 292. Copyright (2022) American Chemical Society.

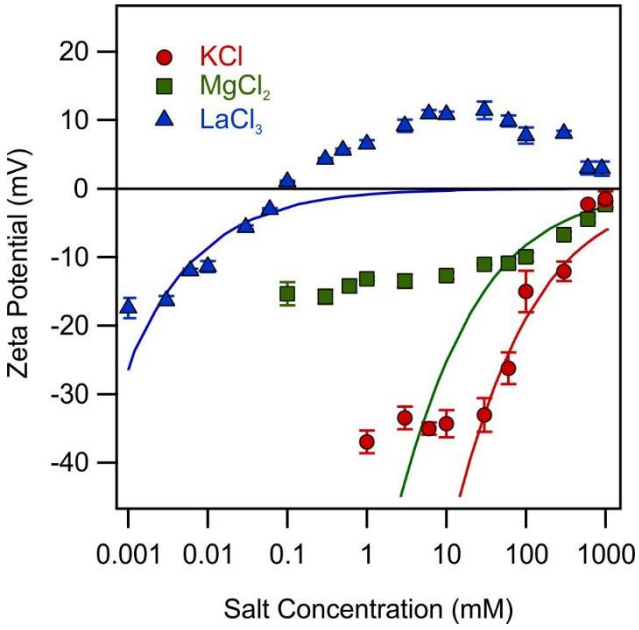

Figure S3. Zeta potential values of h-HNTs at different concentrations of multivalent salts. The lines represent the results of calculations using equation (17). Reprinted (adapted) with permission from Ref. 296. Copyright (2022) American Chemical Society.

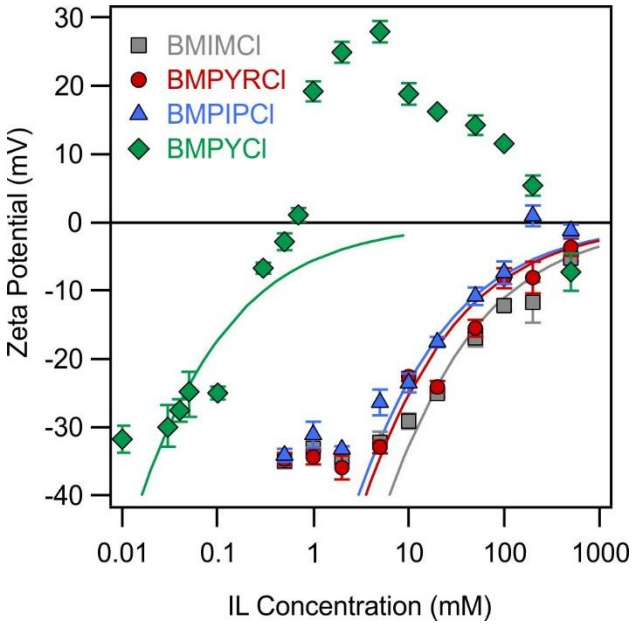

Figure S4. Zeta potential values of h-HNTs at different concentrations of IL solutions with different cation structures. The lines are the results of calculations using equation (17). Reprinted (adapted) with permission from Ref. 292. Copyright (2022) American Chemical Society.

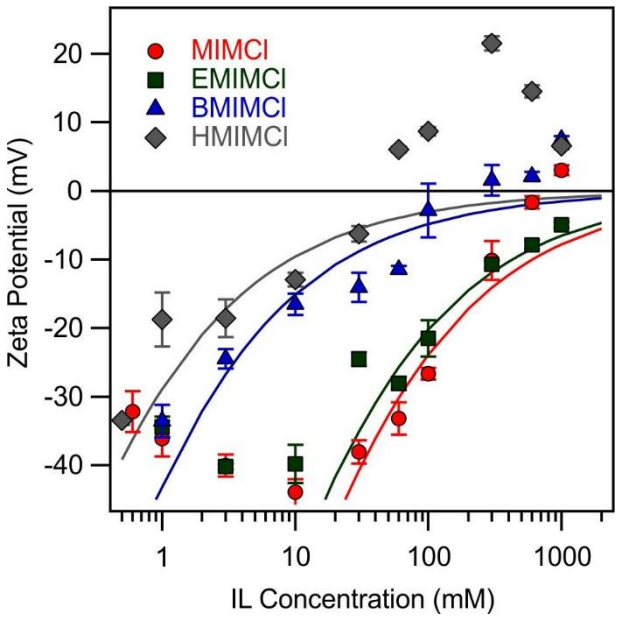

Figure S5. Zeta potential values of h-HNTs at different concentrations of imidazolium-based ILs with different alkyl chain lengths. The lines represent the results of calculations using equation (17). Reprinted (adapted) with permission from Ref. 296. Copyright (2022) American Chemical Society.

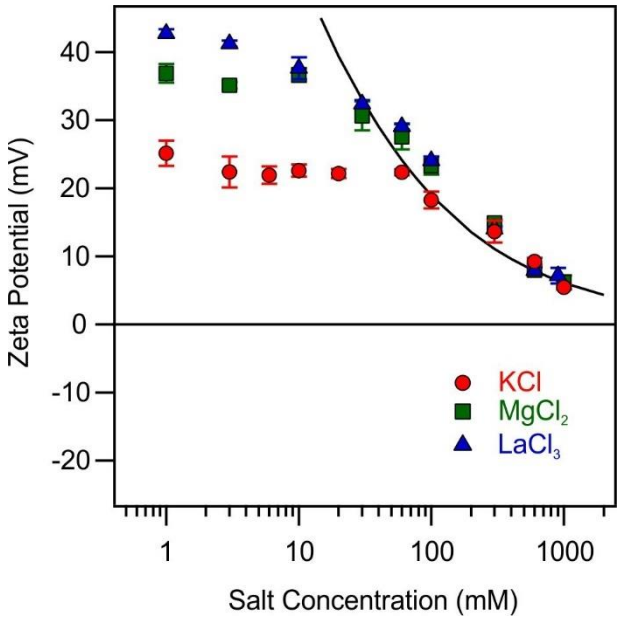

Figure S6. Zeta potential values of h-HNT-IP-2 at different concentrations of multivalent salts. The line is result of calculation using equation (17). Reprinted (adapted) with permission from Ref. 296. Copyright (2022) American Chemical Society.

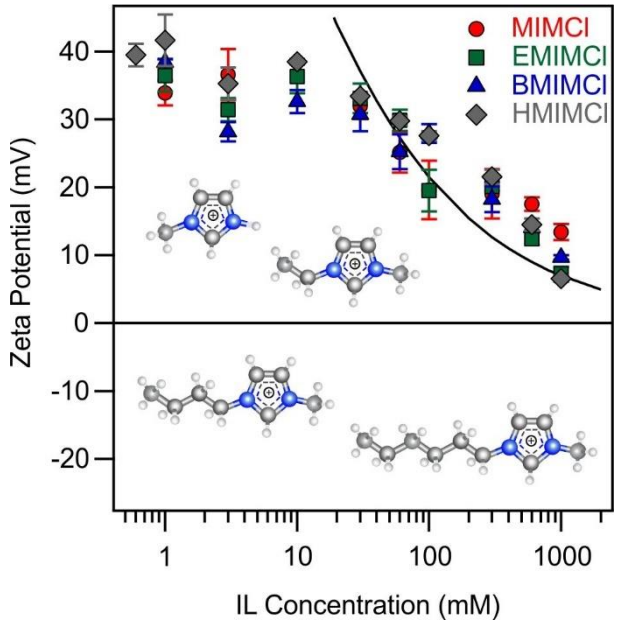

Figure S7. Zeta potential values of h-HNT-IP-2 at different concentrations of imidazolium-based ILs with different alkyl chain lengths. The line is result of calculation using equation (17). Reprinted (adapted) with permission from Ref. 296. Copyright (2022) American Chemical Society.

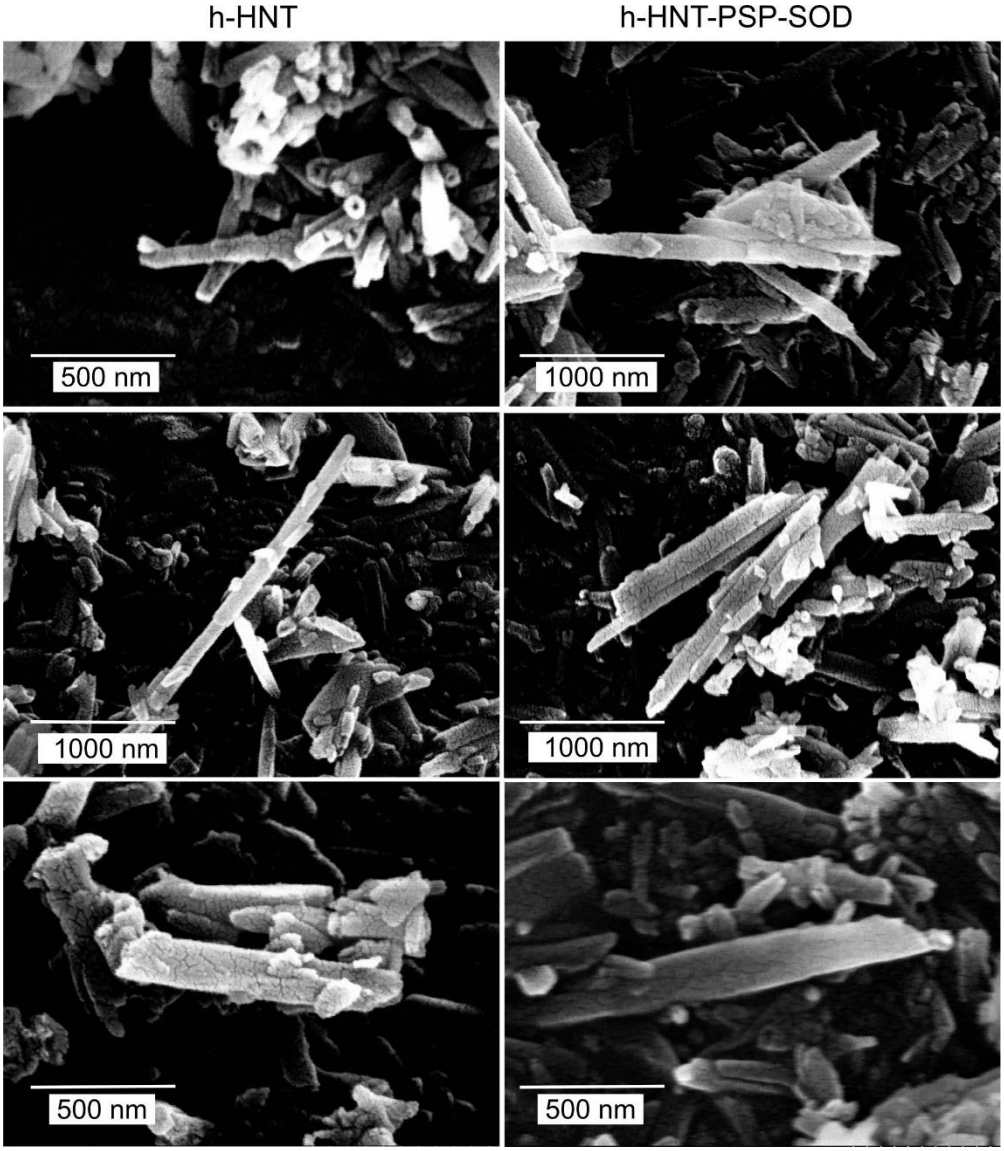

Figure S8. SEM images of bare h-HNT (left column) and h-HNT-PSP-SOD (right column) materials. The h-HNT-PSP-SOD nanotubes contained 100 mg of PSP and 10 mg of SOD together with 1 g of h-HNT. Reprinted (adapted) with permission from Ref. 305. Copyright (2022) American Chemical Society.

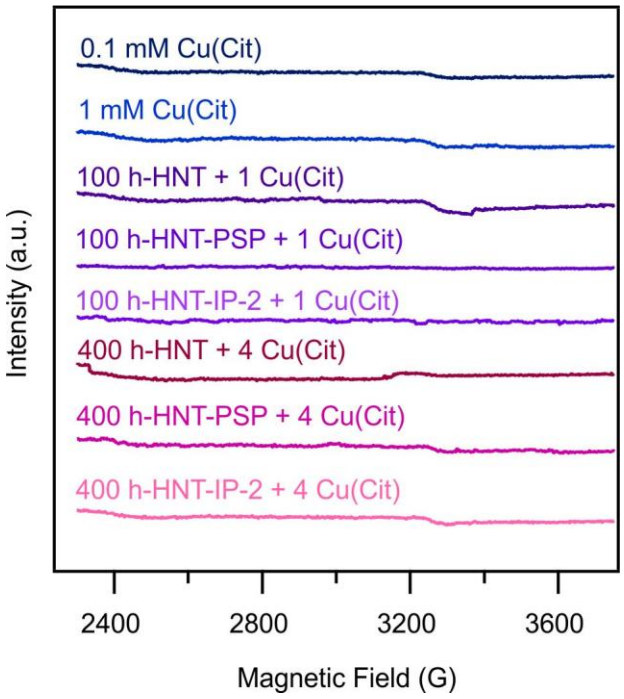

Figure S9. EPR spectra recorded for the Cu(Cit) complexes in solutions and in the presence of h-HNT, h-HNT-PSP, and h-HNT-IP-2 at different concentrations. The numbers 100 and 400 represent the final particle concentrations expressed in mg/L, while 1 and 4 are the Cu(Cit) concentrations in mM unit. Reprinted from Ref. 323. Copyright (2022), with permission from Elsevier.